University of Cape Town

Chaotic behaviour of disordered nonlinear lattices

Bob Senyange

A thesis presented for the degree of
Doctor of Philosophy

Department of Mathematics and Applied Mathematics

April 2021

Supervisor: Associate Professor Haris Skokos

Abstract

In this work we systematically investigate the chaotic energy spreading in prototypical models of disordered nonlinear lattices, the so-called disordered Klein-Gordon (DKG) system, in one (1D) and two (2D) spatial dimensions. The normal modes' exponential localization in 1D and 2D heterogeneous linear media explains the phenomenon of Anderson Localization. Using a modified version of the 1D DKG model, we study the changes in the properties of the system's normal modes as we move from an ordered version to the disordered one. We show that for the ordered case, the probability density distribution of the normal modes' frequencies has a 'U'-shaped profile that gradually turns into a plateau for a more disordered system, and determine the dependence of two estimators of the modes' spatial extent (the localization volume and the participation number) on the width of the interval from which the strengths of the on-site potentials are randomly selected. Furthermore, we investigate the numerical performance of several integrators (mainly based on the two part splitting approach) for the 1D and 2D DKG systems, by performing extensive numerical simulations of wave packet evolutions in the various dynamical regimes exhibited by these models. In particular, we compare the computational efficiency of the integrators considered by checking their ability to correctly reproduce the time evolution of the systems' finite time maximum Lyapunov exponent estimator Λ and of various features of the propagating wave packets, and determine the best-performing ones. Finally we perform a numerical investigation of the characteristics of chaos evolution for a spreading wave packet in the 1D and 2D nonlinear DKG lattices. We confirm the slowing down of the chaotic dynamics for the so-called weak, strong and selftrapping chaos dynamical regimes encountered in these systems, without showing any signs of a crossover to regular behaviour. We further substantiate the dynamical dissimilarities between the weak and strong chaos regimes by establishing different, but rather general, values for the time decay exponents of Λ. In addition, the spatio-temporal evolution of the deviation vector associated with Λ reveals the meandering of chaotic seeds inside the wave packets, supporting the assumptions for chaotic spreading theories of energy.

Declaration

I know the meaning of plagiarism and declare that all the work on the *Chaotic behaviour of disordered nonlinear lattices* contained in this thesis except that which is properly acknowledged as references is my own work and that it has not been submitted before for any degree or examination in any University.

Bob Senyange

Acknowledgements

I would like to firstly express my deepest gratitude to my thesis advisor Assoc. Prof. Haris Skokos for having granted me the chance to work with him, his collaborators and team of students. Most notably his guidance and mentorship, facilitation, availability for discussion at all times and patience whenever things did not go as planned.

I am also grateful to all colleagues and visitors of the research group, led by Assoc. Prof. Skokos, most especially: A. Schwellnus, B. K. Mfumadi, A. Ngapasare, M. Hillebrand, B. M. Many, A. J. Chinenye, H. Moges and J-J. Du Plessis for their academic and social contribution during the course of my studies and in particular for the insightful scientific discussions. Fellow colleagues and friends, Dr. H. J. B. Njagarah, Dr. B. Aineamani, J. Nagawa, M. Isiagi and L. Mthombeni, are much appreciated for welcoming me to Cape Town and ensuring my well-being at all times.

I additionally express my thanks to the members of the Center for High Performance Computing (CHPC, South Africa), whose facility I used for my computations, especially Mr. Kevin Colville who attended to me from the time I started learning scientific computing. I express my gratitude to the University of Cape Town's (UCT) ICTS High Performance Computing team whose services offered HPC training courses and a working space on the University facilities for my computations. I am also grateful to the staff of the Department of Mathematics and Applied Mathematics (MAM) for providing a pleasant working environment. Great thanks to Mr. Nimrod Matotong of MAM for ensuring my working space and data stored on 'Zeus' MAM computing facility are as required and for attending to my immediate computer needs especially software installations and repairs.

I am so grateful to my family, especially my mother for her encouraging words, my dear wife Lilian for her love, patience, and great support during the time I was away for studies and the period of writing this thesis, my daughters Josephine Gemma and Mariah Antonia, my son Leroy and all my siblings for the prayers and having to bear with my absence. 'Eri bazadde bange, Taata (Omukama akuwummuze mirembe) ne Maama Nyonjo, mweebale kunteekerateekera kkubo lino eryatandikira ddala okuva mu buto bwange'. I am grateful to God for He heard our prayers and made a way for me even when it seemed impossible.

Last but not the least, I also thank Muni University (Arua, Uganda) for awarding me the African Development Bank (ADB V-HEST) scholarship (2016-2019) towards my studies, the UCT for awarding me the International & Refugee students' scholarship 2018 and the various institutions or persons that facilitated my travels to the conferences I attended.

Publications and Talks related to this work

Parts of the work in this thesis have been presented in the international peer reviewed journal papers listed below.

P-1 **B. Senyange** and Ch. Skokos, *Computational efficiency of symplectic integration schemes: Application to multidimensional disordered Klein–Gordon lattices*, Eur. Phys. J. Spec. Top. **227**, 625 (2018).

P-2 **B. Senyange**, B. Many Manda, and Ch. Skokos, *Characteristics of chaos evolution in one-dimensional disordered nonlinear lattices*, Phy. Rev. E. **98**, 052229 (2018).

P-3 B. Many Manda, **B. Senyange**, and Ch. Skokos, *Chaotic wave-packet spreading in two-dimensional disordered nonlinear lattices*, Phy. Rev. E. **101**, 032206 (2020).

P-4 **B. Senyange**, J.-J. du Plessis, B. Many Manda, and Ch. Skokos, *Properties of normal modes in a modified disordered Klein–Gordon lattice: From disorder to order*, Nonlinear Phenomena in Complex Systems, **23**, 165−171 (2020).

Some results from this work have also been included in the following oral and poster conference presentations delivered by B. Senyange.

C-1 "On the symplectic integration of the Klein-Gordon lattice model", *The* 3^{rd} *EAUMP conference*, Makerere University, Kampala (Uganda), October 26−28, 2016 (Oral presentation).

C-2 "Chaotic dynamics of the disordered Klein-Gordon lattice", *The International Scientific Workshop: Recent Advances in Hamiltonian and Nonholonomic Dynamics*, Moscow (Russia), June 15−18, 2017 (Oral presentation).

C-3 "Chaotic dynamics of one-dimensional disordered nonlinear lattices", *Nonlinear Localization in Lattices*, Spetses (Greece), June 18−22, 2018 (Poster presentation).

C-4 "On characterising the dynamics of 1-D disordered nonlinear Hamiltonian lattices", *The annual Southern Africa Mathematical Sciences Association (SAMSA) conference*, Palapye (Botswana), November 19−22, 2018 (Oral presentation).

C-5 "Chaotic dynamics in disordered nonlinear lattices", *The International Congress on Industrial and Applied Mathematics (ICIAM)*, Valencia (Spain), July 15−19, 2019 (Oral presentation).

C-6 "Chaotic dynamics in disordered nonlinear lattices: Symplectic integrators", *The International Congress on industrial and Applied Mathematics (ICIAM)*, Valencia (Spain), July 15−19, 2019 (Poster presentation).

C-7 "Chaotic dynamics in disordered nonlinear lattices: Symplectic integrators", *The 62nd Annual Congress of South African Mathematical Society (SAMS)*, Cape Town (South Africa), December 2−4, 2019 (Oral presentation).

C-8 "Symplectic integration techniques for disorderd nonlinear Hamiltonian lattices", *The annual Southern Africa Mathematical Sciences Association (SAMSA) conference*, Virtual, November 23−25, 2020 (Oral presentation).

List of abbreviations

1D - one-dimensional
2D - two-dimensional
AL - Anderson Localization
BCH - Baker Campbell Hausdorff
BEC - Bose–Einstein condensate
DDLSE - Disordered discrete linear Schrödinger equation
DDNLS - Disordered discrete nonlinear Schrödinger
DFPUT - Disordered Fermi Pasta Ulam Tsingou
DKG - Disordered Klein-Gordon
DNA - Deoxyribo-Nucleic Acid
DVD - Deviation vector distribution
FPUT - Fermi Pasta Ulam Tsingou
IC - Initial condition
KG - Klein-Gordon
LCE - Lyapunov characteristic exponent
mLCE - maximum Lyapunov characteristic exponent
NM - Normal mode
PBD - Peyrard–Bishop Dauxois
SI - Symplectic integrator
TDH - Tangent dynamics Hamiltonian
TM - Tangent map

Contents

Chapter 1

Introduction

Disordered models are extended systems in space with many degrees of freedom which try to mimic heterogeneous arrangements observed in natural phenomena. Heterogeneity is introduced in the model by attributing a unique random value (or a set of unique random values) for each degree of freedom in relation to one (or many) of the system's parameter(s). Anderson Localization (AL), a phenomenon where energy excitations remain localized in linear systems with sufficient disorder, was discovered about six decades ago by physicist Phillip Warren Anderson [Anderson, P. (1958)] in a work investigating the underlying mechanisms of electron transport in crystals, which won him the Nobel Prize in 1977. Anderson considered the tight-binding approximation for an electron on a lattice with randomly distributed on-site energies and nearest-neighbour tunnelling. Electron inability to diffuse away from an initial position was related to the wave function amplitude falling off exponentially with growing distance from its original location. This wave localization behaviour is a phenomenon of phase-coherence. Therefore, the electronic state keeps phase coherence, while loss of coherence leads to delocalization [Rayanov et al. (2013)]. AL manifests in many types of wave propagation in disordered systems, for example in the dynamics of Bose–Einstein condensates, the conductivity process of materials, etc. AL has been extensively investigated in theoretical and numerical [Kopidakis et al. (2008); Pikovsky and Shepelyansky (2008); Flach et al. (2009b); Laptyeva et al. (2014); Prat et al. (2019)], and experimental [Hu et al. (2008); Lahini et al. (2008); Cobus et al. (2016)] studies in the context of metal-insulator transitions, dynamics of ultracold atoms in optical arrays, light propagation in photonic crystals and the quantum Hall effect [Kramer et al. (1993); Evers and Mirlin (2008); Sanchez-Palencia and Lewenstein (2010)]. Heterogeneity in disordered systems can be either correlated or uncorrelated but still leads to localization. In his study, Anderson [Anderson, P. (1958)] used uncorrelated disorder. In general, the normal modes (NMs) of linear systems with sufficiently strong disorder are localized and therefore any initially localized wave packet does not exhibit a spreading behaviour for all time. The introduction of nonlinearities to such systems leads to NM interaction and hence the emergence of chaos.

The nonlinearity effect in disordered systems has attracted extensive attention in experiments [Dalichaouch et al. (1991); Schwartz et al. (2007); Billy et al. (2008); Lahini et al. (2008); Roati et al. (2008)], as well as in theory and simulations [Kopidakis et al. (2008); Pikovsky and Shepelyansky (2008); Flach et al. (2009b); Skokos et al. (2009); García-Mata and Shepelyansky (2009); Veksler et al. (2009); Laptyeva et al. (2010); Basko (2011); Mulansky and Pikovsky (2012, 2013)] and it has been primarily investigated using the one-dimensional (1D) disordered discrete nonlinear Schrödinger equation (DDNLS) and the disordered nonlinear Klein-Gordon (DKG) lattice models [Pikovsky and Shepelyansky (2008); Flach et al. (2009b); Skokos et al. (2009); Flach

(2010); Laptyeva et al. (2010); Skokos and Flach (2010); Bodyfelt et al. (2011b); Skokos et al. (2013); Laptyeva et al. (2014)]. It was revealed in these research papers that AL is eventually destroyed by nonlinearity and the characteristics of different spreading behaviours, namely the so-called 'weak', 'strong' and 'selftrapping' regimes of chaos, were identified and their appearance was theoretically explained. From the models' structural point of view, the appearance of these dynamical regimes can be explained using the systems' NMs properties, that is to say, the NMs' localization volume, the width of their frequency band, the average eigenvalue spacing of the modes which strongly interact with a particular NM, and the magnitude of these quantities compared to the nonlinearity induced frequency shift [Flach et al. (2009b); Laptyeva et al. (2010); Flach (2010); Laptyeva et al. (2014)].

The studies performed on the 1D DKG model reported in Skokos et al. (2013) confirmed that nonequilibrium chaos and phase decoherence persist in a disordered nonlinear system thus fuelling the prediction of a complete delocalization. However, the following are a number of interesting related open questions that have been raised in the past few years: What is the connection between chaoticity and energy transport? How does the initial excitation affect the chaoticity and the nature of it's evolution in time? How does the appearance of chaos depend on the basic dynamical parameters of the system, i.e. the disorder and nonlinearity strengths? Are wave packets homogeneously chaotic, or there exist 'chaotic hot spots', with some degrees of freedom behaving 'more' chaotically than others? Will wave packets eventually exhibit a less chaotic behaviour, leading to the halt of spreading [Johansson et al. (2010); Aubry (2011)], or will they spread indefinitely as recent numerical simulations have indicated [Kopidakis et al. (2008); Pikovsky and Shepelyansky (2008); Flach et al. (2009b); Skokos et al. (2009); García-Mata and Shepelyansky (2009); Laptyeva et al. (2010); Skokos and Flach (2010); Bodyfelt et al. (2011b); Skokos et al. (2013)]? What are the basic principles and the intrinsic dynamical components that define the observed chaotic behaviours? How the observed dynamical behaviours depend on the dimensionality of our lattice and more explicitly how all these behaviours alter when we consider 2D disordered systems?

The scope of this thesis is to set the basis for a systematic study of these questions providing some concrete answers to them. For this purpose we use the maximum Lyapunov characteristic exponent (mLCE) to characterize chaos along with the deviation vector distributions (DVDs) [Skokos et al. (2013)], which is used to identify possible 'chaotic hot spots'. Extensive numerical simulations of wave packets evolution for different initial excitations and for several values of disorder and nonlinearity strengths are performed and their dynamics is analysed by the above mentioned techniques in an attempt to uncover the mechanisms that introduce chaos in disordered systems. We note that although we will mainly present results for a 1D disordered lattice namely the 1D DKG system, a significant part of our analysis will be devoted to the less studied case of 2D lattices in order to get a broader understanding of the generality of our results for the chaotic dynamics of disordered lattices in spatial dimensions greater than one.

The thesis is organised in six chapters as follows. In Chapter 2 we present a review of some theoretical, experimental and numerical aspects of energy localization in linear disordered systems. We also discuss some theoretical results about the properties of energy spreading in typical 1D lattices followed by the structural properties of their NMs through a wide range of disorder strengths. In Chapter 3, we present in detail the numerical techniques used to obtain our findings. In Chapter 4 we discuss results for the 1D DKG system while we extend our investigation to the computationally more challenging case of the 2D DKG model in Chapter 5. Finally in Chapter 6 we summarize the results of our work.

Chapter 2

Disordered lattices

Disordered systems exist in nature, for example in cases where imperfections or impurities appear in materials, and disordered models try to capture their dynamics. We can therefore consider disordered systems to be models with many degrees of freedom, extended in space, exhibiting heterogeneity as observed in nature. For such a system, heterogeneity is modelled by allocating random values to one or more of the system's parameters in each degree of freedom. In 1958, a phenomenon where in linear disordered systems, whose eigenstates are also localized, energy excitations do not propagate but remain localized was studied by Anderson [Anderson, P. (1958)]. This behaviour, a study which won him a Nobel Prize in 1977, is usually called AL. AL can be used to explain the evolution of many physical processes for example, the conductivity of materials and the dynamics of Bose–Einstein condensates (BECs).

In this chapter we present some examples of widely studied ordered models and also discuss briefly the theory of disordered lattices. The chapter is presented in the following order: We briefly present some widely studied ordered models in Section 2.1 and discuss their dynamical properties and characteristics in relation to disordered systems. Section 2.2 discusses the underlying dynamical properties of linear models using as an example the well known Anderson model [Anderson, P. (1958)] for two different forms of disorder. We then discuss the dynamics of nonlinear models in Section 2.3 and give some examples emphasizing already published results for them. In particular, we focus on the two main models used in our research namely, the DKG chain of anharmonic oscillators and the DDNLS system. For small wave packet amplitudes, there exists a direct correspondence between the parameters of the DDNLS system and those of the DKG model. Because of this, we only theoretically discuss in detail the properties of disordered models using the DDNLS model. Section 2.4 describes some of the measures we use in quantifying the spatial extent of wave packets, and lastly, we present results on the properties of NMs for a modified Klein-Gordon model having a disorder set with a variable width in Section 2.5. Parts of the results discussed in Section 2.5 were also presented in Senyange et al. (2020).

2.1 Ordered lattices

As a precursor to disordered systems, we present some examples of homogeneous Hamiltonian models which have been used to understand the phenomenon of energy propagation in physical processes.

Fermi Pasta Ulam Tsingou (FPUT) models

In 1955, a Los Alamos publication [Fermi et al. (1955)] introduced and described the now famous FPUT (originally named as FPU) problem: a paradox in chaos theory where a number of physical systems exhibited almost exactly periodic behaviour. This discovery was a great contribution to the birth of nonlinear science, whose explorations led to the revelation of interesting phenomena like for example the existence of solitons (a wave packet propagating at a constant velocity while maintaining its shape) [Sirovich et al. (2005)] and to the deeper understanding of chaotic dynamics. The main communication in Fermi et al. (1955) was the observation of a practical recurrence of the initial state as opposed to the expected state of energy equipartition amongst the modes of the FPUT 1D system. Over the years, studies of the FPUT problem have led to deeper understanding of the dynamical behaviour of ordered discrete nonlinear lattices with many degrees of freedom. The FPUT model has been pivotal in the theoretical studies of solitons, inverse scattering, discrete breathers, fully integrable systems, equipartition of energy and the development of Chirikov's criterion for the onset of chaotic motion [Ford (1992); Campbell et al. (2012)] in lattice models. Some of the most recent studies have led to the observation of the FPUT recurrence with dependence on space and time [Goossens et al. (2019)], regular motion in multidimensional models [Moges et al. (2020)] and dynamics of the model in thermal equilibrium [Amati and Schilling (2020)].

Klein Gordon models

The Klein-Gordon (KG) system without disorder has been investigated as far back as 1980. In Butera et al. (1980), it was confirmed that for the KG model of a lattice field theory, the lower frequency oscillators have smaller critical energies (describing the stochasticity border separating the regions of chaos from those of order) than the higher frequency oscillators. Two years later, the model was used to probe oscillator behaviour as the system approaches thermodynamic equilibrium [Fucito et al. (1982)]. Further works regarding thermalization in the KG chain have been carried out including Giorgilli et al. (2015), Paleari and Penati (2016), Pistone et al. (2018), and Danieli et al. (2019) among others.

2.2 Linear disordered models and Anderson localization

Linearity/Nonlinearity is a key ingredient to consider when dealing with transport properties of energy in disordered lattices. It is well known that linearity combined with a presence of sufficiently strong disorder leads to AL [Anderson, P. (1958)]. Wave delocalization, however, is due to loss of phase coherence and so for AL to occur, the state of the electrons has to preserve the coherence [Rayanov et al. (2013)]. However, in the general sense, AL occurs in many different scenarios of wave packet propagation involving a variety of disordered media. Experimental observation of AL for matter, electromagnetic and acoustic waves in disordered systems has been reported. For example in John et al. (1983), phonon localization in heterogeneous elastic media was predicted and four years later, in John (1987) the critical behaviour of electromagnetic waves in heterogeneous dielectric systems was described, while in Wiersma et al. (1997) an optical experiment showing AL of light was reported. We now briefly describe the Anderson model in one and two spatial dimensions and mention some studies where AL has been observed.

Anderson model

In 1D, the N oscillator Anderson model (a tight-binding approximation model for electron motion) is described using the Hamilton function [Anderson, P. (1958)]

$$H_{1A} = \sum_{l=1}^{N} \left[\epsilon_l |\psi_l|^2 - \left(\psi_{l+1}\psi_l^* + \psi_{l+1}^*\psi_l\right)\right], \tag{2.1}$$

with ψ_l being a complex variable denoting the l^{th} site wave function and ψ_l^* denotes the corresponding complex conjugate. The random on-site energies ϵ_l, which introduce the disorder, are chosen from the distribution

$$\mathcal{P}(\epsilon_l) = \begin{cases} \frac{1}{W}, & \text{for } |\epsilon_l| < \frac{W}{2}; \\ 0, & \text{otherwise.} \end{cases}$$

In this case, parameter $W \neq 0$ dictates the magnitude of the onsite energies.
The schematic representation of model (2.1) where the electron tunnels with a unit constant rate between immediate neighbouring sites is presented in Figure 2.1. In Figure 2.1 **(a)**, there is no disorder in the system, and the wave function (represented by the blue sinusoidal curve) is extended. The introduction of disorder in the system [Figure 2.1 **(b)**], leads to a spatial wave function (represented by the upper blue curve) localization with exponentially decaying tails.

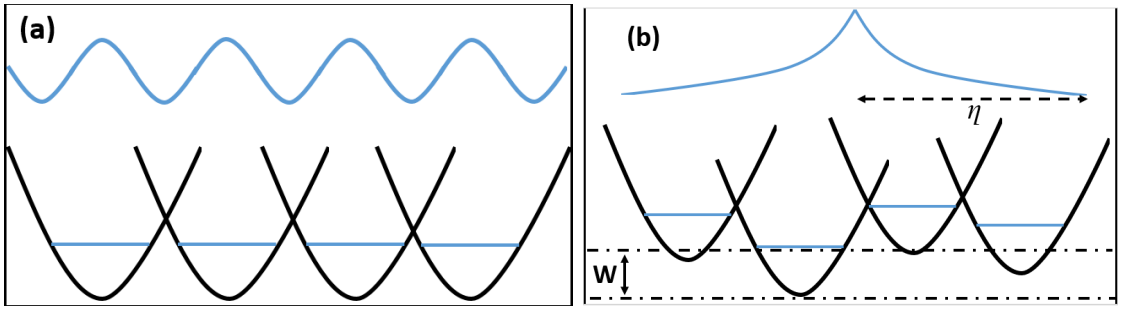

Figure 2.1: **Bottom:** Representation of the Anderson electron model (2.1) for a lattice **(a)** without disorder and **(b)** with disorder. **Top:** The electronic wave function is **(a)** extended in the homogeneous case and, **(b)** localized with exponentially decaying tails and localization length η in the disordered case.

The equations of motion of system (2.1) are generated by $\dot{\psi}_l = \frac{\partial H_{1A}}{\partial(i\psi_l^*)}$ and yield the 1D disordered Discrete Linear Schrödinger equation (DDLSE):

$$i\dot{\psi}_l = -\psi_{l+1} + \epsilon_l\psi_l - \psi_{l-1}. \tag{2.2}$$

Taking $\psi_l(t) = A_l e^{-i\lambda t}$ and substituting in equation (2.2) we get the linear eigenvalue problem

$$\lambda A_l = \epsilon_l A_l - A_{l+1} - A_{l-1}. \tag{2.3}$$

The system's NMs are the normalized eigenvectors $A_{\nu,l}$ (where $\sum_l A_{\nu,l}^2 = 1$) and the frequencies of these modes are the corresponding eigenvalues λ_ν. Finding the solution of eigenvalue problem (2.3) is equivalent to diagonalizing the tridiagonal matrix $\mathbf{A}$ with elements

$$a_{k,l} = \begin{cases} \epsilon_k, & \text{for } k = l; \\ -1, & \text{for } k = l \pm 1; \\ 0, & \text{otherwise.} \end{cases} \tag{2.4}$$

Theorem 1 (Gershgorin circle theorem) *Let* $\mathbf{A}$ *be a matrix whose entries are defined in equation* (2.4)*. Define* R_k *as* $R_k = \sum_l |a_{k,l}|$*. Then, the eigenvalues* λ_ν *of matrix* $\mathbf{A}$ *are bounded as* $|\lambda_\nu - a_{k,k}| \leq R_k - |a_{k,k}|$*.*

Using Theorem 1 [Gerschgorin (1931); Wolkowicz and Styan (1980)], we find the upper and lower bounds of the eigenvalues λ_ν to be respectively $2 + \epsilon_l$ and $-2 + \epsilon_l$. Since $\epsilon_l \in [-W/2, W/2]$, the maximum and minimum possible values of the frequencies are $2 + \frac{W}{2}$ and $-2 - \frac{W}{2}$ respectively. The eigenfrequency spectrum width Δ therefore is

$$\Delta = W + 4.$$

Due to the localization nature of the system's eigenstates, the exponential decay

$$|A_{\nu,l}| \propto \exp\left(\frac{-|l - l_0|}{\eta(\lambda_\nu)}\right)$$

describes their asymptotic behaviour, with $\eta(\lambda_\nu)$ denoting the localization length and l_0 the position of the spatial centre of the NM. The localization length for (2.1) with weak uncorrelated disorder $W \leq 4$ and for eigenfrequencies close to the centre of the spectrum can be estimated as [Kramer et al. (1993)]

$$\eta(\lambda_\nu) \approx 24\frac{4 - \lambda_\nu^2}{W^2}.$$

An alternative computation approach of $\eta(\lambda_\nu)$ is by using the transfer matrix method, basing on the random matrix theory and various perturbative techniques [Ishii (1973); Crisanti et al. (1993); Kramer et al. (1993)]. Localized states of disordered systems can also be quantified using Lyapunov characteristic exponents (LCEs), intensity-intensity correlation functions and the participation number [Crisanti et al. (1993); Kramer et al. (1993); Laptyeva et al. (2014)]. As a disorder dependent quantity, the localization length is maximized in the centre, $\lambda_\nu = 0$, of the frequency band where $\eta(0) \approx 96/W^2$. Using the approach of perturbation theory, $\eta(0) \approx [\ln(W/(2e))]^{-1}$ for strong disorder $W \geq 4$ [Krimer and Flach (2010); Laptyeva et al. (2014)].
The level of localization of the modes can also be characterised by two commonly used quantities, namely, the second moment $m_2^{(\nu)}$ which is computed as

$$m_2^{(\nu)} = \sum_l (l_0 - l)^2 |A_{\nu,l}|^2$$

with $l_0 = \sum_l l|A_{\nu,l}|^2$ denoting the centre position of eigenstate ν. $m_2^{(\nu)}$ quantifies the degree of spreading of the ν^{th} eigenstate. The second quantity is the participation number P_ν which is computed as

$$P_\nu = \frac{1}{\sum_l |A_{\nu,l}|^4} \tag{2.5}$$

and estimates the number of sites in the mode with high energy density. Additionally, the effective distance V_ν between the exponential tails of the eigenstate ν can be computed as [Krimer and Flach (2010); Laptyeva et al. (2014)]

$$V_\nu = \sqrt{12 m_2^{(\nu)}} + 1. \tag{2.6}$$

Quantities P_ν and V_ν give the exact width of a flat, compactly distributed norm density distribution and have been used to approximate the spatial extent (localization volume) of eigenstate ν. However, for weak disorder and with the inclusion of fluctuations, the

calculation of P_ν gives a reduced value compared to the correct volume, while the V_ν does not. Therefore, we use V_ν to measure the localization volume of eigenstate ν. The averages

$$V = \overline{V}_\nu \tag{2.7}$$

and

$$P = \overline{P}_\nu \tag{2.8}$$

of these quantities over disorder realizations (sets of disorder numbers ϵ_l of the model (2.1)) and modes can be used to approximate the W-dependent localization volume and participation number respectively, of the NMs. For weak disorder, the average V scales as $3.3\eta(0)$ and it tends to 1 for sufficiently strong disorder [Krimer and Flach (2010)]. This therefore implies that the average spacing

$$d \approx \frac{\Delta}{V} \tag{2.9}$$

of NM eigenfrequencies in the range of the NM localization volume gives

$$d \approx \frac{\Delta W^2}{300}$$

for $W \leq 4$. The scales d and Δ are vital in determining the characteristics of wave packet evolution in nonlinear systems [Flach (2010); Laptyeva et al. (2014)].
Since NMs of disordered systems are spatially exponentially localized, an initially localized wave packet which covers a finite number L of sites will not spread beyond the extent of the NMs containing the excited sites. For an excitation well within the localization volume (i.e. $L \ll V$), the wave packet spreads to fill up the localization volume in an approximate integration time of $2\pi/d$ units [Flach (2010)]. However, there is no significant expansion of the wave packet observed when $L \geq V$. Wave packets which are under the influence of AL correspond to trajectories that evolve on tori in the phase space, following what is usually called quasi-periodic motion.
In two spatial dimensions, the Hamilton function for the Anderson model is [Laptyeva et al. (2012, 2014)],

$$H_{2A} = \sum_{k,l} \left[\epsilon_{k,l}|\psi_{k,l}|^2 - \left(\psi_{k,l+1}\psi^*_{k,l} + \psi_{k+1,l}\psi^*_{k,l} + \psi^*_{k,l+1}\psi_{k,l} + \psi^*_{k+1,l}\psi_{k,l}\right)\right],$$

with $\psi_{k,l}$ being a complex variable denoting the wave function at lattice site (k,l) and $\psi^*_{k,l}$ the corresponding complex conjugate. The random uncorrelated disorder $\epsilon_{k,l}$ is chosen uniformly from interval $[-W/2, W/2]$, where W is the strength of disorder. The corresponding equations of motion computed as $\dot{\psi}_{k,l} = \frac{\partial H_{2A}}{\partial(i\psi^*_{k,l})}$ are

$$i\dot{\psi}_{k,l} = \epsilon_{k,l}\psi_{k,l} - \left(\psi_{k-1,l} + \psi_{k+1,l} + \psi_{k,l-1} + \psi_{k,l+1}\right). \tag{2.10}$$

Similar to the 1D case, taking $\psi_{k,l}(t) = A_{k,l}e^{-i\lambda t}$ and substituting it in equation (2.10) we get the linear eigenvalue problem

$$\lambda A_{k,l} = \epsilon_{k,l}A_{k,l} - A_{k-1,l} - A_{k+1,l} - A_{k,l-1} - A_{k,l+1}. \tag{2.11}$$

For a large lattice, based on Theorem 1 [Gerschgorin (1931)] we see that the bounds of the eigenvalues λ_ν are $-4 + \epsilon_{k,l} \leq \lambda_\nu \leq 4 + \epsilon_{k,l}$, and therefore the frequency band is defined by the interval $[-4 - \frac{W}{2}, 4 + \frac{W}{2}]$.

We now highlight some literature on AL and the role of disorder in AL.
Experimental studies for the observation of AL in 1D and 2D models have been reported in light waves [Wiersma et al. (1997); Scheffold et al. (1999); Störzer et al. (2006); Schwartz et al. (2007); Lahini et al. (2008)], microwaves [Dalichaouch et al. (1991); Chabanov et al. (2000)], sound waves [Weaver (1990)], electron gases and matter-waves [Akkermans and Montambaux (2007)]. Billy et al. (2008), reported the experimental study and observation of AL using dilute BECs of ^{87}Rb prepared in an isotropic opto-magnetic hybrid trap. The experiment was performed as follows: a BEC was loaded onto an optical lattice and its expansion was confined by a magnetic trap [Dalfovo et al. (1999); Morsch and Oberthaler (2006)]. A disordered potential was created by an optical speckle field when a laser beam was passed through a diffusive plate [Freund (2007)]. The BEC was then allowed to diffuse across the optically generated disordered potential by turning off the magnetic trap. Feshbach resonances [Timmermans et al. (1999); Chin et al. (2010)] are responsible for reducing the influence of interactions between atoms in the condensate to a negligible level. On the other hand, deep optical potentials are responsible for compensating the influence of these interactions. The bosonian gas is non-interacting under these conditions and so a single wave function can be used to characterize it. Localization of the atomic wave function can be studied in situ, using fluorescence or absorption approaches in imaging the atomic density. Through this method, findings showing the presence of AL for BEC in one [Clément et al. (2005); Fort et al. (2005); Billy et al. (2008)], and three [Jendrzejewski et al. (2012); Kondov et al. (2011)] spatial dimensions random potentials have been reported.
Figure 2.2 illustrates the setup for the observation of AL in **(a)** the case of ultra-cold atoms in random potentials, **(b)** 1D disordered photonic lattices and **(c)** 2D disordered photonic lattices.

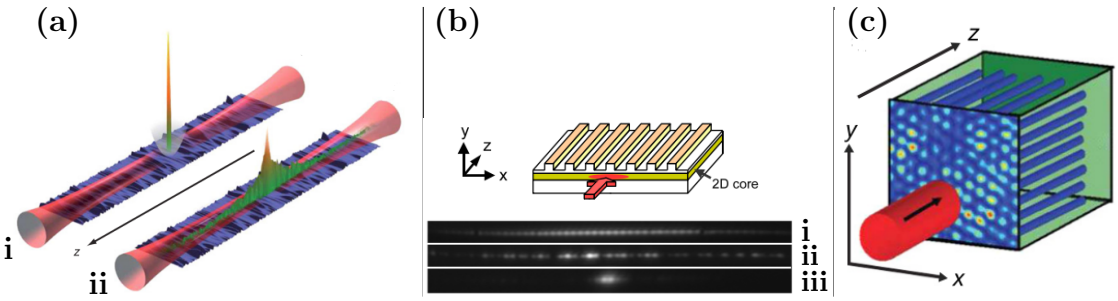

Figure 2.2: Experimental observation of AL. **(a)** from Billy et al. (2008): (**i**) the BEC is initially prepared in a magnetic trap and confined transversely to the z-axis in a 1D optical waveguide. (**ii**) When the trap is switched off, the condensate is allowed to expand along the waveguide superimposed with a speckle potential. The BEC stops its expansion after about 0.5s. **(b)** from Lahini et al. (2008): propagation of light in a 1D disordered waveguide lattice. The red arrow indicates the input beam, that generally covers a few lattice sites. Lower panels **i**–**iii** display the output light distribution in the case of (**i**) a periodic lattice, and (**ii**), (**iii**) a disordered lattice. **(c)** from Schwartz et al. (2007): a probe beam entering a disordered lattice, which is periodic in the two transverse dimensions (x and y) but invariant in the propagation direction (z). In this experiment a triangular (hexagonal) photonic lattice was used. The lattice is induced optically, by transforming the interference pattern among three plane waves into a local change in the refractive index, inside a photorefractive crystal. The input probe beam is always launched at the same location, while the disorder is varied in each realization of the performed experiments.

In Figure 2.2**(a) i** [from Billy et al. (2008)], a small BEC, of approximately 2×10^4

atoms, was formed in a hybrid trap combination of a loose magnetic longitudinal trap, and a horizontal optical waveguide ensuring a strong transverse confinement. A weak disordered optical potential, transversely invariant over the atomic cloud, was then superimposed. Figure 2.2**(a) ii** shows the BEC expansion on switching off the longitudinal trap, which, eventually localizes. Another experiment was performed in Lahini et al. (2008), by introducing disorder using a randomly varying waveguide width. The authors demonstrated the wave packet transitions from a ballistic expansion to exponential localization in coupled optical waveguide lattices in one dimension. The experimental setup of this investigation is shown in Figure 2.2**(b)** with the output observations in Figure 2.2**(b) i-iii**. In this demonstration, photonic lattices were used to observe AL in light. The distribution of the light intensity was visualized and measured at the lattice output. A year before the two studies shown in Figure 2.2 **(a)** and **(b)** were performed, experiments on the transverse localization of light in the presence of disorder potentials in 2D photonic lattices were performed [Schwartz et al. (2007)]. In the set up, shown in Figure 2.2 **(c)**, the random potential was controlled and varied by introducing disorder through a speckle beam. For weak disorder, ballistic transport was reported to turn diffusive and AL was observed for stronger disorder.
Our last consideration is Dalichaouch et al. (1991) where the authors reported microwave localization in two dimensional random media of dielectric cylinders and placed between two parallel aluminium plates. Due to the presence of localized modes, sharp peaks were observed in the transmission spectrum.

Disorder in a system can be generated in ways other than using a random uncorrelated distribution for example as discussed in our next model. We consider the Aubry-André model [Aubry and Andre (1980)], a model with correlated disorder, whose Hamiltonian is:

$$H_{AA} = \sum_{l} \left[\theta \cos(2\pi\alpha l)|\psi_l|^2 - \left(\psi_{l+1}\psi_l^* + \psi_{l+1}^*\psi_l\right)\right], \tag{2.12}$$

with ψ_l being a complex variable denoting the wave function for lattice site l and ψ_l^* the corresponding complex conjugate. $\alpha = \left(\sqrt{5}-1\right)/2$, and the parameter θ controls the magnitude of the on-site potentials, similar to the role of W in equation (2.1). With this model, we can observe NMs due to quasi-periodic potentials displaying a transition between localized and extended modes for specific values of θ. The corresponding equations of motion of Hamiltonian (2.12) are generated by $\dot{\psi}_l = \frac{\partial H_{1A}}{\partial(i\psi_l^*)}$ and yield the quasi-periodic version of the 1D DDLSE:

$$i\dot{\psi}_l = \theta \cos(2\pi\alpha l)\psi_l - \psi_{l+1} - \psi_{l-1}. \tag{2.13}$$

Setting $\psi_l(t) = A_l e^{-i\lambda t}$ in equation (2.13) we get the linear eigenvalue problem

$$\lambda A_l = \theta \cos(2\pi\alpha l)A_l - A_{l+1} - A_{l-1}. \tag{2.14}$$

In solving the eigenvalue problem (2.14) we use the matrix $\mathbf{A}$ whose entries $a_{k,l}$ are such that

$$a_{k,l} = \begin{cases} \theta\cos(2\pi\alpha k), & \text{for } k = l; \\ -1, & \text{for } k = l \pm 1; \\ 0, & \text{otherwise.} \end{cases}$$

In this case, the eigenvalues λ_ν of $\mathbf{A}$ are bounded as $-2 + \theta\cos(2\pi\alpha l) \leq \lambda_\nu \leq 2 + \theta\cos(2\pi\alpha l)$. The minimum and maximum possible values of the frequencies are therefore $-2-\theta$ and $2+\theta$ respectively. This model has been used to study the so-called Aubry-André localization [Roati et al. (2008); Edwards et al. (2008)] in ultra-cold atomic physics. In

an experimental manifestation of the phenomenon, a primary periodic lattice was created via interference patterns of two counter-propagating beams and quasi-periodicity was introduced by superimposing a weak secondary lattice with incommensurate wavelength [Guidoni et al. (1997)]. For the case when $\theta = 2$, Hamiltonian (2.12) is identical to the so-called Harper system [Harper (1955)]. This is a critical point whereby for $\theta < 2$ the states are localized and extended respectively in momentum and real space. For $\theta > 2$ the states have an exponential localization in real space with length $\eta = [ln(\theta/2)]^{-1}$ while they are extended in the momentum space [Aubry and Andre (1980); Sokoloff (1981)].

2.3 Nonlinear disordered models

Having discussed energy localization for linear disordered systems in the previous subsection, a fundamental question in this context is the effect of nonlinearities on the localization. This discussion has attracted extensive attention and studies in experiments [Pertsch et al. (2004); Schwartz et al. (2007); Roati et al. (2008); Lahini et al. (2008); Lucioni et al. (2011)], as well as in theory and simulations [Kopidakis et al. (2008); Pikovsky and Shepelyansky (2008); Flach et al. (2009a); Skokos et al. (2009); García-Mata and Shepelyansky (2009); Veksler et al. (2009); Mulansky et al. (2009); Mulansky and Pikovsky (2010); Laptyeva et al. (2010); Skokos and Flach (2010); Krimer and Flach (2010); Flach (2010); Johansson et al. (2010); Basko (2011); Bodyfelt et al. (2011b,a); Aubry (2011); Ivanchenko et al. (2011); Molina et al. (2012); Vermersch and Garreau (2012); Michaely and Fishman (2012); Basko (2012); Mulansky and Pikovsky (2012); Laptyeva et al. (2012); Milovanov and Iomin (2012); Lucioni et al. (2013); Vermersch and Garreau (2013); Mulansky and Pikovsky (2013); Skokos et al. (2013); Laptyeva et al. (2013); Tieleman et al. (2014); Ivanchenko et al. (2014); Antonopoulos et al. (2014); Ermann and Shepelyansky (2014); Laptyeva et al. (2014); Basko (2014); Flach et al. (2015); Martínez et al. (2016); Achilleos et al. (2016); Antonopoulos et al. (2017); Cherroret (2017); Iomin (2017); Achilleos et al. (2018)]. As mentioned before, two typical 1D Hamiltonian lattice models, namely, the DDNLS equation and the DKG anharmonic oscillator chain, have been used to numerically investigate the nonlinearity effect on the evolution of initially localized wave packets in heterogeneous media [Flach et al. (2009b); Skokos et al. (2009); Laptyeva et al. (2010); Skokos and Flach (2010); Flach (2010); Bodyfelt et al. (2011b,a); Skokos et al. (2013)]. The 1D and 2D versions of the DDNLS and DKG models are described in the next sections of this chapter with the DKG systems also further studied in the next chapters of this thesis.

2.3.1 The discrete nonlinear Schrödinger (DDNLS) equations

We start with the DDNLS system, whose Hamilton function is

$$H_{1D} = \sum_{l} \left(\epsilon_l |\psi_l|^2 - \left(\psi_{l+1}\psi_l^* + \psi_{l+1}^*\psi_l\right) + \frac{\beta}{2}|\psi_l|^4 \right), \tag{2.15}$$

where ψ_l are complex variables, with ψ_l^* being their complex conjugate values at lattice site l and $\beta > 0$ is quantifying the strength of the nonlinearity. The random disorder numbers ϵ_l, are chosen from a uniform distribution over the interval $\left[-\frac{W}{2}, \frac{W}{2}\right]$, where W denotes the disorder strength. Setting $\beta = 0$ in equation (2.15) gives the Anderson model of equation (2.1). The model of equation (2.15) describes a variety of nonlinear processes including localization of energy in chains of homogeneous anharmonic oscillators [Eilbeck et al. (1985); Kevrekidis et al. (2001); Eilbeck and Johansson (2003)] where $\epsilon_l = 0$, the light evolution through coupled optical waveguides in Kerr media [Kivshar and Agrawal

(2003)] and two-body interactions in ultracold atomic gases on an optical lattice within a mean-field approximation [Morsch and Oberthaler (2006)] among others. The equations of motion are

$$i\dot{\psi}_l = \epsilon_l\psi_l - \psi_{l+1} - \psi_{l-1} + \beta|\psi_l|^2\psi_l. \tag{2.16}$$

Besides the total energy H_{1D} (2.15), the equations (2.16) conserve the total norm

$$S = \sum_l |\psi_l|^2.$$

Since varying the total norm is equivalent to changing the nonlinearity strength β, often the norm is fixed at $S = 1$ and β is left as the control parameter. In a physical sense, the norm S could be used to denote the intensity of light or the density of an atomic condensate.

Model (2.15) can be naturally extended to two spatial dimensions over $N \times M$. The associated $2D$ DDNLS Hamiltonian is

$$H_{2D} = \sum_{l,m}\left(\epsilon_{l,m}|\psi_{l,m}|^2 - \left[\psi^*_{l,m}\left(\psi_{l,m+1} + \psi_{l+1,m}\right) + \psi_{l,m}\left(\psi^*_{l,m+1} + \psi^*_{l+1,m}\right)\right] + \frac{\beta}{2}|\psi_{l,m}|^4\right), \tag{2.17}$$

with the disorder $\epsilon_{l,m}$ again being randomly chosen from $[-W/2, W/2]$ where W and β are respectively disorder and nonlinearity strength. The equations of motion of (2.17) are

$$i\dot{\psi}_{l,m} = \epsilon_{l,m}\psi_{l,m} - \left(\psi_{l-1,m} + \psi_{l+1,m} + \psi_{l,m-1} + \psi_{l,m+1}\right) + \beta|\psi_{l,m}|^2\psi_{l,m}. \tag{2.18}$$

In general it is not possible to analytically integrate equations (2.16) and (2.18). However, for a coupled two oscillators lattice, system (2.17) becomes 1D and it is fully analytically integrable because of the DDNLS norm and energy conservation properties [Cruzeiro-Hansson et al. (1986); Eilbeck and Johansson (2003)]. In Ablowitz and Ladik (1976) and Ablowitz and Clarkson (1991) an integrable version of the DDNLS model was described, however, it has not yet been used to describe any physical processes. We also have nonlinear quasi-periodic chains which are described by taking the disorder ϵ_l of the 1D Hamiltonian (2.15) to be $\epsilon_l = \theta\cos(2\pi\alpha l)$, where the parameter θ and α are as described in equation (2.12). These quasi-periodic chains have been reported to describe the evolution of light pulses with high intensity in Kerr photonics [Lahini et al. (2009)] and the dynamical behaviour of interacting BECs in optic traps [Deissler et al. (2010); Lucioni et al. (2011)].

2.3.2 The Klein-Gordon (DKG) lattice models

The second model we focus on is the DKG lattice Hamiltonian model with a quartic nonlinearity in the potential and quadratic nearest-neighbour coupling. For physical applications, the DKG system is suitable for describing the dynamics of atomic arrays under the influence of external fields, e.g. the conservative nonlinear optical lattice vibration dynamics in molecular crystals [Ovchinnikov et al. (2001)]. The 1D Hamiltonian of the DKG model is

$$H_{1K} = \sum_l\left[\frac{p_l^2}{2} + \frac{\tilde{\epsilon}_l q_l^2}{2} + \frac{1}{2W}\left(q_{l+1} - q_l\right)^2 + \frac{q_l^4}{4}\right], \tag{2.19}$$

where q_l is the generalized coordinate and p_l the momentum of chain site l. $\tilde{\epsilon}_l \in [1/2, 3/2]$ are uncorrelated random values from a uniform distribution and W is the disorder strength. Therefore using Hamiltonian (2.19), the energy at site l can be defined as

$$h_l = \frac{p_l^2}{2} + \frac{\tilde{\epsilon}_l q_l^2}{2} + \frac{\left(q_l - q_{l-1}\right)^2 + \left(q_{l+1} - q_l\right)^2}{4W} + \frac{q_l^4}{4}, \tag{2.20}$$

where the interaction component $(q_{l+1}-q_l)^2/2$ of the energy (2.19) between sites $l+1$ and l is shared equally to contribute $(q_{l+1}-q_l)^2/4$ to each of the two sites.
The corresponding equations of motion $\frac{d\mathbf{q}}{dt}=\frac{\partial H}{\partial \mathbf{p}}$; $\frac{d\mathbf{p}}{dt}=-\frac{\partial H}{\partial \mathbf{q}}$ of Hamiltonian (2.19) lead to

$$\ddot{q}_l=-\tilde{\epsilon}_l q_l+\frac{1}{W}\left(q_{l+1}+q_{l-1}-2q_l\right)-q_l^3. \tag{2.21}$$

The total energy $H_{1K}=\sum_l h_l$ of the system is conserved by the equations (2.21). We also use the parameter H_{1K} to control the system's nonlinearity. The 2D KG Hamiltonian takes the form

$$H_{2K}=\sum_{l,m}\left[\frac{p_{l,m}^2}{2}+\frac{\tilde{\epsilon}_{l,m}q_{l,m}^2}{2}+\frac{1}{2W}\left(\left[q_{l,m+1}-q_{l,m}\right]^2+\left[q_{l+1,m}-q_{l,m}\right]^2\right)+\frac{1}{4}q_{l,m}^4\right], \tag{2.22}$$

where $q_{l,m}$ and $p_{l,m}$ are respectively the generalized coordinate and momentum of site (l,m), $\tilde{\epsilon}_{l,m}$ are random values chosen uniformly from $[\frac{1}{2},\frac{3}{2}]$ and W is the disorder strength. Using Hamiltonian (2.22), energy at site (l,m) is defined as

$$h_{l,m}=\frac{p_{l,m}^2}{2}+\frac{\tilde{\epsilon}_{l,m}q_{l,m}^2}{2}+\frac{1}{4W}\left(\left[q_{l,m+1}-q_{l,m}\right]^2+\left[q_{l+1,m}-q_{l,m}\right]^2+\left[q_{l,m-1}-q_{l,m}\right]^2+\left[q_{l-1,m}-q_{l,m}\right]^2\right)+\frac{1}{4}q_{l,m}^4, \tag{2.23}$$

and the equations of motion corresponding to (2.22) are

$$\ddot{q}_{l,m}=-\tilde{\epsilon}_{l,m}q_{l,m}+\frac{1}{W}\left(q_{l-1,m}+q_{l+1,m}+q_{l,m-1}+q_{l,m+1}-4q_{l,m}\right)-q_{l,m}^3. \tag{2.24}$$

Similar to the DDNLS Hamiltonian models in equations (2.15) and (2.17), the linear parts of Hamiltonians (2.19) and (2.22) can be reduced to the Anderson model in one and two dimensions respectively. This explains the exponential localization of all harmonic eigenstates of the DKG models. By neglecting the nonlinear terms q_l^4 in equation (2.19) and $q_{l,m}^4$ in equation (2.22) and taking the ansatz $q_l=A_l e^{-i\omega t}$ and $q_{l,m}=A_{l,m}e^{-i\omega t}$ for the 1D and 2D models respectively, the DKG Hamiltonians are reduced to the same linear eigenvalue problems provided in equations (2.3) and (2.11), using the relations $\lambda=W\omega^2-W-2$, $\epsilon_l=W(\tilde{\epsilon}_l-1)$ and $\epsilon_{l,m}=W(\tilde{\epsilon}_{l,m}-1)$. The corresponding eigenvalues (square frequencies) ω_ν^2 lie in the interval $[1/2,4/W+3/2]$. In the limit of small energies and amplitudes, a map

$$\beta S\approx 3WH \tag{2.25}$$

providing a relationship between parameters W and H of the DKG systems and β and S of the DDNLS model exists [Kivshar and Peyrard (1992); Kivshar (1993); Johansson and Rasmussen (2004); Johansson (2006)].
In Table 2.1, we present the exact correspondences (and the main characteristics) between the 1D DDNLS and DKG models for small nonlinearities. Because of the existing mapping between these two models, we only give a more detailed discussion on theoretical estimates in Section 2.3.3 for the DDNLS system and adapt the results for the DKG model. Existing simulations of these two models show qualitatively similar dynamical behaviour for a variety of energy and disorder parameters [Flach et al. (2009a); Skokos et al. (2009); Laptyeva et al. (2010); Bodyfelt et al. (2011b)]. Compared to the DDNLS model, the DKG system allows up to a multiplicative factor of 10^2 less numerical integration time for a fixed accuracy irrespective of the systems' final evolution time.

	DDNLS	mapping	DKG
Disorder	ϵ_l	$\epsilon \mapsto \tilde{\epsilon}_l = \frac{\epsilon_l}{W} + 1$	$\tilde{\epsilon}_l$
Eigenfrequency	λ_ν	$\lambda_\nu \mapsto \omega_\nu^2 = \frac{\lambda_\nu + W + 2}{W}$	ω_ν^2
Frequency spectrum width	$\Delta_D = W + 4$	$\Delta_D \mapsto \Delta_K = \frac{\delta_D}{W}$	$\Delta_K = 1 + \frac{4}{W}$
Localization volume	$\mathrm{V}_D \sim \begin{cases} \frac{330}{W^2} & W \to 0 \\ 1 & W \to \infty \end{cases}$	$V_D \mapsto V_K = V_D$	$\mathrm{V}_K \sim \begin{cases} \frac{330}{W^2} & W \to 0 \\ 1 & W \to \infty \end{cases}$
Average spacing of frequencies	$\mathrm{d}_D \sim \begin{cases} W^2 & W \to 0 \\ W & W \to \infty \end{cases}$	$d_D \mapsto d_K = \frac{d_D}{W}$	$\mathrm{d}_K \sim \begin{cases} W & W \to 0 \\ constant & W \to \infty \end{cases}$
Nonlinear frequency shift	$\delta_D \sim \beta n$		$\delta_K \sim \frac{3H_K}{2}$

Table 2.1: Correspondence between characteristic quantities of the DDNLS model to the DKG model. Based on Table 1 of Bodyfelt et al. (2011b).

A quasi-periodic variation of the DKG chain [Laptyeva et al. (2014)] is governed by the Hamiltonian

$$H_{q1K} = \sum_l \left[\frac{p_l^2}{2} + \frac{q_l^2(2 + \cos(2\pi\alpha l))}{4} + \frac{1}{4\theta}(q_{l+1} - q_l)^2 + \frac{q_l^4}{4} \right],$$

where the parameters α and θ have the same meaning as for the Aubry-Andr*é* model (2.12). The system's equations of motion are

$$\ddot{q}_l = -\frac{q_l(2 + \cos(2\pi\alpha l))}{2} + \frac{1}{2\theta}(q_{l+1} + q_{l-1} - 2q_l) - q_l^3.$$

We also note that the DDNLS and DKG systems discussed have quartic nonlinearity in their Hamiltonians. However, in some cases the index of nonlinearity may be parametrized to get a higher or fractional order for example in some optical materials, doped glasses, semiconductors and at the crossover between the molecule dimer BEC and Bardeen-Cooper-Schrieffer (BCS) pairs in ultra-cold Fermi gases [Yan et al. (2011)]. A fairly detailed coverage on parametrized nonlinearity index, which we recommend for further reading, has been included in Laptyeva et al. (2014).

2.3.3 Theoretical estimations

The localized nature of NMs in disordered media hinders the spreading of energy if modes do not interact with each other. The presence of nonlinearity induces interactions between the NMs of the system, hence spreading of the energy is possible. The theory of the spreading mechanism in such cases has been explained in Flach et al. (2009b), Skokos et al. (2009), Flach (2010), Laptyeva et al. (2010), Bodyfelt et al. (2011b) and Flach et al. (2015). Here we highlight the key ideas discussed in these papers.

Extremely high energies lead to a strong nonperturbative effect of nonlinearity, and so spreading of the energy is not realized. On the other hand, very low energies create AL effects in the system in which case the energy never spreads or it takes a long time before spreading. The fast spreading of the wave packet occurs at moderate energies of the system. In order to understand the energy spreading mechanism, we use the NM space in studying the system. The equations of motion for the DDNLS system in NM form can be written using the transformation $\psi_l = \sum_\nu A_{\nu,l}\phi_\nu$, where $\phi_\nu = \phi_\nu(t)$ is the amplitude

of NM ν at time t. Using the equations of the eigenvalue problem (2.3) and taking into account the orthogonality of the NMs, we revise the equations of motion (2.16) to become

$$i\dot{\phi}_\nu = \lambda_\nu \phi_\nu + \beta \sum_{\nu_1,\nu_2,\nu_3} I_{\nu,\nu_1,\nu_2,\nu_3} \phi^*_{\nu_1} \phi_{\nu_2} \phi_{\nu_3},$$

where $I_{\nu,\nu_1,\nu_2,\nu_3}$ is the overlap integral

$$I_{\nu,\nu_1,\nu_2,\nu_3} = \sum_l A_{\nu,l}, A_{\nu_1,l}, A_{\nu_2,l}, A_{\nu_3,l}.$$

The nonlinear interactions of modes are of finite range, because of the exponential localized nature of the NMs, and thus each NM effectively couples with finitely many neighbouring modes. This finite number of neighbouring partner modes with effective coupling to a NM ν is on average the so-called localization volume V_ν. The eigenvalues of the neighbouring eigenstates of ν will be different in general, but bounded within the frequency spectrum band which has length Δ. This therefore means that the eigenvalues of the NMs which are neighbours of ν within V_ν have an average frequency spacing $d_\nu \approx \Delta/V_\nu$. Averaging over all NMs, gives an average spacing d of the eigenvalues where $d \approx \Delta/V$, and $V = \overline{V}_\nu$. In this case $\overline{V}_\nu$ is used to denote the average of quantity V_ν over all disorder realisations. The strength of the NM interaction is proportional to the DDNLS norm density and to the energy density for the DKG model. In general, we can define two norm densities $n_l = |\psi_l|^2$ and $n_\nu = |\phi_\nu|^2$ in the real and NM spaces respectively, for the DDNLS system, if the wave packet has spread far enough. The averages of these two densities over a number of different disorder realizations give practically the same characteristic norm density n. Therefore the presence of nonlinearity induces a frequency shift $\delta_{1D} = \beta n$ for the DDNLS model and $\delta_{1K} = 3H_{1K}/2$ for the DKG system on a single oscillator [Skokos et al. (2009); Laptyeva et al. (2010)].

Consider an excitation of L central neighbouring oscillators with a constant total norm $n \neq 0$, a random on-site phase for all sites and a vanishing norm for the remaining oscillators in the lattice. This, for the 1D DKG model, corresponds to giving the same energy

$$h = \frac{H_{1K}}{L}$$

to each of the L oscillators. This can be easily achieved by setting the momentum of each oscillator to be $\sqrt{2h}$ with randomly assigned signs while their initial displacements are set to zero.

For very high energies (or energy densities), i.e. when the size of the frequency shift δ_{1D} induced by the nonlinearity is larger than the frequency spectrum width Δ_D, the sites where the excitation takes place will instantly be set out of resonance compared to the non excited neighbouring sites. This leads to the formation of structures similar to discrete breathers that persist for a very long time. That is to say, a large section of the wave packet will be self-trapped [Kopidakis et al. (2008); Skokos et al. (2009)]. Unlike AL, this phenomenon requires gaps to exist in the spectrum of the linear wave equations in order to occur [Flach and Willis (1999); Flach and Gorbach (2008)]. For a frequency shift $\delta_{1D} \geq 2$ in the DDNLS model, some wave packet sites are tuned out of resonance, therefore self-trapping behaviours can be observed. However for relatively small frequency shifts $\delta_{1D} < \Delta_D < 2$, the self-trapping tendencies are avoided and propagation of the wave packet will be realised. A NM in the wave packet resonantly interacts with it's neighbours when the size of the frequency shift δ_{1D} is greater than the average spacing d_{1D} of the NMs. For this reason, this dynamical regime is called the 'strong chaos' regime. The NMs weakly interact with each other when δ_{1D} is smaller than d_{1D} and so this is called the

'weak chaos' regime [Laptyeva et al. (2010)]. In general, the width of a propagating wave packet will increase (but with a fixed total norm) and so its norm density will decrease. This means that the nonlinear frequency shift will decrease and therefore the dynamics will crossover into the asymptotic (i.e. limiting behaviour of the dynamics in time) weak chaos regime from the transient strong chaos regime at later times.
Only weak chaos and selftrapping regimes are present whenever only a single site is excited [Pikovsky and Shepelyansky (2008); Skokos et al. (2009); Flach et al. (2009a)]. For sites excitations of the order of the localization volume, we can summarize the dynamical regimes as follows:

i. *Selftrapping* regime: $\delta_{1D} > \Delta_D > 2$
ii. *Strong chaos* regime: $\Delta_D > \delta_{1D} > d_{1D}$
iii. *Weak chaos* regime: $\Delta_D > d_{1D} > \delta_{1D}$

In Figure 2.3 we illustrate these dynamical regimes in a parametric space for both the DDNLS and DKG models when the number of initially excited neighbouring sites is equal to the localization volume V.

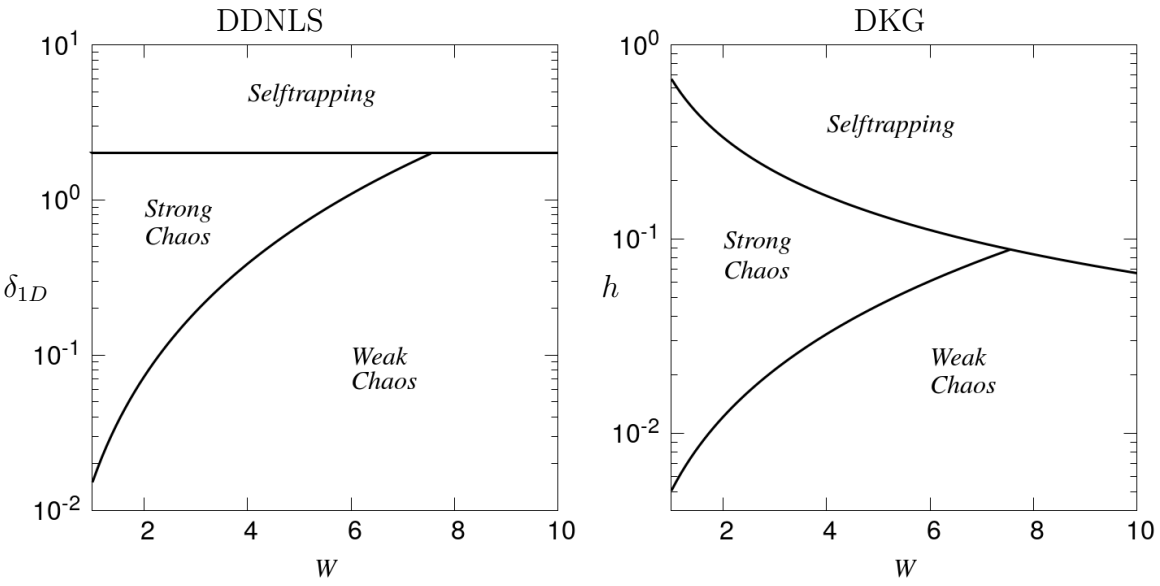

Figure 2.3: The parameter space (W, δ_{1D}) and (W, h) respectively showing the dynamical regimes of the dynamics for the DDNLS model (2.15) [left panel] and the DKG system (2.19) [right panel]. Parameters W, δ_{1D} and h respectively denoting the disorder strength, the DDNLS (model) nonlinear frequency shift and the uniformly distributed initial energy (2.20) at each site. The plots are based on Fig. 1 of Skokos et al. (2009), Figure 1.2 of Gkolias (2013) and Figures 10 and 16 of Laptyeva et al. (2014).

The DDNLS model's nonlinear frequency shift $\delta_{1D} \sim \beta n$ of the initial excitation is equivalent to the energy density h in the DKG system. The regime boundary curves for the DDNLS model (left panel of Figure 2.3) are represented by the equations $\delta_{1D} = d_{1D}$ and $\delta_{1D} = 2$. The lower regime boundary estimates for the weak chaos case are analytically found using $d_{1D} = \Delta_{1D} W^2/330$. To get the boundary curves for the DKG system, we use the equations involving δ_{1D} and the transformation (2.25) which practically maps the regime regions of the DDNLS model to the DKG system.
Chaotic dynamics takes place primarily due to the nonlinear interaction of modes [Skokos et al. (2009); Flach et al. (2009b)] in the lattice interior. As a consequence, the modes close to the wave packet boundaries get heated. The wave packet spreading mechanism depends on either a normal mode on the cold exterior (bordering the wave packet) being excited resonantly by some particular normal mode within the packet, or incoherently

heated by the packet. It was conjectured [Laptyeva et al. (2010); Flach (2010)] that an exterior mode μ is excited according to the equation

$$i\dot{\phi}_\mu \approx \lambda_\mu \phi_\mu + \beta n^{\frac{3}{2}} \mathcal{P}(\beta n) f(t)$$

with $\mathcal{P}(\beta n) \approx 1 - exp(\frac{-\beta n}{d})$ denoting the probability, for a mode excited to average packet norm density n, to be resonant with at least one triplet of other modes at a specific value of the interaction parameter β [Flach (2010); Krimer and Flach (2010)] while $f(t)$ denotes a stochastic force. The evolution of the norm, averaged over all modes, is therefore given by

$$|\phi(t)|^2 \propto \beta^2 n^3 [\mathcal{P}(\beta n)]^2 t.$$

$|\phi(t)|^2$ will be equal to the wave packet norm n at a time $T \propto \beta^{-2} n^{-2} [\mathcal{P}(\beta n)]^{-2}$, after which the mode forms part of the wave packet. We can characterise the rate of norm diffusion using the inverse of T which we denote as D,

$$D(t) = T^{-1} \propto \beta^2 n^2 [\mathcal{P}(\beta n)]^2.$$

Thus, the resonance probability $\mathcal{P}(\beta n)$ largely dictates the nature of the chaotic dynamics whether it is characterised as strong or weak chaos. Since the second moment,

$$m_2 = \sum_l (l - \bar{l})^2 n_l, \tag{2.26}$$

where $\bar{l} = \sum_l l n_l$ is the centre of the norm distribution $\{n_l\}_l$ of the wave packet, is approximately equal to the inverse of the square packet norm, i.e. $m_2 \approx 1/n^2$, and we also have the diffusion equation $m_2 \propto Dt$, then

$$\frac{1}{n^2} \propto \beta \left[1 - \exp\left(-\frac{\beta n}{d}\right)\right] t^{\frac{1}{2}}. \tag{2.27}$$

Equation (2.27) also determines the subdiffusive spreading for the strong and weak chaos regimes as

$$m_2(t) \propto \begin{cases} \beta t^{\frac{1}{2}}, & \text{for strong chaos,} \\ d^{-\frac{2}{3}} \beta^{\frac{4}{3}} t^{\frac{1}{3}}, & \text{for weak chaos.} \end{cases}$$

Thus, for 1D systems, this yields propagation laws in terms of the second moment m_2 (2.26) for the weak and strong chaos cases of the wave packet. That is to say, the second moment increases as $m_2(t) \propto t^{\frac{1}{3}}$ in the weak chaos and $m_2(t) \propto t^{\frac{1}{2}}$ in the strong chaos regime.

A similar theoretical analysis [Flach (2010); Laptyeva et al. (2012)] for the 2D systems gives the following spreading laws

$$P(t), m_2(t) \propto \begin{cases} t^{\frac{1}{3}}, & \text{for strong chaos,} \\ t^{\frac{1}{5}}, & \text{for weak chaos.} \end{cases}$$

2.3.4 Other disordered systems

Besides the DDNLS and DKG models, various 1D coupled oscillatory lattice models have been intensively studied in a variety of physical disciplines for example biology, biophysics and material science [Ford (1992); Braun and Kivshar (2004); Peyrard (2004)]. An enormous number of models and their applications have been reported, including but not limited to the Fermi–Pasta–Ulam-Tsingou (FPUT) chains [Fermi et al. (1955)], the Frenkel–Kontorova model [Kontorova and Frenkel (1938); Braun and Kivshar (2004)] and the Peyrard–Bishop Dauxois (PBD) Deoxyribo-Nucleic Acid (DNA) model [Dauxois et al. (1993)].

The disordered Fermi Pasta Ulam Tsingou (DFPUT) model

The disordered version of the FPUT model [Fermi et al. (1955)] was used in Li et al. (2001) and Dhar and Saito (2008) to investigate the heterogeneity effect on thermal conductivity in one dimensional mass-disordered harmonic and anharmonic lattices. In contrast to the conclusions of Li et al. (2001), who reported that disorder induces a finite thermal conductivity at low temperatures, Dhar and Saito (2008) found no evidence of a finite-temperature transition in the conducting properties of the DFPUT model. They instead, revealed that disorder dominates transport properties of systems of small sizes at low temperatures. For systems of large size, the heat current J was found to depend on the lattice size N as $J \propto 1/N^{2/3}$. A comparative study of chaos and AL in the DFPUT and Hertzian [Johnson (1985)] models describing granular chains has been presented in Ngapasare et al. (2019), where, the discontinuous nonlinearity of the Hertzian system has been found to trigger energy spreading at lower energies. The DFPUT model, however, was shown to exhibit an alternate behaviour between localized and delocalized chaos which is strongly dependent on the type of initial excitation.

The Frenkel–Kontorova model

Frenkel-Kontorova system is a simple model that has become one of the fundamental and universal tools of low-dimensional nonlinear physics. It describes the dynamics of a chain of particles with nearest neighbour coupling and the influence of an external periodic potential [Braun and Kivshar, S. (1998)]. This model was first mentioned by Prandtl (1928) and Dehlinger (1929). Then Frenkel and Kontorova [Kontorova and Frenkel (1938)] worked independently on the same model. This model has been used in describing the dynamics of a crystal lattice near a soliton (a wave packet propagating at a constant velocity while maintaining its shape) [Sirovich et al. (2005)]. Frenkel and Kontorova derived an analytical solution for a moving single soliton which was generated for large enough displacement of the atoms [Filippov (2000)]. A detailed discussion of the model including it's applications is given in Braun and Kivshar (2004).

DNA models

The dynamical behaviour of base pairs in the DNA molecule has been studied using various models. A comprehensive review of some of the various models has been presented in Manghi and Destainville (2016). One of these models, namely the PBD model, was introduced in Dauxois et al. (1993), and it has since been used to explain a number of observations from experiments performed in relation to base pair openings in DNA. For specific temperatures, numerical simulations showed good qualitative description of the amplitude fluctuation openings and emergence of denaturation bubbles from thermal fluctuations. Numerical studies of the PBD model in Hillebrand et al. (2019) revealed that chaoticity increases with energy and this behaviour is independent of the heterogeneity composition of base pairs.

2.4 Measures of spreading

In our study we concentrate on the energy spreading behaviour for the DKG models in one and two spatial dimensions. We present here the spreading measures we use in our analysis.

2.4.1 1D DKG model

As we explained in Section 2.3.2, the energy h_l of the oscillator at site l of the 1D DKG model (2.19) is given by

$$h_l = \frac{p_l^2}{2} + \frac{\tilde{\epsilon}_l q_l^2}{2} + \frac{(q_{l-1} - q_l)^2 + (q_{l+1} - q_l)^2}{4W} + \frac{q_l^4}{4}, \tag{2.28}$$

and thus the energy density distribution is defined by

$$\xi_l = \frac{h_l}{H_{1K}}. \tag{2.29}$$

The extent of the wave packet can be measured by the second moment m_2 and the participation number P. The second moment m_2 estimates the wave packet extent of spreading and is given by

$$m_2 = \sum_l (l - \bar{l})^2 \xi_l \tag{2.30}$$

where $\bar{l} = \sum_l l\xi_l$ denotes the centre of the distribution $\{\xi_l\}_l$ (2.29).
The participation number

$$P = \left[\sum_l \xi_l^2\right]^{-1}, \tag{2.31}$$

on the other hand, estimates the number of sites with the highest energy. When the total energy H_{1K} of the system is equally distributed amongst L oscillators then $P = L$, with the particular case of a single site excitation giving $P = 1$. In all other cases, P lies between one and the lattice size. We note that P is equivalent to the Renyi entropy I_2 where

$$I_r = \frac{1}{1-r} \ln \sum_l \xi_l^r.$$

2.4.2 2D DKG model

For the 2D DKG model (2.22), the energy $h_{l,m}$ at site (l, m) is given by

$$h_{l,m} = \frac{p_{l,m}^2}{2} + \frac{\epsilon_{l,m}}{2} q_{l,m}^2 + \frac{q_{l,m}^4}{4} + \frac{1}{4W}\left[(q_{l+1,m} - q_{l,m})^2 + (q_{l,m+1} - q_{l,m})^2\right], \tag{2.32}$$

and thus the energy density distribution is defined by

$$\xi_{l,m} = \frac{h_{l,m}}{H_{2K}}. \tag{2.33}$$

The second moment m_2 is given by

$$m_2 = \sum_{l,m} ||(l, m) - \overline{(l, m)}||^2 \xi_{l,m} \tag{2.34}$$

with $\overline{(l, m)} = \sum_{l,m}(l\xi_{l,m}, m\xi_{l,m})$ denoting the position of the energy distribution $\{\xi_{l,m}\}_{l,m}$ centre and $||\cdot||$ denoting the Euclidean norm.
The participation number P is given by

$$P = \frac{1}{\sum_{l,m} \xi_{l,m}^2}, \tag{2.35}$$

such that $P = N{\cdot}M$ whenever the total energy of the system is equally distributed amongst an $N \times M$ rectangular array of $N{\cdot}M$ oscillators (where $N \times M$ is a sub-array of the entire lattice). For a general distribution of the energy amongst the oscillators, P always lies between one and the lattice size.

2.5 Transition from order to disorder

In Section 2.3.3, we used the theory of NMs to describe the temporal behaviour of the second moment m_2 (2.30 and 2.34) of the wave packet as a quantity for classifying the dynamics of 1D and 2D disordered Hamiltonian systems in categories of chaotic regimes. This shows the power of NMs, as inherent structures of a system, in revealing the characteristics a system's dynamics. Here we probe the NM properties for Hamiltonian lattices over a transition in the heterogeneity spectrum from order at one end to disorder at the other end. In order to do this, we consider a 1D linear version of the DKG model (2.19) to which we introduce parameters, D (related to the site disorder) and $\mathcal{W}$ (regulates the size of neighbour interactions). D together with $\mathcal{W}$ determine the strength of disorder in our model. Starting from an ordered version of this new model, we study the properties of the NMs as we move towards a disordered system by changing D and keeping $\mathcal{W}$ constant. In the process, we monitor changes in the qualitative structure, eigenfrequencies, average participation number P (2.8) and average localization volume V (2.7) of the NMs, studying the changes in the width Δ of the frequency spectrum, and the average spacing d (2.9) of the frequencies of the modes.

2.5.1 The modified Klein-Gordon model

We start by performing an analysis for the linear version LDKG of the 1D DKG model (2.19) whose Hamiltonian function is

$$H_K = \sum_l \left[\frac{p_l^2}{2} + \frac{\tilde{\epsilon}_l q_l^2}{2} + \frac{1}{2\mathcal{W}} (q_{l+1} - q_l)^2 \right], \tag{2.36}$$

where again q_l and p_l are respectively representing the generalized position and momentum of oscillator l. The disorder coefficients $\tilde{\epsilon}_l$ take uncorrelated random values chosen from the interval $[1-D, 1+D]$ following a probability distribution with function $\mathcal{P}(\tilde{\epsilon}_l) = 1/(2D)$. The parameter D defines the interval width from which $\tilde{\epsilon}_l$ is chosen, while $\mathcal{W} > 0$ determines the strength of nearest neighbor interaction. In our investigation, we use $0 \leq D \leq 1/2$ with $D = 0$ (i.e. setting $\epsilon_l = 1$ for all sites) corresponding to the ordered version of Hamiltonian (2.36). For a fixed $\mathcal{W}$, when D increases from 0, the system shifts from ordered to disordered while keeping the strength of nearest neighbor interactions constant.
The equations of motion of Hamiltonian (2.36) are

$$\dot{q}_l = p_l\,; \qquad \dot{p}_l = -\left[\tilde{\epsilon}_l q_l + \frac{1}{\mathcal{W}} (2q_l - q_{l-1} - q_{l+1}) \right], \tag{2.37}$$

where as usual the dot denotes the time t derivative. Using the ansatz $q_l = A_l e^{i\omega t}$, where A_l is the amplitude of oscillator l, equation (2.37) leads to the eigenvalue problem

$$\omega^2 A_l = \frac{1}{\mathcal{W}} \left[(\mathcal{W}\tilde{\epsilon}_l + 2) A_l - A_{l-1} - A_{l+1} \right]. \tag{2.38}$$

The system's NMs are the normalized eigenvectors $A_{\nu,l}$, $\nu = 1, 2, \ldots, N$, with $\sum_l A_{\nu,l}^2 = 1$, and the eigenvalues ω_ν^2 are the corresponding squared frequencies of these modes. System (2.36) corresponds to the Anderson model (2.1) by considering the relations

$$\lambda = \omega^2 \mathcal{W} - \mathcal{W} - 2, \tag{2.39}$$
$$\epsilon_l = \mathcal{W}(\tilde{\epsilon}_l - 1), \tag{2.40}$$
$$W = 2D\mathcal{W}, \tag{2.41}$$

where λ, ϵ_l and W are as defined for the model (2.1) with $0 < W \leq \mathcal{W}$. In this way the eigenvalue problems (2.3) and (2.38) and consequently the Hamiltonian systems (2.1) and (2.36), become identical. Finding the solution of the eigenvalue problem (2.38) involves the diagonalization of the $N \times N$ tridiagonal matrix $\mathbf{B}$ with elements

$$b_{l,l-1} = b_{l,l+1} = -\frac{1}{\mathcal{W}}, \quad b_{l,l} = \tilde{\epsilon}_l + \frac{2}{\mathcal{W}}, \tag{2.42}$$

and $b_{k,l} = 0$ otherwise, for $l, k = 1, 2, \ldots, N$. Once again, the direct application of Theorem 1 [Gerschgorin (1931); Wolkowicz and Styan (1980)] to matrix $\mathbf{B}$ (2.42) gives $\tilde{\epsilon}_l \leq \omega^2(D) \leq \tilde{\epsilon}_l + 4/\mathcal{W}$. The minimum $\omega_-^2(D)$, and maximum $\omega_+^2(D)$, possible values of the squared frequencies are respectively $\omega_-^2(D) = 1 - D$ and $\omega_+^2(D) = 1 + D + 4/\mathcal{W}$ since $\tilde{\epsilon}_l \in [1 - D, 1 + D]$. The width of the squared frequency (ω_ν^2) spectrum therefore is

$$\Delta_K(D) = 2D + \frac{4}{\mathcal{W}}. \tag{2.43}$$

Setting $\tilde{\epsilon}_l = 1 \; \forall \; l = 1, 2, \ldots, N$ in (2.36), i.e. $D = 0$, gives an ordered linear system where the analytic solution of the corresponding eigenvalue problem [Losonczi (1992); Yueh (2005); Borowska and Łacińska (2015); Da Fonseca and Kowalenko (2019)] is

$$\omega_\nu^2(D = 0) = 1 + \frac{2}{\mathcal{W}}\left[1 - \cos\left(\frac{\nu\pi}{N+1}\right)\right], \quad \nu = 1, 2, \ldots, N.$$

For each mode ν, $\omega_\nu^2(0)$ is bounded below by 1 and above by $1 + 4/\mathcal{W}$, thereby giving a maximum spectrum width $\Delta_K = \frac{4}{\mathcal{W}}$ in accordance with (2.43).
The presence of the disorder range width D and the parameter $\mathcal{W}$ in the LDKG model (2.36) allows for the alteration of the system's disorder strength by modifying D or $\mathcal{W}$ or both parameters, while for the equivalent DDLSE system (2.1) we can only change the disorder strength by varying W. In the studies of the DKG and LDKG models [Flach et al. (2009a); Skokos et al. (2009); Laptyeva et al. (2010); Skokos et al. (2013)] performed so far, the value of D was fixed at $D = 1/2$ and various values of $W \geq 1$ (implying $\mathcal{W} \geq 1$ through (2.41)) used. As $W \to 0$, the nearest neighbor interaction term becomes more significant compared to the on-site potential $\tilde{\epsilon}_l q_l^2/2$ in Hamiltonian (2.36) and the system tends to a more ordered one. In [Krimer and Flach (2010)], the focus was on strong disorder and so the properties of NMs for the DDLSE (2.1) were discussed for disorder parameter values $W \geq 1$. For the modified model (2.36) [and equivalently for the DDLSE (2.1)], by changing the disorder through increasing D starting from 0 while keeping $\mathcal{W}$ fixed, we obtain a transition from order to disorder. By considering equations (2.39)–(2.41), we can use analogous results obtained for the DDLSE (2.1) [Kramer et al. (1993); Krimer and Flach (2010)] to deduce the results for the LDKG model (2.36). A NM ν of the system (2.36) has an asymptotic exponential spatial decay described by

$$A_{\nu,l} \sim \exp\left(-\frac{|l - l_0|}{\eta_\nu}\right),$$

with $l_0 = \sum_l l A_{\nu,l}^2$ denoting the mean spatial position of the NM and η_ν is the localization length [Anderson, P. (1958); Kramer et al. (1993); Krimer and Flach (2010)], whose dependence on D and ω_ν^2 is given by

$$\eta_\nu(D, \omega_\nu^2) = \frac{24\left[4 - (\omega_\nu^2\mathcal{W} - \mathcal{W} - 2)^2\right]}{4D^2\mathcal{W}^2}, \tag{2.44}$$

where $D\mathcal{W} \leq 2$. We note that D and $\mathcal{W}$ affect Δ_K (2.43) and η_ν (2.44) in different ways, since they do not appear in each one of these two expression exclusively as a product $D\mathcal{W}$

or a quotient $D/\mathcal{W}$ (or $\mathcal{W}/D$). By solving the equation $\frac{d}{d\omega_\nu^2}\eta_\nu = 0$, we find that the most extended NMs (i.e. NMs with the largest localization length η_0 at a particular value of D) appear whenever $\omega_\nu^2 = 1 + \frac{2}{\mathcal{W}}$. In this case

$$\eta_\nu\left(D, \omega_\nu^2 = 1 + \frac{2}{\mathcal{W}}\right) = \eta_0 = \frac{24}{D^2\mathcal{W}^2}, \tag{2.45}$$

for $D\mathcal{W} \leq 2$. This is a generalization over D, of the findings of Kramer et al. (1993) and Krimer and Flach (2010) where the localization length is reported to be maximized for frequencies at the centre of the band width for $D = 0.5$.

2.5.2 Properties of NMs

In this investigation, we fix $\mathcal{W} = 4$ and systematically change D from values very close to $D = 0$ (system's state of order) to $D = 1/2$ (system's state of disorder). This set up leads to $W = 8D$ (2.41) with the square frequency band width $\Delta_K = 2D + 1$ (2.43). Computation of NMs for a lattice of size N implies working with an $N \times N$ matrix. Therefore very large sizes of N are impossible to use in numerical computations. For this reason, we use $D-$dependent lengths of up to a maximum length $N = 50{,}000$. We note that the pair of parameters $\mathcal{W} = 4$ and $D = 1/2$ is a typical combination of values that have been used in several studies of disordered systems including Flach et al. (2009a), Skokos et al. (2009), Laptyeva et al. (2010) and Skokos et al. (2013). In order to perform a statistical analysis of the NM properties, we perform simulations over $n_d = 100$ disorder realizations for a fixed value of $D \in (0, 0.5]$. We order the NMs either by increasing value of their squared frequency ω^2, or of their mean spatial position l_0 for each value of D. Since the frequency band and it's width Δ_K depend on D, we use the normalized square frequency

$$\omega_{\nu,n}^2 = \frac{\omega_\nu^2 - \omega_{\nu,-}^2}{\Delta_K} = \frac{\omega_\nu^2 - \omega_{\nu,+}^2}{\Delta_K} + 1 = \frac{\omega_\nu^2 + D - 1}{2D + 1}, \tag{2.46}$$

of the NM to allow for a direct comparison of cases with different values of D.

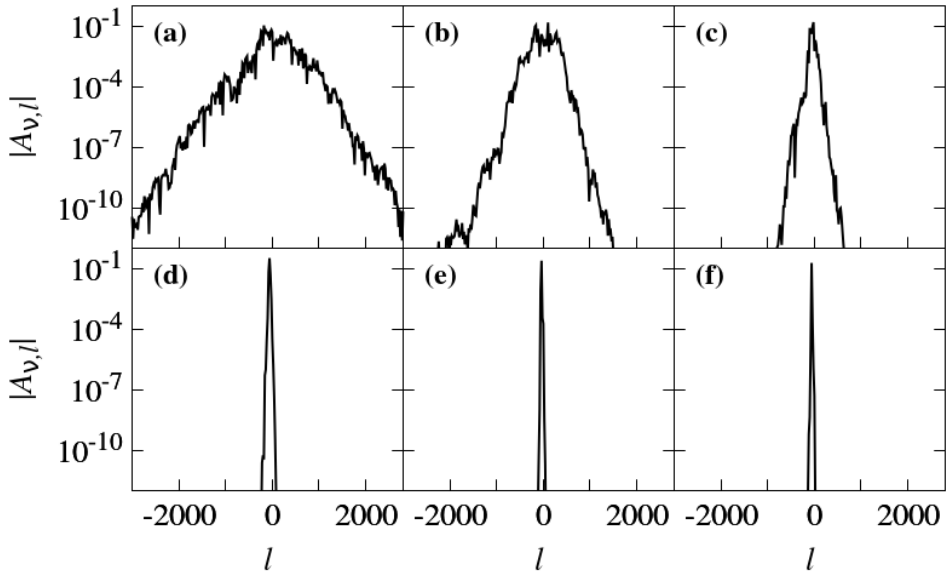

Figure 2.4: The profiles of representative NMs of the LDKG model (2.36), whose mean spatial position l_0 is approximately positioned at the lattice centre and the corresponding normalized square frequencies (2.46) $\omega_{\nu,n}^2 \approx 0.5$ for **(a)** $D = 0.1$, **(b)** $D = 0.15$, **(c)** $D = 0.2$, **(d)** $D = 0.3$, **(e)** $D = 0.4$ and **(f)** $D = 0.5$. The plots are in linear-log scale.

In Figure 2.4 we present the profiles (absolute values of amplitudes $A_{\nu,l}$) of the NMs against the lattice site l, for some centrally positioned (with mean spatial position, l_0, close to the lattice centre) representative modes in linear-log scales for six different values of D, namely, $D = 0.1,\ 0.15,\ 0.2,\ 0.3,\ 0.4,\ 0.5$. The disorder realizations $\tilde{\epsilon}_l \in [1-D, 1+D]$ for the different values of D are the same up to an appropriate scaling. In each panel of Figure 2.4 we plot a NM so that $\omega^2_{\nu,n} \approx 0.5$, a frequency which is approximately centrally placed in the frequency band with a general correspondence to the most extended NMs [Anderson, P. (1958); Kramer et al. (1993); Krimer and Flach (2010)]. All NMs are characterized by clearly defined exponential tails (i.e. NMs are exponentially localized) with a spatial extent which decreases, as D increases, from an order of thousand of sites for $D = 0.1$ [Figure 2.4**(a)**] to a couple of dozen sites for $D = 0.5$ [Figure 2.4**(f)**]. The lattice centre in Figure 2.4 has been shifted to $l = 0$. We note that NMs with square frequencies approximately centrally placed in the frequency band, i.e. $\omega^2_{\nu,n} \approx 0.5$, are not uniquely associated to having their centre l_0 in the middle of the lattice as one may deduce from Figure 2.4.

In Figure 2.5**(a)** we show the normalized NM square frequencies $\omega^2_{\nu,n}$ (2.46) for a representative disorder realization of model (2.36) with $N = 10{,}000$ and parameter $D = 0.1$, as a function of the mean spatial position l_0 of the NMs. The distribution of square frequencies ω^2_ν throughout the lattice is in such a way that they are concentrated at the borders of the spectrum as more data points are located in the regions around $\omega^2_{\nu,n} \approx 0.1$ and $\omega^2_{\nu,n} \approx 0.9$.

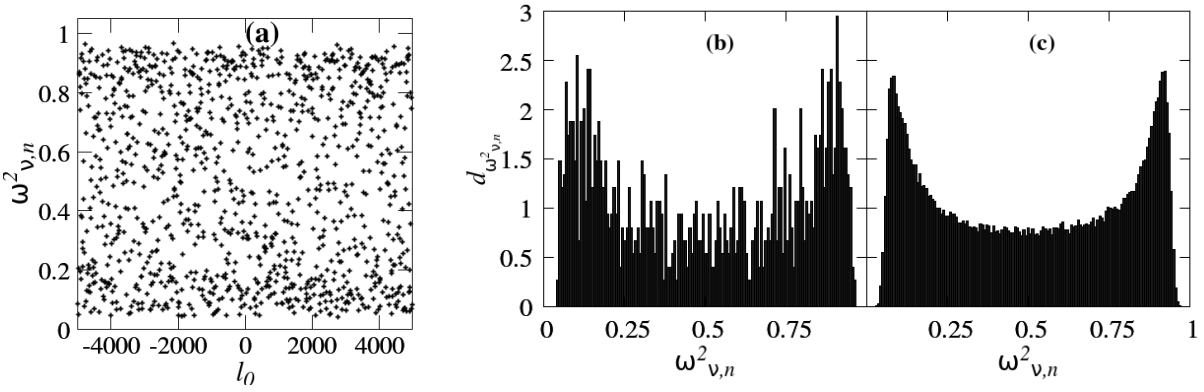

Figure 2.5: Results for the distribution of the square frequencies ω^2_ν of the NMs of system (2.36) with $N = 10{,}000$ and $D = 0.1$: **(a)** the normalized square frequencies $\omega^2_{\nu,n}$ (2.46) of the NMs for a representative disorder realization as a function of the mean spatial position l_0 of the NMs, **(b)** the probability density distribution $d_{\omega^2_{\nu,n}}$ of $\omega^2_{\nu,n}$ for the realization shown in **(a)** and, **(c)** similar to **(b)** but the probability density distribution is computed for for $n_d = 100$ disorder realizations.

This frequency distribution is substantiated in Figure 2.5**(b)** where we present a histogram showing the probability density distribution $d_{\omega^2_{\nu,n}}$ of the square frequencies $\omega^2_{\nu,n}$ of Figure 2.5**(a)**. The maximum values of $d_{\omega^2_{\nu,n}}$ appearing at the edges of the distribution are evidence of the concentration of the square frequencies at the borders of the spectrum. By considering similar findings to the ones of Figure 2.5**(b)** over $n_d = 100$ disorder realizations of parameter $D = 0.1$, we obtain the squared frequency distribution shown in Figure 2.5**(c)** where we have a smoother profile. Here the distribution is seen to have a 'U' shape with peaks of the same distribution value at the two edges. As seen in Figure 2.5**(a)**, where only one disorder realisation is considered, the frequencies avoid the extreme ends $\omega^2_{\nu,n} \approx 0$ and ≈ 1 of the band, something which is also visible in the more general case of Figure 2.5**(c)**. The observation of a 'U' shaped distribution ($d_{\omega^2_{\nu,n}}$) of the

square frequencies ω_ν^2 for $D = 0.1$, as seen in Figure 2.5**(c)**, motivates us to investigate the general dependence of the probability density distribution $d_{\omega^2_{\nu,n}}$ on D. Therefore in Figure 2.6 we show this dependence. We present results for $D = 0.06$ (purple curve), $D = 0.1$ (green curve), $D = 0.2$ (red curve), $D = 0.4$ (black curve) and $D = 0.5$ (orange curve). For lower values of D, the distributions have a 'bowl' shape feature at its centre with peaks at the edges of the distribution. The distribution develops a chapeau-like shape with higher values obtained at plateau edges corresponding to $\omega^2_{\nu,n} \approx 0.2$ and $\omega^2_{\nu,n} \approx 0.8$ for higher values of D ($D = 0.4$ and $D = 0.5$).

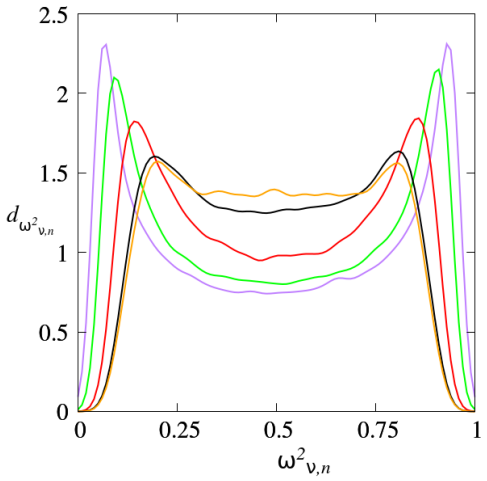

Figure 2.6: Results for the probability density distributions $d_{\omega^2_{\nu,n}}$ of the normalized squared frequencies $\omega^2_{\nu,n}$ (2.46) of system (2.36) for $D = 0.06$ (purple curve), $D = 0.1$ (green curve), $D = 0.2$ (red curve), $D = 0.4$ (black curve) and $D = 0.5$ (orange curve). Every curve is a result of analysing $n_d = 100$ disorder realizations. The plots are in linear-linear scale.

We have seen in Figure 2.4 the spatial extent of NMs decrease as D increases for a representative mode at each value of D that was considered. We now give a generalised estimate of the NM extent using a large number of disorder realisations for various D values.

The extent of NMs can be numerically estimated using a number of different approaches [Kramer et al. (1993); Krimer and Flach (2010)]. For this purpose, we use the localization volume V_ν (2.6) and participation number P_ν (2.5) of the NMs [Krimer and Flach (2010)]. V_ν and P_ν, which are proportional to the average localization length η_ν (2.44), were reported to capture correctly the main features of the NM extent [Kramer et al. (1993); Krimer and Flach (2010)]. We compute V_ν (2.6) and P_ν (2.5) for various values of D and for many disorder realisations in order to get better statistics. In Figure 2.7 we present the localization volume V_ν (2.6), the participation number P_ν (2.5) and the ratio V_ν/P_ν of the NMs of Hamiltonian (2.36) for $D = 0.1$, with respect to the frequency $\omega^2_{\nu,n}$ (2.46). All results are obtained from the analysis of $n_d = 100$ disorder realisations. In creating these plots, we only consider modes with a mean position l_0 located in the central one-third of the lattice in order to avoid any boundary effects. The black curves represent running averages $\langle V \rangle$ [Figure 2.7**(a)**], $\langle P \rangle$ [Figure 2.7**(b)**] and $\langle V/P \rangle$ [Figure 2.7**(c)**] of, respectively, quantities V_ν, P_ν and V_ν/P_ν. We see that the maxima of $\langle V \rangle$ and $\langle P \rangle$ are obtained at the frequency band centre (i.e. $\omega^2_{\nu,n} \approx 0.5$), as expected from equations (2.44) and (2.45). The black continuous curve [Figure 2.7**(c)**] of the ratio $\langle V/P \rangle$, is seen to be independent of $\omega^2_{\nu,n}$ especially in the middle of the frequency band where we find the most extended modes. This shows that, generally the ratio $V_\nu/P_\nu \approx 2.8$ for all NMs except those whose frequencies are at the band edges.

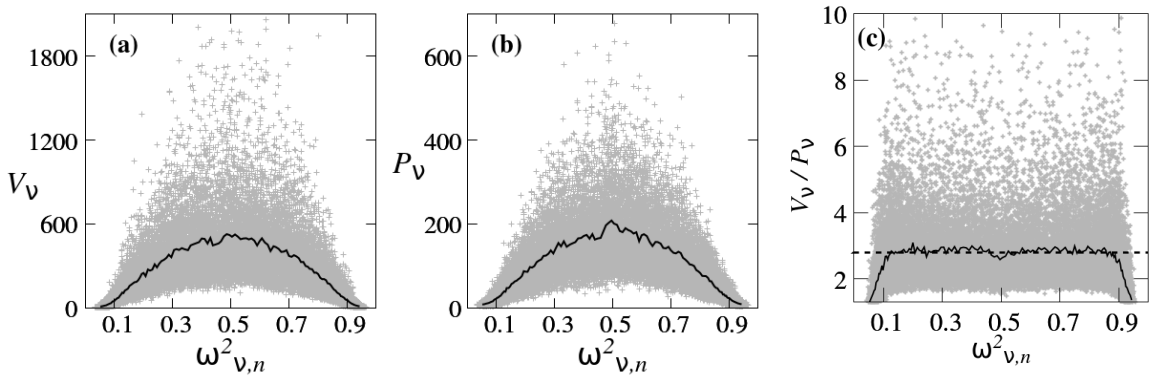

Figure 2.7: Results for **(a)** the localization volume V_ν (2.6), **(b)** the participation number P_ν (2.5), and **(c)** the scaling V_ν/P_ν of the NMs of Hamiltonian model (2.36) for $D = 0.1$ and $n_d = 100$ disorder realizations, as a function of the NMs' normalized square frequency $\omega^2_{\nu,n}$ (2.46). The black curves show running averages of the plotted quantities, i.e. **(a)** $\langle V \rangle$, **(b)** $\langle P \rangle$ and **(c)** $\langle V/P \rangle$. The straight dashed line in **(c)** shows the value $V_\nu/P_\nu = 2.8$. The plots are in linear-linear scale.

We extend the study whose results are shown in Figure 2.7 to other values of D in order to understand their dependence on D.
In Figure 2.8 we show how the dependence of $\langle V \rangle$ on $\omega^2_{\nu,n}$ changes with respect to D for the cases **(a)** $D = 0.06$ (purple curve), $D = 0.08$ (blue curve), $D = 0.1$ (green curve) and **(b)** $D = 0.2$ (red curve), $D = 0.35$ (turquoise curve), $D = 0.5$ (orange curve).

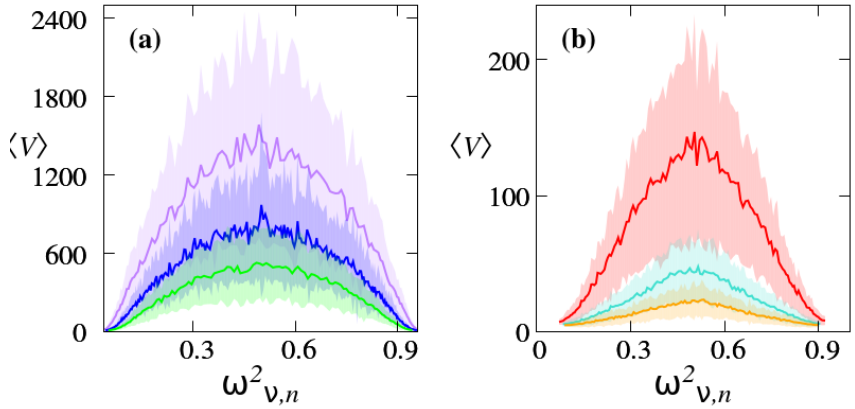

Figure 2.8: Results for the average localization volume $\langle V \rangle$ of NMs located at the central one-third of the lattice of the LDKG system (2.36) as a function of the normalized square frequency $\omega^2_{\nu,n}$ (2.46). **(a)** $D = 0.06$ (purple curve), $D = 0.08$ (blue curve) and $D = 0.1$ (green curve). **(b)** $D = 0.2$ (red curve), $D = 0.35$ (turquoise curve) and $D = 0.5$ (orange curve). The shaded area around each curve indicates 1 standard deviation of V_ν (2.6). The plots are in linear-linear scale.

The shaded area around the $\langle V \rangle$ curve in each case indicates one standard deviation. As in Figure 2.7, we obtain the results of Figure 2.8 only for NMs whose mean positions are located in the middle one-third of the lattice. From the results of Figure 2.8 we observe that both the average value $\langle V \rangle$ and the corresponding standard deviation of the NM localization volume V_ν decrease as D increases.
Next we investigate further the dependence of the average spatial extent of the NMs on the disorder parameter D by restricting our analysis to modes whose square frequencies correspond to the middle one-third of the frequency band (i.e. the more extended modes)

and in addition are also positioned at the lattice's middle one-third. We compute the average participation number $\langle P \rangle$ and localization volume $\langle V \rangle$ for these modes, along with an estimation of the computation errors quantified by one standard deviation, for $n_d = 100$ disorder realizations and present the results in Figure 2.9. We see a decrease of the spatial extent quantities $\langle P \rangle$ and $\langle V \rangle$ when D increases (i.e. as system (2.36) moves from an ordered towards a more disordered lattice).

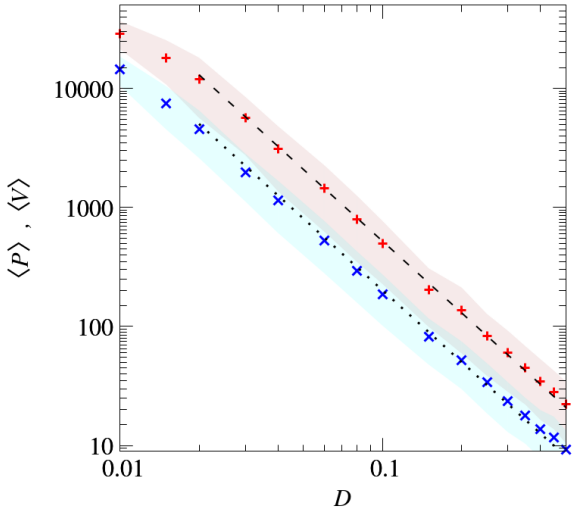

Figure 2.9: Results for the relation between the spatial extent of the NMs and parameter D: The average participation number $\langle P \rangle$ (blue points) and localization volume $\langle V \rangle$ (red points) of the NMs positioned at the central one-third of the lattice and with square frequencies located in the middle one-third of the frequency band, as a function of D, over $n_d = 100$ disorder realizations. The shaded area indicates 1 standard deviation of $\langle V \rangle$ (red shading) and $\langle P \rangle$ (blue shading). The straight lines correspond to the functions $\langle P \rangle = a_p D^{-2}$ (dotted lower line) and $\langle V \rangle = a_v D^{-2}$ (dashed upper line) with $a_p = 2.01$ and $a_v = 5.21$. The plot has logarithmic axes.

Since the localization length η_ν scales as $\propto D^{-2}$ in equations (2.44) and (2.45), we expect $\langle V \rangle$ and $\langle P \rangle$ to have a similar behaviour. We see that this scaling is true from the results of Figure 2.9 since the data $\langle V \rangle$ and $\langle P \rangle$ are respectively well fitted by the functions $a_v D^{-2}$ with $a_v = 5.21 \pm 0.09$ shown by a dashed line and $a_p D^{-2}$ with $a_p = 2.01 \pm 0.05$ shown by a dotted line. In particular, for $D = 0.5$ we have $\langle V \rangle \approx a_v D^{-2} \approx 21$ and $\langle P \rangle \approx a_p D^{-2} \approx 8$, which is in agreement with the findings of Krimer and Flach (2010). The fitting of data shown in Figure 2.9 gives a ratio $\langle V \rangle / \langle P \rangle \approx 2.6$, a value close to 2.8 obtained in Figure 2.7 for $D = 0.1$. In Figure 2.9 we show results for $0.01 \leq D \leq 0.5$, but for obtaining fittings $a_v D^{-2}$ and $a_p D^{-2}$ mentioned above, we only use results for $0.03 \leq D \leq 0.5$. This is because for $D < 0.03$, the NMs are characterized by very large spatial extent which requires a lattice size greater than the maximum size $N = 50{,}000$ which we used for these computations. Using the results of Figure 2.9 and the frequency scale Δ_K (2.43) of the LDKG system we can now define the average NM frequency spacing d as

$$d = \frac{\Delta_K}{\langle V \rangle} \approx \frac{D^2(2D+1)}{5.21}, \tag{2.47}$$

for $\mathcal{W} = 4$, where $\langle V \rangle = 5.21 D^{-2}$ is the fitting shown in Figure 2.9. The quantities Δ_K (2.43) and d (2.47) are key in determining the wave packets' evolution in nonlinear

systems.

As mentioned before for the results of Figure 2.9, lattice size is a restricting factor when numerically investigating NMs and their properties especially when D is very small. We now present a brief discussion for an estimate of the lattice size N which will produce reliable results for the study of NMs. We perform the study as follows:

For a particular value of D (say $D = 0.03$) and a fixed lattice size N (starting with a minimum size $N = 30$), we compute the average localization volume $\langle V \rangle$ of NMs using $n_d = 100$ disorder realizations. We then repeat this computation procedure for an increasing value of N (say $N = 50$, 80, 100, etc.) until when the value of $\langle V \rangle$ becomes independent of N. This will eventually happen when N exceeds a critical value we denote as N_c. In other words, at the lattice size N_c the system has it's maximum possible value of $\langle V \rangle$. We do this for other values of $D > 0.03$. In Figure 2.10**(a)**, we show numerical findings for the dependence of $\langle V \rangle$ on N when different values of $D = 0.01, 0.02, \ldots, 0.5$ are used. The dashed line shows points that correspond to suggested critical values N_c of lattice size below which the computation results must be treated with utmost caution. That is to say, in order to eliminate the interference by lattice boundaries on the study of the NM properties and shapes, a lattice size $N > N_c$ should be used.

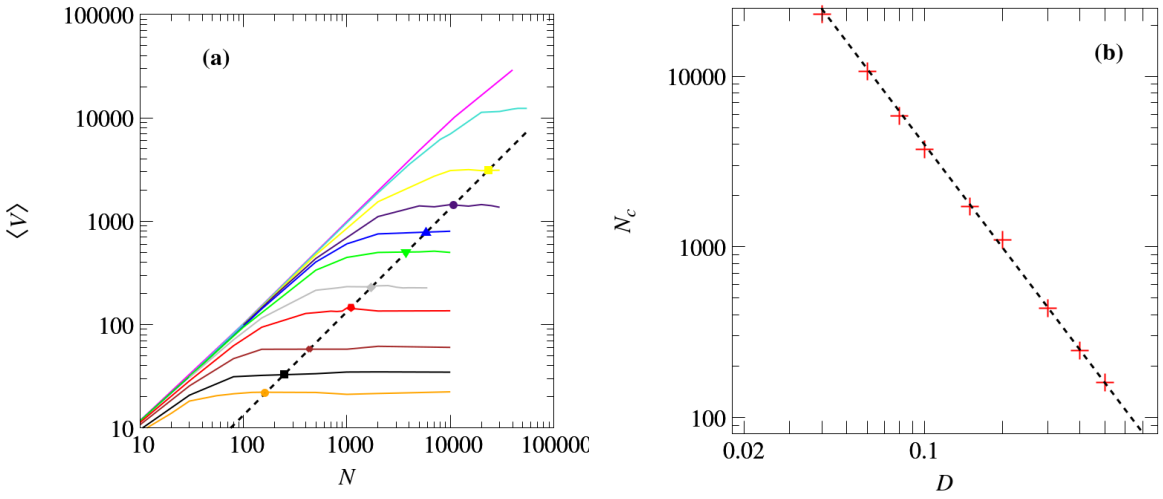

Figure 2.10: Results for lattice size N to use for computing NM extent. **(a)** the dependence of the average NM localization volume $\langle V \rangle$ on lattice size N for different values of $D = 0.01$ (pink curve), 0.02 (turquoise curve), 0.04 (yellow curve), 0.06 (purple curve), 0.08 (blue curve), 0.1 (green curve), 0.15 (gray curve), 0.2 (red curve), 0.3 (brown curve), 0.4 (black curve) and $D = 0.5$ (orange curve). The straight dotted line shows the points corresponding to the critical lattice size values N_c. **(b)** the dependence of N_c on D where the straight line corresponds to the function $N_c = a_N D^{-2}$ with fitting constant $a_N = 40$. The plots have logarithmic axes.

Figure 2.10**(b)** shows the exponential dependence of N_c on D, where it clearly reveals that very large lattice sizes are required for computations involving small values of D. Small values of D would therefore involve computing the eigenvectors and eigenvalues of a matrix $\mathbf{B}$ (2.42), with high order dimensions, and thus an extremely hard computational task. More precisely, the critical lattice size, N_c, depends on D as

$$N_c = a_N D^{-2},$$

where $a_N = 40$. This shows that for the ordered system (when D is zero), one requires an infinite lattice while for $D = 0.01$, a very big size of the order of 100,000 is necessary to compute reliable properties of the NMs.

2.6 Summary

In this chapter we gave a summarised review on properties and behaviour of disordered systems starting with the linear disordered models and discussing the localization of their NMs for both correlated and uncorrelated on-site potentials. We described some nonlinear disordered models with emphasis on two typical models, namely, the DKG and DDNLS systems. Based on the dynamics of the DDNLS model we highlighted the theoretical estimations about the energy spreading mechanisms induced by nonlinearities in disordered lattices. We also mentioned some rather important findings on ordered systems like the FPUT and the Frenkel-Kontorova system as well as the DNA and DKG models. We saw that the NMs of linear disordered systems with sufficiently strong disorder only extend to a finite number of sites and any initially localized wave packet will not spread to an entire lattice of very large size. The introduction of nonlinearities to such models destroys AL as the NMs interact with each other and chaos emerges in the system. The characteristics of the different chaotic dynamical behaviours, namely, the weak, strong and selftrapping regimes were identified. The weak chaos regime is characterised by the wave packet second moment growing subdiffusively following a power law $m_2(t) \propto t^{1/3}$. The strong chaos regime on the other hand has a faster subdiffusion as $m_2(t) \propto t^{1/2}$ which gradually slows down to the weak chaos spreading rate. The appearance of these various dynamical regimes is dependant on the properties of systems' NMs, namely, the frequency band width Δ, the NM localization volume V, the average spacing $d \approx \Delta/V$ of the modes and the nonlinearity dependent frequency shift due to the energy. In addition, we introduced and studied the qualitative and statistical NM properties for a modified 1D disordered DKG model (2.36), whose disorder strength depends on two parameters, namely, D which defines the interval from which the disorder values are chosen and $\mathcal{W}$ which regulates the size of nearest-neighbour interactions. For a fixed $\mathcal{W} = 4$, we investigated the qualitative structural changes in the NMs as the model becomes disordered by letting D approach 0.5 from 0. The NMs become more spatially localized in the lattice and the number of the NMs' squared frequencies become less clustered on the ends of the frequency band losing an initial 'U' shape to a 'plateau'-like distribution when D increases. Analysing further the model, we computed the NM localization volume V_ν (2.6) and participation number P_ν (2.5) for different values of D in the interval $0 < D \leq 0.5$. The corresponding average values, over 100 disorder realizations, $\langle V \rangle$ and $\langle P \rangle$ are respectively governed by the laws $\langle P \rangle \propto D^{-2}$ and $\langle V \rangle \propto D^{-2}$. A correction scaling to cater for the fluctuations and thus underestimate of $\langle P \rangle$ is given by $\langle V \rangle \approx 2.6\langle P \rangle$. The control of the on-site potentials by the two parameters D and $\mathcal{W}$ provides more flexibility in ways of working with the system, as the impact of heterogeneity in the model can either be altered through adjusting the sample set of on-site potentials (by modifying the values of D) or the strength of the nearest-neighbour interactions (by changing the values of $\mathcal{W}$). The presence of these two parameters therefore enables the investigations on the effect of different physical processes on the system's dynamics theoretically, numerically and experimentally. This analysis constitutes a first step towards an in-depth study of the dependence of the DKG system's dynamics on the disorder when D is changed.

Chapter 3

Numerical techniques

In this chapter we present the main numerical techniques we use to answer the research questions of our study as stated in Chapter 1. Parts of the findings in this chapter have been reported in Senyange and Skokos (2018). The Chapter is presented as followings: In Section 3.1 we discuss the concepts of deviation vectors, the corresponding deviation vector distribution (DVD) and variational equations, which are then followed by a concise theoretical review on Lyapunov characteristic exponents (LCEs) in Section 3.2. We then provide a detailed theoretical description of various numerical integration techniques in Section 3.3, mainly focussing on the class known as symplectic integrators (SIs). There we give a description of some already existing SIs which have been previously used to integrate Hamiltonian systems (e.g. in solar system and particle accelerator dynamics) and we also construct some new SIs using composition techniques. We then implement in Section 3.4, the methods discussed in Section 3.3 to compare the computational efficiency of many different integrators in following the dynamical evolution of Hamiltonian systems. Finally in Section 3.5 we discuss and summarize our findings.

3.1 Deviation vectors

A variety of techniques used to study dynamical systems involve the consideration of the relative position (or positions) of a pair (or pairs) of points in their respective time-trajectories in a phase space. An infinitesimal perturbation vector which describes the relative position of two phase space points is called a *deviation vector*. For any pair of points $\mathbf{y} = (y_1, y_2, y_3, \cdots, y_N, p_{y_1}, p_{y_2}, \cdots, p_{y_N})$ and $\mathbf{x} = (x_1, x_2, x_3, \cdots, x_N, p_{x_1}, p_{x_2}, \cdots, p_{x_N})$ in a $2N$-D phase space, the deviation of $\mathbf{y}$ from $\mathbf{x}$ is the vector $\mathbf{w} = \mathbf{y} - \mathbf{x}$ where

$$\mathbf{w} = (w_{\mathbf{r1}}, w_{\mathbf{r2}}, \cdots, w_{\mathbf{r2N}}) = (\delta q_{\mathbf{r1}}, \delta q_{\mathbf{r2}}, \cdots, \delta q_{\mathbf{rN}}, \delta p_{\mathbf{r1}}, \delta p_{\mathbf{r2}}, \cdots, \delta p_{\mathbf{rN}}) \tag{3.1}$$

with **ri** denoting the n-tuple spatial-dimension index ranked in position **i**. That is to say, the indexing for an N oscillator 1D Hamiltonian model is such that $\mathbf{r1} = 1$ and $\mathbf{rN} = N$, while for a $N = KM$ oscillator 2D Hamiltonian model (array of K oscillators along one direction and M along a perpendicular direction), $\mathbf{r1} = (1, 1)$ and $\mathbf{rN} = (K, M)$. More particularly, $\delta q_{\mathbf{ri}} = y_i - x_i = w_{\mathbf{ri}}$ for $i \leq N$ and $\delta p_{\mathbf{ri}} = p_{y_i} - p_{x_i} = w_{\mathbf{ri}}$ for $i > N$. We use Equation (3.1) of a deviation vector to define a normalized distribution, the DVD.

3.1.1 Deviation vector distribution (DVD)

In order to study extensively the chaotic behaviour of the DKG systems (2.19) and (2.22), we monitor the evolution of time dependent normalized DVD $\{\xi^D_{\mathbf{r}}\}_{\mathbf{r}\in\mathbb{N}^n}$ of the system, for

a lattice of n spatial dimensions.

$$\xi^D_{\mathbf{r}} = \frac{\delta q^2_{\mathbf{r}} + \delta p^2_{\mathbf{r}}}{\sum_{\mathbf{k}} \delta q^2_{\mathbf{k}} + \delta p^2_{\mathbf{k}}}, \tag{3.2}$$

where $\mathbf{k}$ and $\mathbf{r}$ are n-tuples whose components are positive integers.
Through the DVD we monitor the position of the degrees of freedom where the chaotic dynamics is concentrated (chaotic hotspots) [Skokos et al. (2013)] as time evolves. We also use the deviation vector for the computation of the LCEs [Lyapunov (1992); Oseledec (1968); Benettin et al. (1976); Pesin (1977); Skokos (2010)]. LCEs, which we describe in later in Section 3.2, are a measure at relatively large times. Due to computational limitations, we are unable to compute the LCEs for very long times. We therefore seek deviation vectors that will give as much information about the exponents as possible in the shortest time possible. For the DVD (3.2), we define the associated second moment m^D_2 and participation number P^D as follows:
The participation number P^D of the DVD (3.2),

$$P^D = \frac{1}{\sum_{\mathbf{r}} {\xi^D_{\mathbf{r}}}^2}, \tag{3.3}$$

where $\mathbf{r}$ is a spatial dimension dependent index, estimates the number of lattice sites with the strongest deviation. The second moment m^D_2 of the DVD (3.2) which quantifies the spatial extent of spreading of the distribution is given by

$$m^D_2 = \sum_{\mathbf{r}} ||\mathbf{r} - \bar{\mathbf{r}}||^2 \xi^D_{\mathbf{r}} \tag{3.4}$$

where $\bar{\mathbf{r}} = \sum_{\mathbf{r}} \mathbf{r}\xi^D_{\mathbf{r}}$ is the centre of the distribution $\{\xi^D_{\mathbf{r}}\}_{\mathbf{r}}$ and $||\cdot||$ denotes the Euclidean norm.

3.1.2 Equations of motion and variational equations

Let $H(\mathbf{q}, \mathbf{p})$ be a Hamiltonian function of a time independent model with N degrees of freedom. For generalised position vector $\mathbf{q}$ and conjugate momenta vector $\mathbf{p}$, the system configuration in the $2N-D$ phase space is described by the point $\mathbf{z}(t) = (\mathbf{q}(t), \mathbf{p}(t))$. The resulting equations of motion

$$\frac{d\mathbf{p}}{dt} = -\frac{\partial H}{\partial \mathbf{q}}, \qquad \frac{d\mathbf{q}}{dt} = \frac{\partial H}{\partial \mathbf{p}} \tag{3.5}$$

can be written using matrices as $\frac{d\mathbf{z}}{dt} = J_{2N} D$, where D is the transpose of $\begin{pmatrix} \frac{\partial H}{\partial \mathbf{q}} & \frac{\partial H}{\partial \mathbf{p}} \end{pmatrix}$. J_{2N} is a matrix of the form

$$J_{2N} = \begin{pmatrix} \mathbf{0}_N & \mathbf{I}_N \\ -\mathbf{I}_N & \mathbf{0}_N \end{pmatrix}$$

with $N \times N$ identity matrix $\mathbf{I}_N$ and $N \times N$ zero matrix $\mathbf{0}_N$.
A deviation vector stationed at the point $\mathbf{z}(t)$ evolves in the tangent space following the so called *variational equations* [see e.g. Skokos and Gerlach (2010); Gerlach and Skokos (2011); Gerlach et al. (2012)]

$$\frac{d\mathbf{w}(t)}{dt} = A(t)\mathbf{w}(t), \tag{3.6}$$

where $\mathbf{w} = (\delta q_{\mathbf{r1}}, \delta q_{\mathbf{r2}}, \cdots, \delta q_{\mathbf{rN}}, \delta p_{\mathbf{r1}}, \delta p_{\mathbf{r2}}, \cdots, \delta p_{\mathbf{rN}})$ denotes the deviation vector (3.1) of small perturbations, $A(t) = J_{2N} D^2(\mathbf{z}(t))$ and $D^2(\mathbf{z}(t)) = \left[\frac{\partial^2 H(\mathbf{z})}{\partial q_{\mathbf{j}} \partial q_{\mathbf{k}}}\right]$ is the Hessian matrix of

the Hamiltonian calculated at $\mathbf{z}(t)$. The differential equations (3.6) are linear with respect to $\mathbf{w}$ with coefficients which are elements of matrix $A(t)$.
Let us now compute the variational equations for an autonomous Hamiltonian $H(\mathbf{z})$ which can be split in two parts as

$$H(\mathbf{z}) = T(\mathbf{p}) + V(\mathbf{q}) \tag{3.7}$$

where $H(\mathbf{q}, \mathbf{p})$ is the energy, V is the potential energy and $T = \sum_{\mathbf{r}} \frac{p_{\mathbf{r}}^2}{2}$ is the kinetic energy. The corresponding equations of motion (3.5) are

$$\frac{d\mathbf{q}}{dt} = \mathbf{p}, \qquad \frac{d\mathbf{p}}{dt} = -\frac{\partial V(\mathbf{q})}{\partial \mathbf{q}} \tag{3.8}$$

and the variational equations (3.6) become

$$\frac{d}{dt}\mathbf{w}(t) = \begin{pmatrix} \frac{d}{dt}(\delta\mathbf{q}_{\mathbf{r}}) \\ \\ \frac{d}{dt}(\delta\mathbf{p}_{\mathbf{r}}) \end{pmatrix} = \begin{pmatrix} \mathbf{0}_N & \mathbf{I}_N \\ \\ -D_V^2(\mathbf{q}(t)) & \mathbf{0}_N \end{pmatrix} \begin{pmatrix} \delta\mathbf{q}_{\mathbf{r}} \\ \\ \delta\mathbf{p}_{\mathbf{r}} \end{pmatrix}, \tag{3.9}$$

where the element with indices $\mathbf{j}, \mathbf{k}$ of sub matrix $D_V^2(\mathbf{q}(t))$ is $D_V^2(\mathbf{q}(t))_{\mathbf{j},\mathbf{k}} = \frac{\partial^2 V(\mathbf{q})}{\partial q_{\mathbf{j}} \partial q_{\mathbf{k}}}$. Equivalently, Equation (3.9) can be written as

$$\frac{d}{dt}(\delta\mathbf{q}_{\mathbf{r}}) = \delta\mathbf{p}_{\mathbf{r}}; \qquad \frac{d}{dt}(\delta\mathbf{p}_{\mathbf{r}}) = -D_V^2(\mathbf{q}(t))\delta\mathbf{q}_{\mathbf{r}}.$$

We use the *tangent map method* (TM) technique [Skokos and Gerlach (2010); Gerlach and Skokos (2011); Gerlach et al. (2012)] to integrate the variational equations (3.9). The dynamics on the tangent space for the Hamiltonian (3.7) is defined by the non autonomous Hamiltonian function

$$H_{\mathcal{V}}(\delta\mathbf{q}, \delta\mathbf{p}, t) = \frac{1}{2}\sum_{\mathbf{i}} \delta p_{\mathbf{i}}{}^2 + \frac{1}{2}\sum_{\mathbf{j},\mathbf{k}} D_V^2(\mathbf{q}(t))_{\mathbf{j},\mathbf{k}}\delta q_{\mathbf{j}}\delta q_{\mathbf{k}}, \tag{3.10}$$

called the *tangent dynamics Hamiltonian* (TDH). The equations of motion for the TDH (3.10) are the variational equations (3.9). We integrate equations (3.9) along with the equations of motion (3.8) since the variational equations depend on the position $\mathbf{q}$.

3.2 Lyapunov characteristic exponents (LCEs)

LCEs are asymptotic measures which are used to characterise the average growth of small perturbations to the solutions of a dynamical system. Lyapunov [Lyapunov (1992)] introduced the concept of LCEs in 1892 when analysing the stability of non-stationary solutions of ordinary differential equations. Since then, LCEs have been widely used by researchers in studying dynamical behaviour in various systems. A detailed survey of the theoretical and application aspects of this topic is presented and can be found in Skokos (2010).
The theory of LCEs was applied to characterise chaotic orbits by Oseledec (1968), and the connection between LCEs and exponential divergence of nearby orbits was given in Benettin et al. (1976) and Pesin (1977). For a chaotic orbit, at least one LCE is positive, implying exponential divergence of nearby orbits, while in the case of regular orbits all LCEs are zero or negative. Therefore, since the presence of a positive exponent guarantees chaoticity of an orbit, the computation of the *maximum Lyapunov Characteristic Exponent* (mLCE) λ suffices for purposes of determining the chaotic nature of the orbit.

The mLCE is computed as the limit for $t \to \infty$ of the quantity

$$\Lambda(t) = \frac{1}{t} \ln \frac{\|\mathbf{w}(t)\|}{\|\mathbf{w}(0)\|}, \tag{3.11}$$

often called the finite time mLCE, where $\mathbf{w}(0)$ and $\mathbf{w}(t)$ are deviation vectors from a given orbit at times $t = 0$ and $t > 0$, respectively. As usual $\|.\|$ denotes the norm of a vector. So, we have

$$\lambda = \lim_{t\to\infty} \Lambda(t). \tag{3.12}$$

The existence of this limit is guaranteed by the Multiplicative Ergodic Theorem [Oseledec (1968); Benettin et al. (1980a,b); Skokos et al. (2016)]. $\Lambda(t)$ tends to zero in the case of regular orbits following a power law [Benettin et al. (1976)],

$$\Lambda(t) \propto t^{-1},$$

while it tends to non-zero values in the case of chaotic orbits.
A Hamiltonian of N degrees of freedom has at most $2N$ different LCEs, which are ordered as $\lambda = \lambda_1 \geq \lambda_2 \geq \ldots \geq \lambda_{2N}$. In Benettin et al. (1978) a theorem was formulated, which led directly to the development of a numerical technique for the computation of all LCEs. This technique which is based on the time evolution of multiple deviation vectors keeps them linearly independent by the Gram-Schmidt orthonormalization procedure. The theoretical framework, as well as the corresponding numerical method for the computation of all LCEs (usually called the standard method), was given in Benettin et al. (1980a,b). According to this method all LCEs λ_2, λ_3, etc. are computed respectively as the limit for $t \to \infty$ of some appropriate finite-time dependent quantities Λ_2, Λ_3, etc [Benettin et al. (1980b); Skokos and Gerlach (2010)]. It has been shown in Benettin et al. (1980a) that for an autonomous Hamiltonian flow, the LCEs are such that,

$$\lambda_i = -\lambda_k, \text{ for } i = 1, 2, \cdots, N \text{ and } i + k = 2N + 1.$$

In addition, since the Hamiltonian function is an integral of motion, at least two LCEs vanish, i.e.,

$$\lambda_N = -\lambda_{N+1} = 0,$$

while the presence of any additional independent integral of motion leads to the vanishing of another pair of the LCEs.

3.3 Numerical Integration

Ordinary differential equations can be integrated using various numerical integration techniques. Unfortunately, some integration techniques fail to preserve important structural properties that define the systems of differential equations, for example Hamiltonian system conservation properties. However, SIs conserve the integrals of motion in Hamiltonian systems for long times and so are a preference for the integration of these systems. Starting with the work of Wisdom and Holman (1991), SIs have been widely used for long-term integrations of the solar system. In such studies, for example McLachlan (1995) and Morbidelli (2002), low order schemes were constructed and used for solving Hamiltonian systems. For our work, we need schemes that are computationally fast and efficient thereby enabling us to perform a long term analysis of the dynamics of the studied systems.

3.3.1 Symplectic integrators (SIs)

We now discuss in more detail the theory of SIs, mention some efficient schemes that have been previously used and recommended, describe composition techniques for the construction of new schemes and define some new SIs.
Let $f(\mathbf{q},\mathbf{p})$ and $g(\mathbf{q},\mathbf{p})$ be real valued differentiable functions of $\mathbf{q}$ and $\mathbf{p}$ defined on $\mathbb{R}^{2m}$ for some positive integer m. Then, the *Poisson bracket* $\{\cdot,\cdot\}$ of $f(\mathbf{q},\mathbf{p})$ and $g(\mathbf{q},\mathbf{p})$ is defined as

$$\{f,g\} = \sum_{i=1}^{m} \left(\frac{\partial f}{\partial q_i}\frac{\partial g}{\partial p_i} - \frac{\partial f}{\partial p_i}\frac{\partial g}{\partial q_i} \right).$$

For a point $\mathbf{z} = (\mathbf{q},\mathbf{p})$ on the Hamiltonian surface defined by $H(\mathbf{q},\mathbf{p})$, we can write the Hamilton equations of motion (3.5) in the form

$$\frac{d\mathbf{z}}{dt} = \{\mathbf{z}, H(\mathbf{z})\} =: L_H\mathbf{z}, \tag{3.13}$$

where L_H is a differential operator. For an initial condition $\mathbf{z}(t)$, the formal solution of Equation (3.13) is

$$\mathbf{z}(t+\tau) = \sum_{i\geq 0} \frac{\tau^i}{i!} L_H^i \mathbf{z}(t) = e^{\tau L_H}\mathbf{z}(t). \tag{3.14}$$

If the Hamiltonian function $H(\mathbf{q},\mathbf{p})$ can be split into two integrable parts like for example $T = T(\mathbf{p})$ and $V = V(\mathbf{q})$, namely $H = T + V$ (for example in Equation (3.7)), then the action of the operators $e^{\tau L_T}$ and $e^{\tau L_V}$ (obtained by splitting $H(\mathbf{q},\mathbf{p})$) is explicitly known through finding the analytic solution of the differential equations (3.5). An explicit SI of order k (where $k \in \mathbb{N}$) approximates the action of operator $e^{\tau L_H}$ by a series of products of operators $e^{a_i\tau L_V}$ and $e^{b_i\tau L_T}$ for $i \in \{1,2,3\cdots,j\}$ for some integer $j \geq 1$, a_i, b_i being coefficients that are determined so as to minimize the error in the approximation. The Baker-Campbell-Hausdorff (BCH) relation enables us to find order conditions which coefficients a_i, b_i satisfy for high order schemes [Koseleff (1993), Koseleff (1996)].
The energy components $T(\mathbf{p})$ and $V(\mathbf{q})$ can be considered as Hamiltonians and so the operators $e^{\tau L_V}$ and $e^{\tau L_T}$ are symplectic maps which are acting on the phase space point $\mathbf{z}$. This therefore means that the operator $e^{\tau L_H}$ is approximated by a symplectic map which is the product composition of $e^{a_i\tau L_V}$ and $e^{b_i\tau L_T}$. That is to say

$$e^{\tau L_H} = e^{\tau(L_V+L_T)} = \prod_{i=1}^{j} e^{a_i\tau L_V} e^{b_i\tau L_T} + \mathcal{O}(\tau^{n+1}),$$

where the positive integer n corresponds to the order of the integrator; and the number ($\leq 2j$) of appearances of $e^{a_i\tau L_V}$ and $e^{b_i\tau L_T}$ in the product approximation of $e^{\tau L_H}$ is called the number of steps of the SI. In the next Sections we study various SIs that have been developed and used by different researchers, as well as some new SIs we construct through composition techniques.

SIs of order one

If a Hamiltonian $H(\mathbf{q},\mathbf{p})$ is analytically integrable (e.g for linear systems), then without having to split H into it's potential and kinetic components, we can construct the simplest single step SI S_1 as $S_1 = e^{\tau L_H}$ whose application in solving the Hamiltonian equations gives no error in the energy. For non integrable Hamiltonians however, we think of SIs that make use of the part splitting techniques. A simple such first order SI is the two step symplectic Euler method [Hairer et al. (2001)] defined as

$$E(\tau) = e^{\tau L_V} e^{\tau L_T}.$$

Unfortunately, SIs of order one have a limited application in solving general Hamiltonian systems because of their very low accuracy in preserving the energy $H(\mathbf{q},\mathbf{p})$ of the system. That is to say, the approximation of the solution in Equation (3.14) leaves a relatively large error term especially when a large time step τ is used. A small time step reduces the error in computation but greatly increases the time required to complete the integration. We therefore focus more on schemes of order greater than one.

SIs of order two

A splitting of the Hamiltonian to have the position and momentum operators $e^{\tau L_V}$ and $e^{\tau L_T}$ respectively contribute one and two integration steps gives a three step SI:

$$LF(\tau) = e^{a\tau L_T} e^{b\tau L_V} e^{a\tau L_T}. \tag{3.15}$$

This integrator, which has been referred to as the Leap frog or Störmer/Verlet [Ruth and Berkeley (1983), Hairer et al. (2001)], has positive coefficients $a = \frac{1}{2}$ and $b = 1$. This is one of the simplest splitting we can have for the integration operators $e^{\tau L_V}$ and $e^{\tau L_T}$ as other possible splittings will either generate the same number of steps or more than three steps. A second class of integrators with order $n \geq 2$ that has been frequently used to integrate Hamiltonian systems and symplectic maps is the $SABA$ and $SBAB$ schemes [Laskar and Robutel (2001)] in which only positive integration steps are used. These integrators are in general used to integrate Hamiltonian systems of the form $H = T + \epsilon V$ for T and V integrable and ϵ a small perturbation parameter. Second order SIs $SABA_1$ and $SBAB_1$ of 3 steps, are identical to the Leap frog integrator LF (3.15). That is to say,

$$SABA_1 = e^{\frac{1}{2}\tau L_T} e^{\tau L_V} e^{\frac{1}{2}\tau L_T} \text{ and } SBAB_1 = e^{\frac{1}{2}\tau L_V} e^{\tau L_T} e^{\frac{1}{2}\tau L_V}.$$

Other second order SIs are the $SABA_2$ and $SBAB_2$ (under SI classes $SABA$ and $SBAB$ respectively) [Laskar and Robutel (2001)] and have the forms

$$SABA_2(\tau) = e^{a_1\tau L_T} e^{b\tau L_V} e^{a_2\tau L_T} e^{b\tau L_V} e^{a_1\tau L_T}, \tag{3.16}$$

with $a_1 = \frac{1}{2} - \frac{1}{2\sqrt{3}}$, $a_2 = 1 - 2a_1$, $b = \frac{1}{2}$, and

$$SBAB_2(\tau) = e^{b_1\tau L_V} e^{a\tau L_T} e^{b_2\tau L_V} e^{a\tau L_T} e^{b_1\tau L_V}, \tag{3.17}$$

for $a = \frac{1}{2}$, $b_1 = \frac{1}{6}$ and $b_2 = 1 - 2b_1$. Each one of these schemes has 5 steps and an error of the order $\mathcal{O}(\tau^4 + \tau^2)$ for an integration time step τ.
A second order integrator with 9 steps, $ABA82$ was studied in McLachlan (1995) and Farrés et al. (2013), namely

$$ABA82(\tau) = e^{a_1\tau L_T} e^{b_1\tau L_V} e^{a_2\tau L_T} e^{b_2\tau L_V} e^{a_3\tau L_T} e^{b_2\tau L_V} e^{a_2\tau L_T} e^{b_1\tau L_V} e^{a_1\tau L_T}, \tag{3.18}$$

where the coefficients a_k, b_k, $k = 1, 2, 3$ are specified in Farrés et al. (2013). We note that the SI $ABA82$ has been referred to as $SABA_4$ in Laskar and Robutel (2001).

SIs of order four

The order two SIs $SABA_2$ (3.16) and $SBAB_2$ (3.17) can be made more accurate by increasing their order and thereby reducing the error magnitude for their computations if the Poisson bracket $\{V, \{V, T\}\}$ leads to an integrable Hamiltonian [Laskar and Robutel (2001)]. The systems considered in this work are such that T is quadratic in momenta $\mathbf{p}$ and independent of $\mathbf{q}$ while V only depends on the positions $\mathbf{q}$. Therefore $\{V, \{V, T\}\}$

is integrable since it only depends on $\mathbf{q}$. Thus, the accuracy of (3.16) and (3.17) can be improved by the application of a corrector term

$$C(\tau) = e^{-\tau^3 \frac{c}{2} L_{\{V,\{V,T\}\}}} \tag{3.19}$$

before and after the application of the main body of these integrators, where $c = \frac{(2-\sqrt{3})}{24}$ for $SABA_2$ and $c = \frac{1}{72}$ for $SBAB_2$. The subsequent application of (3.19) gives two SIs, each with seven steps and error of order $\mathcal{O}(\tau^4)$, which we name $SABA_2C$ for $SABA_2$ and $SBAB_2C$ for $SBAB_2$. That is to say,

$$SABA_2C = e^{-\tau^3 \frac{c}{2} L_{\{V,\{V,T\}\}}} e^{a_1 \tau L_T} e^{b\tau L_V} e^{a_2 \tau L_T} e^{b\tau L_V} e^{a_1 \tau L_T} e^{-\tau^3 \frac{c}{2} L_{\{V,\{V,T\}\}}}$$

and

$$SBAB_2C = e^{-\tau^3 \frac{c}{2} L_{\{V,\{V,T\}\}}} e^{b_1 \tau L_V} e^{a\tau L_T} e^{b_2 \tau L_V} e^{a\tau L_T} e^{b_1 \tau L_V} e^{-\tau^3 \frac{c}{2} L_{\{V,\{V,T\}\}}}$$

with coefficients a_i, b and a, b_i respectively corresponding to the ones of Equations (3.16) and (3.17). We note that SIs in the classes $SABA$ and $SBAB$ of order greater than two, were constructed and tested in Laskar and Robutel (2001). For small time steps, the SI $LF(\tau)$ gave the highest error in the energy compared to all the other SIs which all gave practically the same energy error. For each of the SIs investigated, the energy error was found to grow linearly with the increase in time step for moderate time steps. This linearity was found to be lost in almost all higher order SIs for larger time steps with $LF(\tau)$ giving the smallest error in energy for very large time steps. The SIs $SABA_2C$ and $SBAB_2C$, which require additional computations for the corrector terms $C(\tau)$ (3.19), have been reported to be more efficient compared to other schemes of order less or equal to four except for cases where very high accuracy is desired and the time step used is small.

A second class of fourth order SIs we consider for our study was presented in Farrés et al. (2013) and also in Blanes et al. (2013) as SIs of generalised order. We consider the relatively efficient SIs $ABA864$ of 15 steps and $ABAH864$ of 17 steps. A detailed description of these integration methods and the values of the coefficients a_i, b_i can be found in Blanes et al. (2013).

In Yoshida (1990), a method to construct SIs of higher order by successively applying lower order schemes is proposed. According to that approach, we can construct a SI $S_{2n+2}(\tau)$ of even order $2n+2$ by applying SI $S_{2n}(\tau)$ of even order $2n$ in the following way:

$$S_{2n+2}(\tau) = S_{2n}(d\tau) S_{2n}(\tau - 2d\tau) S_{2n}(d\tau), \tag{3.20}$$

with coefficient

$$d = \frac{-2^{\frac{1}{2n+1}}}{2 - 2^{\frac{1}{2n+1}}}.$$

This means that we have to successively apply 3 times the SI S_{2n} when generating the scheme S_{2n+2}. Hence, a successive application of S_2, 3^n times, with the appropriate coefficients gives the SI S_{2n+2}. In this way the number of steps of the scheme S_{2n+2} grows rapidly when n increases, even when the compositions can be optimised by grouping together similar adjacent elementary operators for example combining $e^{a_i \tau L_V}$ with $e^{b_i \tau L_V}$ in the two step operator $e^{a_i \tau L_V} e^{b_i \tau L_V}$ to get a one step operator $e^{(a_i+b_i)\tau L_V}$ (or $e^{a_i \tau L_T}$ with $e^{b_i \tau L_T}$ in $e^{a_i \tau L_T} e^{b_i \tau L_T}$ to get $e^{(a_i+b_i)\tau L_T}$).

Using the composition technique (3.20), we now demonstrate how to construct several SIs of order four by using order two schemes. In Forest and Ruth (1990) and Yoshida (1990) a fourth order SI of 7 steps was constructed using the SI LF (3.15). This scheme, which we refer to as FR_4 is defined by

$$FR_4(\tau) = e^{a_1 \tau L_T} e^{b_1 \tau L_V} e^{a_2 \tau L_T} e^{b_2 \tau L_V} e^{a_2 \tau L_T} e^{b_1 \tau L_V} e^{a_1 \tau L_T},$$

with

$$a_1 = \frac{1}{2\,(2-2^{1/3})},\quad a_2 = \frac{1-2a_1}{2},\quad b_1 = \frac{1}{2-2^{1/3}},\quad b_2 = 1-2b_1.$$

We note that FR_4 corresponds to $SABA_3$ or $SBAB_3$ under, respectively, the class of $SABA$ and $SBAB$ [Laskar and Robutel (2001)] SIs.
In a similar way we also construct fourth order schemes $SABA_2Y_4$, $SBAB_2Y_4$ and $ABA82Y_4$ (of steps 13, 13 and 25 respectively) by applying the composition method (3.20) to respectively the SIs $SABA_2$ (3.16), $SBAB_2$ (3.17) and $ABA82$ (3.18) of order two.

SIs of order six

The composition technique (3.20) allows us to construct SIs of order six from integrators of order four. In particular, we use $FR4$, $SABA_2Y_4$, $SBAB_2Y_4$, $ABA82Y_4$, $SABA_2C$ and $ABA864$ to create respectively $FR4Y_6$, $SABA_2Y_4Y_6$, $SBAB_2Y_4Y_6$, $ABA82Y_4Y_6$, $SABA_2CY_6$ and $ABA864Y_6$. The new schemes $FR4Y_6$, $SABA_2Y_4Y_6$, $SBAB_2Y_4Y_6$, $ABA82Y_4Y_6$, $SABA_2CY_6$ and $ABA864Y_6$ respectively have 19, 37, 37, 73, 19 and 43 steps.
Besides the composition technique (3.20), another composition method for constructing an order six SI S_6 from an order two SI S_2 was presented in Yoshida (1990). This scheme requires fewer steps than a sixth order SI generated from an order two SI by equation (3.20) and is of the form

$$S_6(\tau) = S_2(w_3\tau)S_2(w_2\tau)S_2(w_1\tau)S_2(w_0\tau)S_2(w_1\tau)S_2(w_2\tau)S_2(w_3\tau), \tag{3.21}$$

where the coefficients w_i are specified in Yoshida (1990). According to McLachlan (1995) the set of coefficients in Yoshida (1990) that corresponds to what is referred to as *solution A* lead to the most numerically efficient composition schemes of the form (3.21). We note that in Kahan and Li (1997) the composition method with *solution A* has been named $s7odr6$. We construct more SIs of order six by applying this composition method to some integrators of order two. From $SABA_2$ (3.16), $SBAB_2$ (3.17) and $ABA82$ (3.18), we respectively obtain $SABA_2Y_6$ and $SBAB_2Y_6$ with 29 steps each and $ABA82Y_6$ with 57 steps.
We also consider order six integration schemes $s11odr6$ of Sofroniou and Spaletta (2005) and, $s9odr6b$ of Kahan and Li (1997) which respectively are based on 11 and 9 successive applications of $S_2(\tau)$. That is to say,

$$s11odr6(\tau) = S_2(\gamma_1\tau)S_2(\gamma_2\tau)\cdots S_2(\gamma_5\tau)S_2(\gamma_6\tau)S_2(\gamma_5\tau)\cdots S_2(\gamma_2\tau)S_2(\gamma_1\tau). \tag{3.22}$$

$$s9odr6b(\tau) = S_2(\delta_1\tau)S_2(\delta_2\tau)S_2(\delta_3\tau)S_2(\delta_4\tau)S_2(\delta_5\tau)S_2(\delta_4\tau)S_2(\delta_3\tau)S_2(\delta_2\tau)S_2(\delta_1\tau), \tag{3.23}$$

where the values of γ_i, $i = 1,\ldots,6$ and δ_i, $i = 1,\ldots,5$ are respectively specified in Sofroniou and Spaletta (2005) and Kahan and Li (1997). When we use order two schemes $SABA_2$ (3.16) and $ABA82$ (3.18) in Equation (3.23) we construct the order six SIs $s9SABA_26$ (37 steps) and $s9ABA82\_6$ (73 steps) respectively. Similarly we construct SIs of order six using the order two integrators $SABA_2$ (3.16) and $ABA82$ (3.18) in Equation (3.22). The obtained integrators are namely $s11SABA_26$ (45 steps) and $s11ABA82\_6$ (89 steps) respectively.

SIs of order eight

We also consider in our study some order eight SIs using the composition schemes presented in Yoshida (1990) with 15 applications of an order two integrator. For order

two SIs $SABA_2$ (3.16) and $ABA82$ (3.18) we implement the schemes, of Yoshida (1990), whose coefficients are referred to as *Solution A* and *solution D*. More specifically we apply *solution A* to generate the integrators $SABA_2Y8A$ of 61 steps and $ABA82Y8A$ of 121 steps from respectively SIs $SABA_2$ and $ABA82$. Solution D has been reported by McLachlan (1995) and Sofroniou and Spaletta (2005) to perform better than the other composition schemes generated by this method. We therefore use solution D to generate integrators $SABA_2Y8D$ of 61 steps and $ABA82Y8D$ of 121 steps from SIs $SABA_2$ and $ABA82$ respectively.

In Kahan and Li (1997), various schemes of order 8 with different number of steps were constructed. From these, we consider the composition scheme $s15odr8$. Using $SABA_2$ (3.16) and $ABA82$ (3.18) in the place of S_2 we get the order eight SIs $s15SABA_28$ of 61 steps and $s15ABA82\_8$ of 121 steps respectively. In Section 4.3 of Sofroniou and Spaletta (2005), two schemes of order eight which require 19 and 21 applications of S_2 were given. We include in our analysis the scheme with 19 applications of S_2 because it requires fewer steps for a particular order two SI compared to the method where S_2 is applied 21 times. We call this scheme $s19odr8$. We now use $s19odr8$ to construct the order eight schemes $s19SABA_28$ of 77 steps and $s19ABA82\_8$ of 153 steps when we replace S_2 with $SABA_2$ (3.16) and $ABA82$ (3.18) respectively.

Symplectic integration schemes of order higher than eight

Numerical experiments performed [Sofroniou and Spaletta (2005)] have shown that composition of schemes of higher order would require double precision arithmetic in order to be efficient, something which would slow down the numerical computation. Secondly, unlike schemes of order smaller or equal to eight, there were inconsistencies in the solutions for higher order schemes depending on the processor used. We therefore do not include composition schemes of order greater than eight in our work.

3.3.2 Solving the equations of motion and the tangent map (TM) method

The equations of motion (3.8) can be written in terms of the differential operator (3.13) as

$$\left.\begin{aligned} \tfrac{d\mathbf{q}}{dt} &= \mathbf{p} \\ \tfrac{d\mathbf{p}}{dt} &= -\tfrac{\partial V(\mathbf{q})}{\partial \mathbf{q}} \end{aligned}\right\} \Longrightarrow \frac{d\mathbf{z}}{dt} = L_{_H}\mathbf{z},$$

where $\mathbf{z} = (\mathbf{q}, \mathbf{p})$ is a point in the phase space and $L_{_H}$ is defined in the same way as in (3.13). The operator $L_{_H}$ can be written as $L_{_H} = L_V + L_T$ where the time evolution maps corresponding to L_V and $L_{_T}$ are

$$e^{\tau L_V} = \begin{cases} \mathbf{q}' = \mathbf{q} + \tau\mathbf{p} \\ \mathbf{p}' = \mathbf{p} \end{cases} \quad \text{and} \quad e^{\tau L_T} = \begin{cases} \mathbf{q}' = \mathbf{q} \\ \mathbf{p}' = \mathbf{p} - \tau\frac{\partial V(\mathbf{q})}{\partial \mathbf{q}}. \end{cases} \tag{3.24}$$

We use the TM method (Section 3.1.2) to solve the variational equations (3.9). We

consider equations (3.8) and (3.9) as a unified set of differential equations

$$\left.\begin{aligned} \tfrac{d\mathbf{q}}{dt} &= \mathbf{p} \\ \tfrac{d\mathbf{p}}{dt} &= -\tfrac{\partial V(\mathbf{q})}{\partial \mathbf{q}} \\ \tfrac{d\delta\mathbf{q}}{dt} &= \delta\mathbf{p} \\ \tfrac{d\delta\mathbf{p}}{dt} &= -D_V^2(\mathbf{q})\delta\mathbf{p} \end{aligned}\right\} \Longrightarrow \frac{d\mathbf{u}}{dt} = L_{H_\mathcal{V}}\mathbf{u},$$

where $\mathbf{u} = (\mathbf{q}, \mathbf{p}, \delta\mathbf{q}, \delta\mathbf{p})$ is a vector formed by the phase space vector $(\mathbf{q}, \mathbf{p})$ and the deviation vector $(\delta\mathbf{q}, \delta\mathbf{p})$. $L_{H_\mathcal{V}}$ is used to solve the whole combined system of equations, in the phase and tangent space. The operator $L_{H_\mathcal{V}}$ can be written as $L_{H_\mathcal{V}} = L_{V_\mathcal{V}} + L_{T_\mathcal{V}}$ where the maps $L_{V_\mathcal{V}}$ and $L_{T_\mathcal{V}}$ give the equations

$$e^{\tau L_{V_\mathcal{V}}} = \begin{cases} \mathbf{q}' = \mathbf{q} + \tau\mathbf{p} \\ \mathbf{p}' = \mathbf{p} \\ \delta\mathbf{q}' = \delta\mathbf{q} + \tau\delta\mathbf{p} \\ \delta\mathbf{p}' = \delta\mathbf{p} \end{cases} \quad \text{and} \quad e^{\tau L_{T_\mathcal{V}}} = \begin{cases} \mathbf{q}' = \mathbf{q} \\ \mathbf{p}' = \mathbf{p} - \tau\frac{\partial V(\mathbf{q})}{\partial \mathbf{q}} \\ \delta\mathbf{q}' = \delta\mathbf{q} \\ \delta\mathbf{p}' = \delta\mathbf{p} - \tau D_V^2(\mathbf{q})\delta\mathbf{p}. \end{cases} \tag{3.25}$$

The new sets of equations (3.24) and (3.25) which respectively correspond to the equations of motion and variational equations can be used in the SIs and their explicit forms for the DKG Hamiltonians (2.19) and (2.22) are given in Appendix A.

3.4 Numerical results

In this Section we present numerical findings on the performance of the SIs that have been described in Section 3.3 for the integration of the equations of motion and variational equations of the 1D (2.19) and 2D (2.22) DKG models. Firstly, for each of the models, we systematically show how we select initial deviation vector to use in our investigation. We note that all of our simulations were performed on an Intel Xeon E5 – 2623 with 3.00 GHz. Our programs were written in the FORTRAN 90 programming language and we used the Intel Fortran (ifort) and gfortran Compiler Suites with an optimization level 2 (-O2).

3.4.1 Integration of the 1D DKG model

The initial deviation vector

Numerical computation of the mLCE (3.12), involves integration of variational equations for a very long time interval in order to get conclusive results about the nature of the dynamics. Here we compare various possible general forms of initial deviation vectors and investigate how they affect the solutions of the variational equations. To do this we compute the finite time mLCE and reproduce parts of a similar analysis that was presented in Gkolias (2013). We consider the following different initial deviation vectors (3.1).

1: a deviation vector whose central coordinate (corresponding to the middle site of the lattice) of both the position and momentum components is non-zero and all other coordinates of the vector are zero.

2: a deviation vector where (a few) more than one centrally positioned coordinates of both the positions and momenta components are non-zero and all other points of the vector are zero.

3: a deviation vector where all centre coordinates of both the positions and momenta components are zero except for a (few) number of coordinates at the boundaries of the vector.

4: a random deviation vector where all coordinates of both the positions and momenta components are non-zero.

The representative forms of these initial deviation vectors **1**, **2**, **3** and **4**, whose coordinate component numbers have been randomly generated, are presented in Figure 3.1. The panels **(a)**, **(b)**, **(c)** and **(d)** in Figure 3.1 show the DVDs $\xi_l^D(0)$ (3.2) plotted against the degrees of freedom (sites) l (where $1 \leq l \leq N = 1\,000$) for the initial deviation vectors of type **1** (red), **2** (green), **3** (purple) and **4** (blue) respectively.

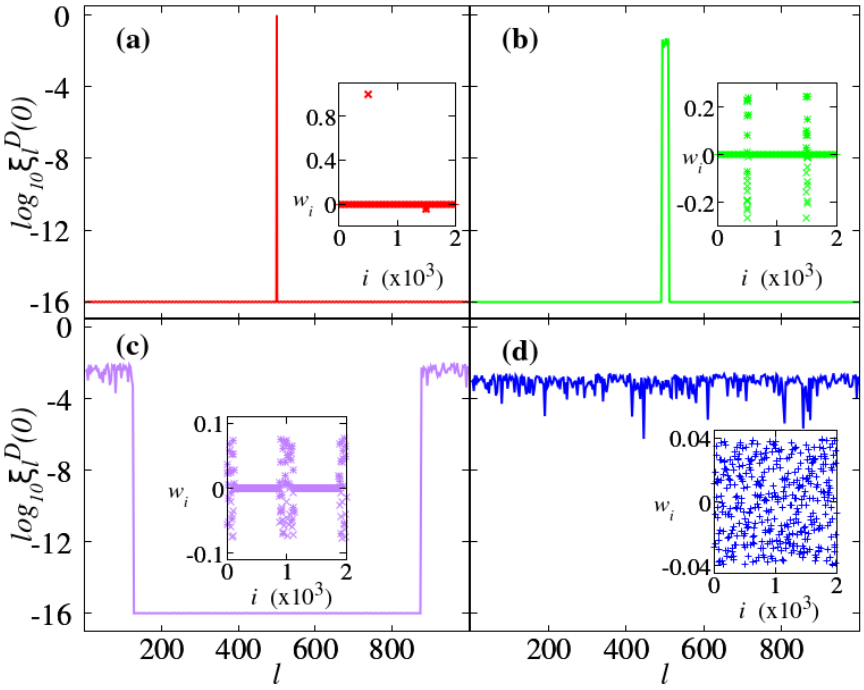

Figure 3.1: The DVDs $\xi_l^D(0)$ for initial deviation vectors **1** [red curves in **(a)**], **2** [green curves in **(b)**], **3** [purple curves in **(c)**] and **4** [blue curves in **(d)**]. The inset plots show the coordinates w_i of the initial deviation vectors $\mathbf{w} = (w_1, w_2, \cdots, w_{2N})$ (3.1). The plots are in linear-log scale and the insets are in log-log scale.

Each inset plot in panels **(a)**, **(b)**, **(c)** and **(d)** shows the corresponding actual deviation vector $\mathbf{w}$ (3.1) [shown using vector coordinates w_i] with the abscissa [labeled using i] representing positions coordinate components $\delta\mathbf{q}$ on one half to the left and momenta coordinate components $\delta\mathbf{p}$ on the other half to the right.

To study the dependence of $\Lambda(t)$ (3.11) on the initial deviation vector, we integrate the 1D DKG model (2.19) with single site excitation (i.e. participation number $P(0) = 1$) of the central oscillator using parameters: $W = 4$, lattice size $N = 1{,}000$ and total energy $H_{1K} = 0.4$, up to a final time $t_f \approx 10^{7.2}$. This set of initial conditions have been reported by Skokos et al. (2013) to belong to the weak chaos regime. We evaluate $\Lambda(t)$ and also monitor the evolution of the DVDs $\xi_l{}^D(t)$ for each of the different cases **1**, **2**, **3** and **4**. The initial values of the DVD participation number, $P^D(0)$, for the cases **1**, **2**, **3** and **4** are respectively 1, 21, 251 and 1 000. The non-zero coordinates of each of these deviation vectors were randomly generated using a uniform distribution on the interval $(-1, 1)$ with

random numbers allocated to each of the components δq_i and δp_i of the vector, as seen in the insets of Figure 3.1. During the integration we monitor the DVD's evolution and compute the corresponding finite time mLCEs. The time evolution of the DVDs up to $t = t_f \approx 10^{7.2}$ is shown in Figure 3.2 panels **(a)** [for **1**], **(b)** [for **2**], **(c)** [for **3**] and **(d)** [for **4**] where the horizontal colour bars show the values of the $\log_{10} \xi_l^D(t)$ (3.2). In all cases, the deviation vector eventually concentrate in the area of the lattice where the initial excitation was performed. The deviation vector **3** initially has no (non-zero) components concentrated around the sites where the excitation takes place.

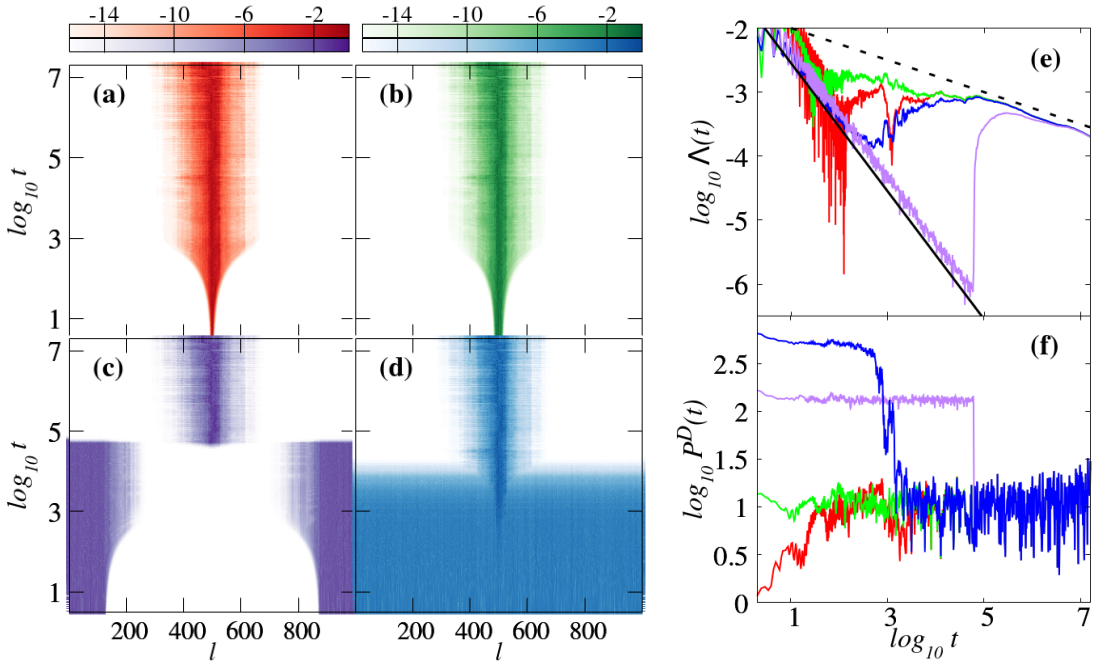

Figure 3.2: Results for the time evolution of the DVD for initial deviation vectors **1** [in **(a)**], **2** [in **(b)**], **3** [in **(c)**] and **4** [in **(d)**]. Time evolution of the finite time mLCEs $\Lambda(t)$ (3.11) [in **(e)**] and DVD participation number $P^D(t)$ (3.3) [in **(f)**] corresponding to the deviation vectors **1** (red curve), **2** (green curve), **3** (purple curve) and **4** (blue curve). The horizontal colour bars indicate the corresponding values of $\log_{10} \xi_l^D(0)$ (3.2). The continuous black and dashed lines in **(e)** respectively guide the eye for slopes -1 and $-1/3$. Panels **(a)**-**(d)** are in linear-log scale while **(e)** and **(f)** are in log-log scale.

For this reason, it takes the longest time (compared to all the other initial deviation vectors considered) before converging to the region where the dynamics takes place as shown in Figure 3.2**(c)**. In panels **(e)** and **(f)** of Figure 3.2 we report respectively the time evolution of the finite time mLCEs $\Lambda(t)$ and DVD participation number $P^D(t)$ for the different initial deviation vectors **1** (red curve), **2** (green curve) **3** (purple curve) and **4** (blue curve). The straight continuous line in **(e)** indicates the slope of $\Lambda(t)$ corresponding to the law $\Lambda(t) \propto t^{-1}$ (representing regular motion) while the dashed line shows the direction [characteristic slope for weak chaos law $\Lambda(t) \propto t^{-1/3}$ [Skokos et al. (2013)]] to which the finite time mLCEs $\Lambda(t)$ from the different initial deviation vectors eventually tend to. After $t = 10^6$, the evolution of $\Lambda(t)$ and $P^D(t)$ is independent of the initial deviation vector used in the corresponding integration as respectively seen in **(e)** and **(f)**. However, for initial deviation vector **2**, where more than one central coordinates of the deviation vector are non-zero and concentrated around excited sites, $\Lambda(t)$ converges fastest to the direction of convergence of all finite time mLCEs (i.e., the dotted line in Figure 3.2 **(e)**). The results of Figure 3.2 also show that the finite time mLCE rate of convergence to it's asymptotic value depends on the number of non-zero coordinates of the

initial deviation vector covering the excited sites and the position of these coordinates with respect to the region of excitation. We can clearly see in Figure 3.2**(e)** that for $P^D(0) = 1$ (initial deviation vector **1**), we require more integration time to observe convergence of $\Lambda(t)$ to the direction of the dotted line compared to when $P^D(0) = 21 > P(0) = 1$ (initial deviation vector **2**). We observe a similar behaviour in Figure 3.2**(f)** for the convergence of $P^D(t)$. For a vector of form **3**, in the first stages ($t < 10^{4.5}$) of the dynamics the deviation vector does not reveal the actual (weak chaos) dynamics of the system and so $\Lambda(t)$ shows the behaviour of regular motion as seen in Figure 3.2**(e)**. However, at a later stage (around $t \approx 10^{4.8}$) as the energy spreads (due to chaoticity in the system [Skokos et al. (2013)]) to more lattice sites, the system's true chaotic nature is characterised by the deviation vector and so $\Lambda(t)$ starts to show the expected behaviour following a law $\Lambda(t) \sim t^{-1/3}$. For the spatial extent of the DVD, we see in **(f)** that eventually for all initial deviation vectors, the participation number $P^D(t) \approx 10$ and case **2** converges to this value before any of the other three deviation vectors. For case **3**, during the initial integration stages ($t < 10^{4.5}$) when the system shows regular behaviour, the spatial extent of the deviation vector as characterised by the participation number P^D is practically fixed with $P^D(t < 10^{4.5}) \approx 251$. P^D then falls to $P^D(t \geq 10^5) \approx 10$ when the chaotic behaviour is reflected by Λ. For the fastest convergence to the eventual state of chaoticity (quantified using Λ) and DVD (quantified using the participation number P^D), we use in this work the deviation vector **2** whose non-zero component of the coordinates fully covers the sites that have been initially excited. That is to say, if we give the same energy to each initially excited site, then we set the deviation vector such that $\frac{P(0)}{P^D(0)} \lesssim 1$ for the 1D DKG model (2.19).

Efficiency of Symplectic integrators

Using the various SIs presented in Section 3.3 we numerically integrate the equations of motion of the 1D KG Hamiltonian (2.19) for different initial energy excitations and parameters. In this process, for a particular disorder realization we compute the quantities $m_2(t)$ (2.30), $P(t)$ (2.31), the energy distribution $\{\xi_l(t)\}$ (2.29) and the absolute relative energy error $e_r(t)$ which is given by

$$e_r(t) = \frac{|H_{1K}(t) - H_{1K}(0)|}{H_{1K}(0)}, \tag{3.26}$$

and we evaluate these quantities using all SIs. A reproduction of these measures using the different SIs ensures that we have the same dynamics or wave packet from each of the SIs. We also use the same initial deviation vector and we compute the time evolution of $\Lambda(t)$ as a way of checking that we accurately compute the level of chaoticity in the system across all SIs.

For our computations we work with a lattice of size $N = 1\ 000$, energy $H_{1K}(0)$, and disorder strength W. We excite a block of L adjacent sites at the centre of the lattice by giving each site energy $h = H_{1K}(0)/L$. We consider the following different sets of initial parameter conditions:

I: $L = 1$, $W = 4$ and $H_{1K}(0) = h = 0.4$
II: $L = 1$, $W = 4$ and $H_{1K}(0) = h = 1.5$
III: $L = 21$, $W = 4$, and $H_{1K}(0) = 4.2$, $(h = 0.2)$
IV: $L = 37$, $W = 3$, and $H_{1K}(0) = 0.37$, $(h = 0.01)$
V: $L = 100$, $W = 4$, and $H_{1K}(0) = 1$, $(h = 0.01)$
VI: $L = 1000$, $W = 4$, and $H_{1K}(0) = 10$, $(h = 0.01)$.

In Skokos et al. (2013) and Gkolias (2013) the cases I and IV have been reported to exhibit the weak chaos behaviour. In Gkolias (2013) case II has been reported to belong

to the strong chaos regime and case III to the strong chaos regime where some disorder realisations exhibited a crossover to weak chaos in a finitely long period of time. For the first four cases (I, II, III and IV), we restrict our evolutions to a system with fixed boundary conditions where we mimic the dynamics of a lattice with an infinite number of sites. We include cases V and VI as representations for general performances of the SIs on situations where the energy would eventually spread to all sites of the lattice. In each of the cases I-VI we initially give the same momentum to each of the excited site(s) with an allocation of random signs to each of these values while setting momentum to zero for all other sites. The displacements for all sites are initially set to zero. An initial deviation vector of the form **2** (Figure 3.1**(b)**) is used. We monitor the normalized energy distributions $\{\xi_l(t)\}_l$ (2.29) for $l = 1, \cdots, N$ and evaluate their second moment $m_2(t)$ (2.30) and participation number $P(t)$ (2.31) for $t \in [0, 10^7]$. During the simulations we adjust the integration time step so that the absolute relative energy error e_r is at a value smaller than 10^{-4}, a typically accepted level [Flach et al. (2009b); Skokos et al. (2009); Laptyeva et al. (2010); Flach (2010); Bodyfelt et al. (2011b)]. That is to say, we set $e_r(t) \lesssim 10^{-5}$. The computational efficiency of each scheme is evaluated by checking its ability to correctly reproduce the dynamics of the energy propagation within an acceptable precision range.

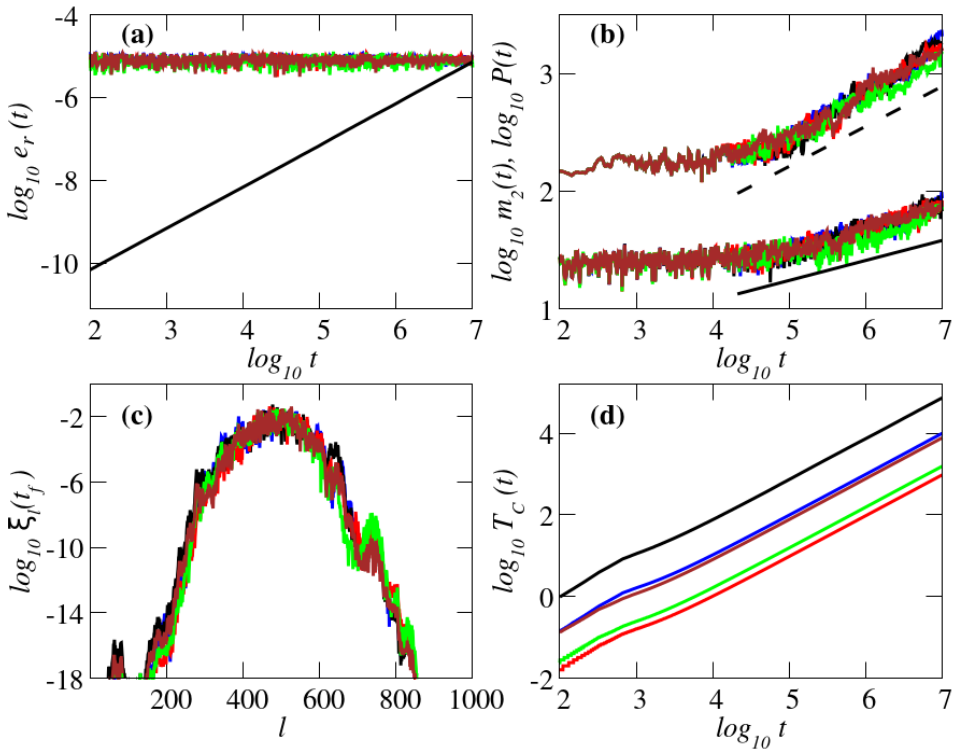

Figure 3.3: Results obtained for the integration of equations of motion for ICs IV (see text) of the 1D DKG Hamiltonian (2.19) by the integrators $ABA82$ of order two, $ABA864$ of order four, $SABA_2Y6$ of order six, $SABA_2Y8A$ of order eight and $RK4$ [blue, red, green, brown and black curves respectively]. **(a)** the time evolution of the absolute relative energy error $e_r(t)$ (3.26); **(b)** the time evolution of the second moment $m_2(t)$ (2.30) (upper curves) and participation number $P(t)$ (2.31) (lower curves); **(c)** the normalized energy distribution $\{\xi_l(t_f = 10^7)\}_l$ (2.29) as a function of lattice site index l; and **(d)** the time evolution of the required CPU time $T_C(t)$ in seconds. The straight lines in **(b)** guide the eye for slopes 1/3 (dashed line) and 1/6 (solid line). The five different curves practically overlap each other in panels **(a)**, **(b)** and **(c)**. Panels **(a)**, **(b)** and **(d)** are in $\log - \log$ scale and **(c)** is in linear $-$ log scale.

We therefore monitor the nature of the energy profiles as quantified by the distribution $\xi_l(t)$, and the time evolution of $e_r(t)$, $m_2(t)$, $P(t)$ and $\Lambda(t)$.
Figure 3.3 shows findings obtained for the evolution of the orbit by four SIs, namely $ABA82$ of order 2 (blue curves), $ABA864$ of order 4 (red curves), $SABA_2Y6$ of order 6 (green curves), $SABA_2Y8A$ of order 8 (brown curves) and the fourth order non symplectic Runge-Kutta $RK4$ [Runge (1895); Weiner and Strehmel (1992)] (black curves) integrator for ICs IV. We include $RK4$ as a representative integrator for non symplectic schemes amidst SIs. All integrators studied produce the same dynamical evolution of the model as the results for $m_2(t)$ (upper curves of Figure 3.3**(b)**), $P(t)$ (lower curves of Figure 3.3**(b)**) and the normalized energy profiles (Figure 3.3 **(c)**) at the final integration time $t_f = 10^7$ practically overlap. We note that by the final integration time $t_f = 10^7$, the energy had not yet reached the boundaries of the lattice as clearly shown in panel **(c)**. The results of Figure 3.3**(b)** show that the wave packet's $m_2(t)$ and $P(t)$ eventually grow respectively as $m_2(t) \propto t^{1/3}$ (direction of black dashed line in Figure 3.3**(b)**) and $P(t) \propto t^{1/6}$ (direction of black continuous line in Figure 3.3**(b)**), in agreement with previously published works [Flach et al. (2009a,b); Skokos et al. (2009); Laptyeva et al. (2010); Bodyfelt et al. (2011b)]. The CPU time, T_C, time evolution for each integrator is shown in Figure 3.3**(d)**. From this result, clearly the $ABA864$ scheme shows the best performance from all the five integrators shown in the figure requiring the least CPU time for the integration. We note that the time step $\tau = 0.006$ used for the integrator $RK4$ maintains $e_r(t)$ (3.26) below 10^{-5} for the whole computation. For shorter integration times smaller than $t = 10^7$, $RK4$ is more accurate since it has the least change in energy H_{1K} (as seen in Figure 3.3**(a)**) compared to the other four schemes presented in Figure 3.3, but it requires more CPU time (as seen in Figure 3.3**(d)**). Under these conditions, integration by $RK4$ beyond $t = 10^7$ would lead to the system losing it's energy conservation property beyond the acceptable accuracy level of $e_r(t) \approx 10^{-5}$. This change in energy beyond the desired accuracy can be avoided for very long integration times by reducing the time step, which in turn slows the computations and hence an increased CPU time for the $RK4$. A more detailed account of the findings for this integrator comparison are presented in Table 3.1.

More precisely, Table 3.1, shows information on the performance of the SIs of order n used for the integration of the equations of motion (2.21) of the 1D KG model (2.19) up to a final time $t_f = 10^7$ for the initial excitation of cases I, IV and VI. The number of SI integration steps (S) is given and for case IV the integration time step τ which keeps $e_r(t) \lesssim 10^{-5}$ for all t is listed. The required CPU time in seconds, T_C, needed for each integrator is also reported. From the results of this table we see that the SIs exhibiting the best performance are: the order four schemes $ABA864$, $ABAH864$ and the order six schemes $SABA_2Y6$, $s9SABA_26$, $ABA864Y6$ in descending order of computational efficiency. Only the CPU times for the SIs that are stable (where $e_r(t)$ remains practically constant) in each of the cases have been reported in Table 3.1. In order to get best performance from each of the SIs, we choose a time step τ which is big enough to keep $e_r(t)$ as close as possible to 10^{-5}. The SIs of order two require very high CPU times of the order of 10^4 seconds compared to the many other better performing SIs, so we only include their results for IC IV. Also, some of the SIs whose theory was discussed in Section 3.3.1 have not been included in Table 3.1 as they do not maintain the value of $e_r(t)$ bounded around 10^{-5} because they require relatively huge values of τ which makes them unstable (with values of $e_r(t)$ fluctuating highly and far from the value 10^{-5}). However, some of these SIs give a fairly and competitively good performance at higher accuracies $e_r(t) < 10^{-5}$. Nonetheless, they still do not feature among the top most efficient SIs. For example, the SI $ABA82Y8D$ which is unstable at $e_r(t) \approx 10^{-5}$ requires a CPU time of approximately 5×10^4 seconds for an accuracy $e_r(t) \approx 10^{-6}$ where it is stable. On the other hand, the SI $SABA_2Y8A$,

which is stable at $e_r(t) \approx 10^{-5}$, requires a larger CPU time of approximately 7×10^4 seconds at this accuracy. However, there are still many more SIs that have a final CPU time T_C that is smaller than that of $ABA82Y8D$, and so it does not appear amongst the top SIs. We note that each of the SIs included in Table 3.1 showed stability for all the six ICs I - VI considered.

			I	IV		VI
SI	n	S	T_C	τ	T_C	T_C
$ABA82$	2	9		0.04	8530	
$SABA_2$	2	5		0.02	12780	
$SBAB_2$	2	5		0.02	14430	
LF	2	3	22350	0.01	32280	33740
$ABA864$	4	15	820	0.56	840	820
$ABAH864$	4	17	1290	0.38	1350	1300
$ABA82Y4$	4	25	2310	0.26	2630	2700
$SABA_2C$	4	7	2170	0.19	3350	2110
$FR4$	4	7	3040	0.09	3310	3040
$SABA_2Y4$	4	13	2620	0.12	3560	3350
$SBAB_2Y4$	4	13	2900	0.12	3840	3620
$SBAB_2C$	4	7	2970	0.14	4780	3140
$SABA_2Y6$	6	29	1310	0.55	1400	1300
$s9SABA_26$	6	37	1440	0.67	1410	1320
$ABA864Y6$	6	43	1640	0.65	1650	1590
$SBAB_2Y6$	6	29	1700	0.46	1750	1660
$s9ABA82\_6$	6	73	*4260	0.93	1920	*2870
$FR4Y6$	6	19	2860	0.18	3090	3010
$SABA_2CY6$	6	19	1800	0.37	3240	2190
$SABA_2Y4Y6$	6	37	3380	0.28	3370	3380
$SBAB_2Y4Y6$	6	37	3870	0.28	3850	3610
$SABA_2Y8A$	8	61	6590	0.20	7290	6820
$ABA82Y8A$	8	121	13600	0.22	12470	11700

Table 3.1: Results obtained for the integration of the equations of motion (2.21) for some of the investigated ICs I, IV and VI (see text) of the 1D DKG Hamiltonian (2.19). The respective order n, number of steps S, CPU times T_C (in seconds) required for integrating the equations of motion up to a time $t_f = 10^7$, the integration time steps τ used for initial condition IV are reported. (*) shows CPU times obtained at a stable value $e_{\mathbf{r}}(t) < 10^{-5}$.

We clearly see that the order four integrator $ABA864$ gives the best performance for the integration of the equations of motion of the 1D DKG model (2.19) basing on the results in Table 3.1. The performance rankings shown in this table for the cases I, IV and VI are similar to those of cases II, III and V with the $ABA864$ giving the smallest CPU time. We now extend this study to solving variational equations of the 1D DKG model. In Figure 3.4 we present results based on the numerical integration of the variational equations (3.9) for the 1D DKG Hamiltonian (2.19) as obtained using the best five SIs for

the weak chaos case IV [Figure 3.4**(a)**, **(b)** and **(c)**], as well and the fully chaotic excitation case VI [Figure 3.4**(d)**, **(e)** and **(f)**]. From panels **(a)** and **(d)** we see that the absolute relative energy error $e_r(t)$ is practically independent of time at a value $e_r(t) \approx 10^{-5}$ for all SIs. Similarly, for a particular case of initial excitation, the time evolution of $\Lambda(t)$ (3.11) is qualitatively the same for all these SIs as seen in each of the panels **(b)** and **(e)**.

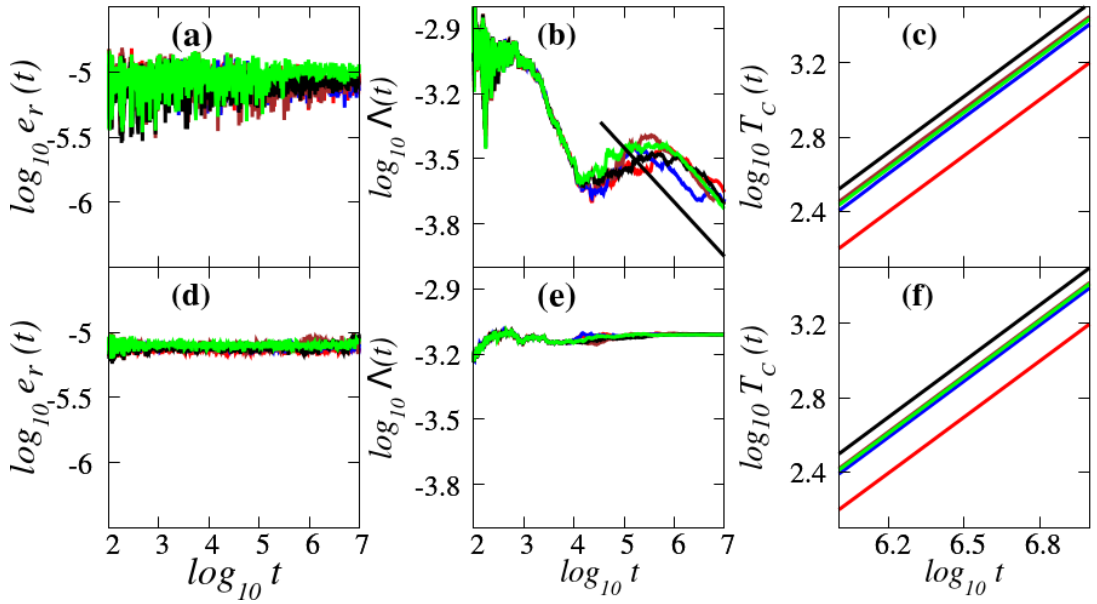

Figure 3.4: Results obtained for the integration of the variational equations (3.9) of the 1D DKG Hamiltonian (2.19) for cases IV [**(a)**, **(b)** and **(c)**] and VI [**(d)**, **(e)** and **(f)**] for the SIs $ABA864$, $ABAH864$, $ABA864Y6$, $s9SABA_26$ and $SABA_2Y6$ [red, blue, black, brown and green curves respectively]: the time evolution of $e_r(t)$ (3.26) [**(a)** and **(d)**], $\Lambda(t)$ (3.11) [**(b)** and **(e)**] and of the required CPU time $T_C(t)$ [**(c)** and **(f)**]. The straight solid line in **(b)** guides the eye for slope $-1/4$. All curves in panels **(a)**, **(d)** and **(e)**, and those for $s9SABA_26$, $SABA_2Y6$ in panels **(c)**, and **(f)** practically overlap. The panels are in $\log - \log$ scale.

In the weak chaos case IV, the finite time mLCE $\Lambda(t)$ (panel **(b)**) eventually decreases in a way similar to what was reported in Skokos et al. (2013), following the law $\Lambda(t) \propto t^{-\alpha_\Lambda}$, with $\alpha_\Lambda = -1/4$. The observed value of $\alpha_\Lambda = -1/4$ is different from the value -1, a value indicating the behaviour for regular orbits. This shows that for this particular disorder realisation, the strength of chaoticity which is measured by Λ [shown in Figure 3.4**(b)**] decreases as the wave packet extends [spreading shown by $m_2(t)$ in Figure 3.3**(b)**] without showing any tendency of the dynamics to exhibit regular behaviour for the entire duration of the integration [Skokos et al. (2013)]. In Chapter 4, we give a more detailed discussion on the 1D DKG model and substantiate on the persistence or relaxation of chaos using better statistics with more dynamical quantities.
For the fully chaotic case VI, the saturation of $\Lambda(t)$ [Figure 3.4**(e)**] to a constant positive value is very fast, showing the typical behaviour of chaos. The SIs give a similar performance for the different ICs as shown in Figure 3.4**(c)** and **(f)**, an indication that their efficiency is independent of the ICs. We also need to check if the computational efficiency as presented in Table 3.1 and Figure 3.4 is independent of the accuracy level $e_r(t)$.

For the case when a high accuracy is needed e.g. for $e_r \approx 10^{-8}$, the time step τ is set to smaller values. Through an appropriate reduction in the time step τ, all SIs that

have been investigated are stable at the absolute relative energy error $e_r \lesssim 10^{-8}$. We perform an analysis similar to the one performed when creating Table 3.1 and Figure 3.4 for the accuracy level $e_r \approx 10^{-8}$ and we present the results for the most efficient SIs on integration of variational equations for case IV in Figure 3.5.
From Figure 3.5**(a)** we see that for each SI considered, the time step τ was chosen so that $e_r(t) \approx 10^{-8}$ with all SIs successfully reproducing the same wave packet characterised by the time evolution laws $m_2(t) \propto t^{1/3}$, $P(t) \propto t^{1/6}$ [Figure 3.5**(b)**] and $\Lambda(t) \propto t^{-1/4}$ [Figure 3.5**(c)**]. The corresponding time steps τ used in ICs case IV to attain this accuracy are also given.

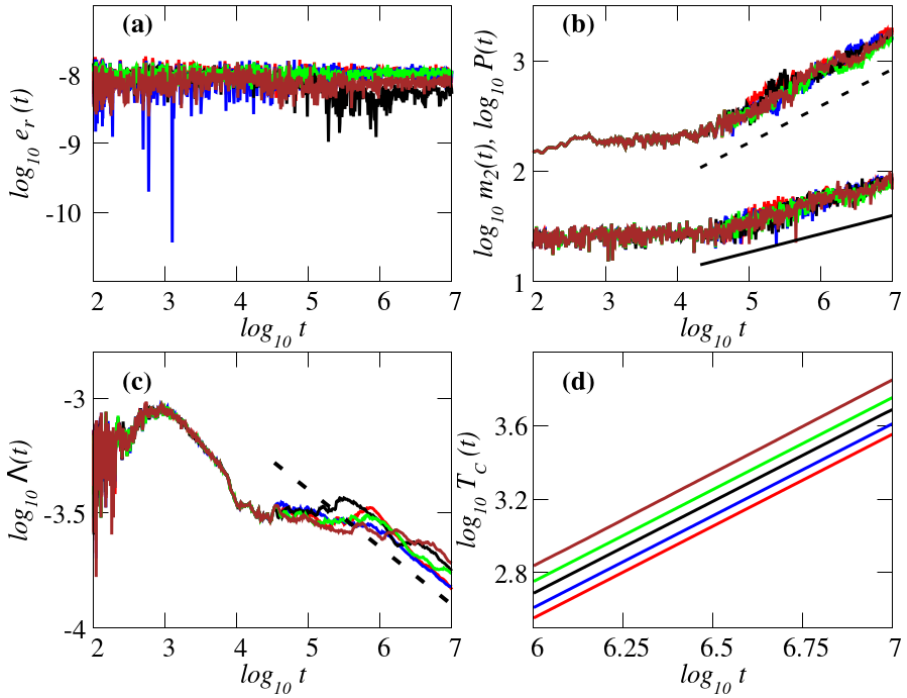

Figure 3.5: Results obtained for the integration of the variational equations of the 1D DKG Hamiltonian (2.19) for the case of ICs IV by the order six SI $s11ABA82\_6$ for $\tau = 0.42$, order eight SI $s15ABA82\_8$ for $\tau = 0.48$, order eight SI $s19ABA82\_8$ for $\tau = 0.59$, order six SI $s9ABA82\_6$ for $\tau = 0.50$ and order six SI $SABA_2Y6$ for $\tau = 0.18$ [red, blue, black, brown and green curves respectively]. The time evolution of **(a)** $e_r(t)$ (3.26), **(b)** $m_2(t)$ (2.30) and $P(t)$ (2.31) [upper and lower curves respectively], **(c)** $\Lambda(t)$ (3.11) and **(d)** CPU time $T_C(t)$. The straight lines in **(b)** guide the eye for slopes 1/3 (black dashed line) and 1/6 (black solid line), while in **(c)** the straight dashed line corresponds to slope $-1/4$. All panels are in $\log - \log$ scale.

We note that the chaotic behaviour observed for $e_r(t) \approx 10^{-5}$ persists for high accuracy level $e_r(t) \approx 10^{-8}$ with $\Lambda(t)$ following the same power law as was observed in Figure 3.4. For each set of the six ICs, all the five SIs presented in Figure 3.5 require more CPU time than that used to obtain $e_r(t) \approx 10^{-5}$ [Figure 3.4**(c)**]. At the accuracy $e_r(t) \approx 10^{-8}$, the time step is very small for the lower order SIs especially the SIs of order two and so they are successively applied for very high number of times during integration leading to a huge growth in the required CPU time. For the accuracy $e_r(t) \approx 10^{-8}$, the five best performing SIs are $s11ABA82\_6$, $SABA_2Y6$ and $s9ABA82\_6$ of order six, and $s15ABA82\_8$ and $s19ABA82\_8$ of order eight.
We now investigate the generality of our results in integrating Hamiltonian lattices of spatial dimension greater than one by considering the 2D DKG model (2.22) in the next section.

3.4.2 Integration of the 2D DKG model

Here we present a numerical study for the 2D DKG model (2.22), similar to the discussion of the 1D DKG system (2.19) reported in Section 3.4.1.

The initial deviation vector

In order to investigate the dependence of finite time mLCE $\Lambda(t)$ (3.11) and other deviation vector related quantity computations on the nature/kind of the initial deviation vector for the 2D DKG model, we performed similar tests like the ones of Section 3.4.1. For this purpose, the following different forms of initial deviation vectors are considered:

- **1**: a deviation vector whose central coordinate (corresponding to the middle site of the lattice) of both the position and momentum components is non-zero and all other coordinates of the vector are zero.
- **2**: a deviation vector where several centrally positioned coordinates of both the positions and momenta components are non-zero and all other elements of the vector are zero.
- **3**: a deviation vector where all centre coordinates of both the positions and momenta components are zero except for a number of coordinates at the boundaries of the lattice.
- **4**: a random deviation vector where all coordinates of both the positions and momenta components are non-zero.

In Figure 3.6 we see the projections of these initial deviation vectors **1** [red, panel **(a)**], **2** [green, panel **(b)**], **3** [purple, panel **(c)**] and **4** [blue, panel **(d)**] on the 2D space.

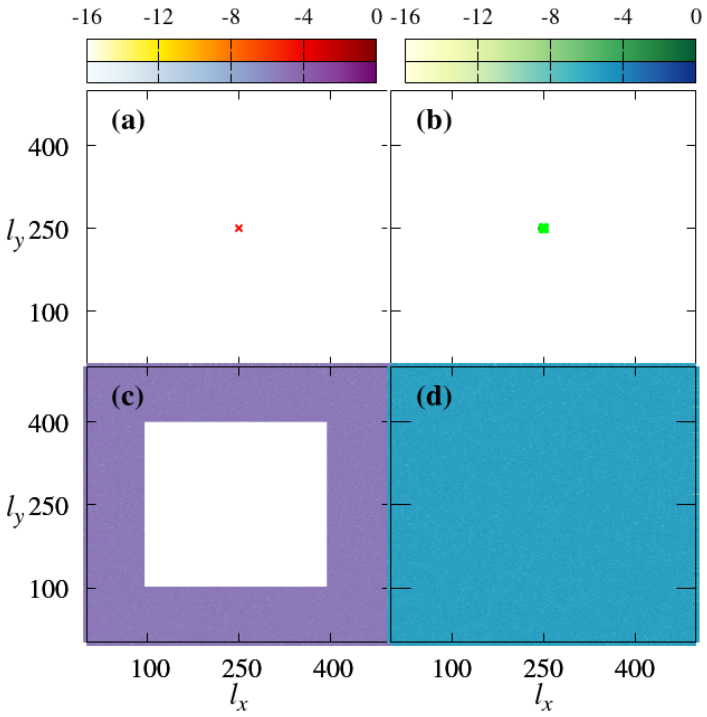

Figure 3.6: Projection of the initial deviation vectors **1** [**(a)** red], **2** [**(b)** green], **3** [**(c)** purple] and **4** [**(d)** blue] on the 2D space. The horizontal colour bars indicate the corresponding values of $\log_{10} \xi^D_{\mathbf{r}}(0)$ (3.2) where $\mathbf{r}$ is of the form (l_x, l_y) for $l_x, l_y \in \{1, 2, \cdots, 501\}$.

In order to understand the dependence of dynamical quantities (for example $\Lambda(t)$ (3.11) and $P^D(t)$ (3.3)) on the initial deviation vector, we integrate the variational equations of

the two dimensional DKG system (2.22). We use a 2D square lattice, $N \times M = 501 \times 501$, of 501 sites in one spatial dimension (x) and 501 sites in a perpendicular spatial dimension (y), strength of disorder $W = 10$ and we excite the middle site of the lattice with energy $H_{2K} = \xi_{(251,251)}(0) = 0.3$. This configuration has been reported in Laptyeva et al. (2012) to belong to the weak chaos regime. We compute $\Lambda(t)$ (3.11) while monitoring the evolution of the DVDs for each case: **1** (non-zero values for only the coordinates corresponding to the middle site of the lattice for both the position and momentum. i.e $P^D(0) = 1$), **2** (7×7 sublattice centre coordinates of both the position and momentum components are non-zero. i.e. $P^D(0) = 49$), **3** (301×301 sublattice centre coordinates of both the position and momentum components are zero and all the remaining coordinates are non-zero. i.e. $P^D(0) = 1.604 \times 10^5$) and **4** (all coordinates of both the position and momentum components are non-zero. i.e $P^D(0) = 501^2$).
Figure 3.7 shows the time evolution of the DVDs for deviation vector cases **1** and **4** with the colour gradients representing the logarithm of the values of the $\xi^D_{\mathbf{r}}(t)$ (3.2) as indicated in Figure 3.6.

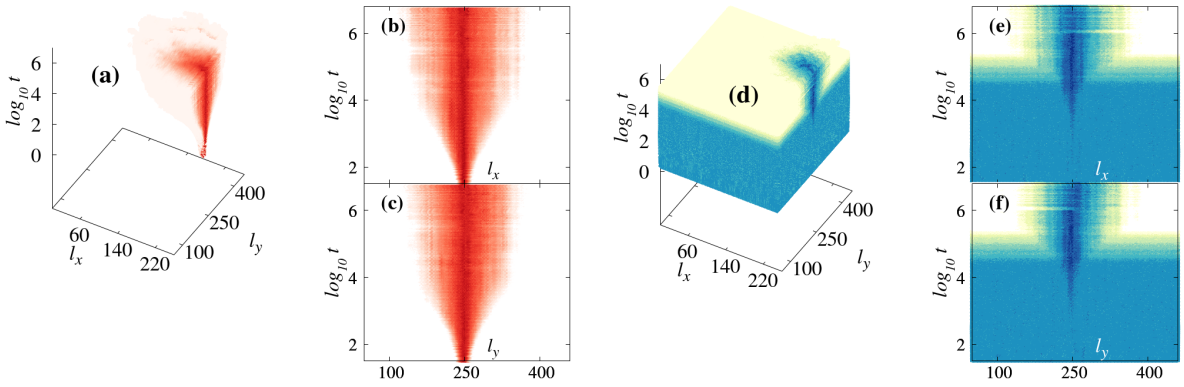

Figure 3.7: The time evolution of initial deviation vectors **1** (red) and **4** (blue). A 3D time evolution with a cross-section at $l_x = 251$ in panels **(a)** and **(d)**. A 1D time evolution at cross-section $l_x = 251$ [panels **(c)** and **(f)**] and cross-section $l_y = 251$ [panels **(b)** and **(e)**]. The plots are in linear − log (for 2D) and linear − linear − log (for 3D) scales.

The evolution of **1** is shown in panels **(a)**, **(b)** and **(c)** while the evolution of **2** is shown in panels **(d)**, **(e)** and **(f)**. Panels **(a)** and **(d)** show a 3D plot for the time (vertical axis) evolution of the DVDs in the phase space with the $x-$coordinates considered from $l_x = 1$ up to $l_x = 251$. The 1D time evolution front faces of panels **(a)** and **(d)** which correspond to the $x-$coordinate $l_x = 251$ are respectively shown in panels **(c)** and **(f)**. Similarly the corresponding 1D time evolution corresponding to $l_y = 251$ are shown in panels **(b)** and **(e)**. From Figure 3.7 we see that by $t \approx 10^6$, the deviation vectors are qualitatively the same for the two cases. For longer times, this is the same qualitative behaviour for all cases of initial deviation vectors. We also see that just like in the 1D DKG case, the deviation vector eventually concentrates around the degrees of freedom where the excitation takes place. This shows that the choice of initial deviation vector does not affect it's asymptotic dynamics. However, the kind of deviation vector that takes the least integration time to give the long term dynamical behaviour is preferred for our numerical computations.
In Figure 3.8 we report the evolution of the quantities $\Lambda(t)$ (3.11) and $P^D(t)$ (3.3) whose evolution depends on the deviation vector. The black continuous line in Figure 3.8**(a)** guides the eye along the slope -1, indicating $\Lambda(t)$ decay power law for regular dynamics. By the integration time $\log_{10} t \approx 6.5$ the value of $\Lambda(t)$ is qualitatively independent of

the corresponding initial deviation vector used in the integration for the cases **1**, **2** and **4** while case **3** requires additional integration time to saturate at the same level as the other cases. However, all the exponents for the four cases converge to a limit direction line (black dashed line) as seen in panel **(a)**. For the initial deviation vector **2**, where more than one central coordinates of the vector are non-zero and concentrated around the sites where the initial excitation takes place, $\Lambda(t)$ converges fastest to the direction of the dashed line. Once again, just like in the case of the 1D DKG model, the results also show that the rate of convergence of the finite time mLCE depends on the size of the non-zero component of the coordinates of the initial deviation vector covering the excited site(s) and the concentration of these coordinates with respect to the region of energy excitation.

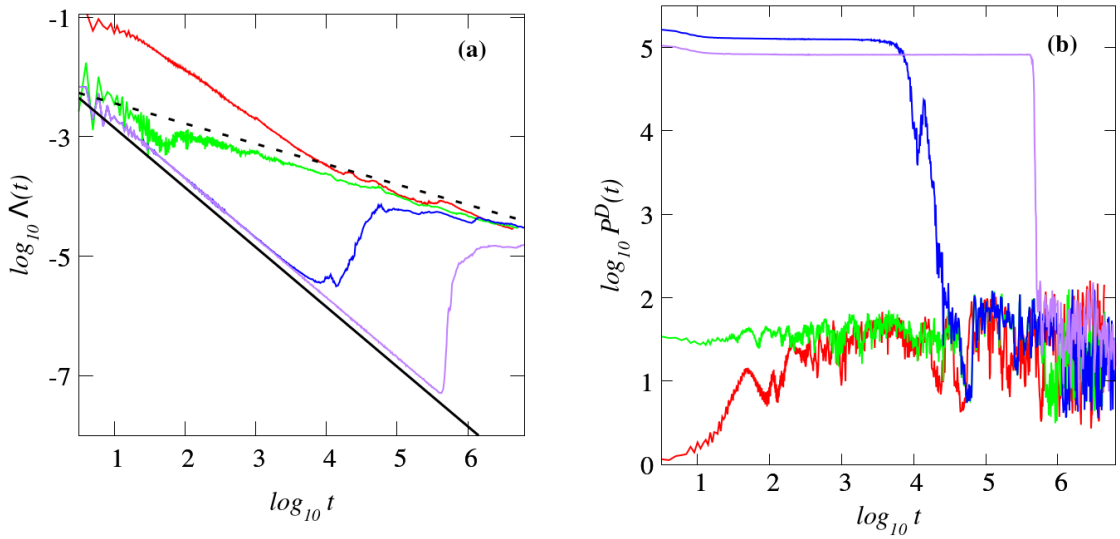

Figure 3.8: Results for the time evolution of **(a)** the mLCE $\Lambda(t)$ (3.11) and **(b)** $P^D(t)$ (3.3) for the initial deviation vectors **1** (red curve), **2** (green curve), **3** (purple curve) and **4** (blue curve). The black continuous line guides the eye for a slope -1 and the black dashed line estimates the direction of convergence of the exponents. The plots are in log-log scale.

We can clearly see in Figure 3.8**(a)** that for $P^D(0) = 1$ (red curve of case **1**), we require more integration time to observe convergence of the finite time mLCE to the direction of the dashed line compared to when $P^D(0) = 49 > 1$ (green curve of **2**). For the initial deviation vector **3**, during the initial stages of the dynamics the vector behaves like a zero vector around the degrees of freedom where the excitation takes place and so $\Lambda(t)$ shows the behaviour observed in the case of regular motion as seen in Figure 3.8**(a)** (purple curve). At a later stage (around $t \approx 10^{5.8}$) of the dynamics however, when the energy has spread to more lattice sites, the deviation vector behaves as expected (non-zero vector) and therefore $\Lambda(t)$ changes and starts showing a chaotic behaviour. For the fastest convergence of the $\Lambda(t)$ to the asymptotic direction [dashed line in Figure 3.8**(a)**], we take the initial deviation vector **2** whose non-zero component of it's coordinates fully covers the sites that have been initially excited. That is to say that, if we give the same energy to each initially excited site, then we set the deviation vector such that it's component with non-zero coordinates just covers the sites where the initial excitation has taken place and $\frac{P^D(0)}{P(0)} \gtrsim 1$. We note that case **4** is not our preferred choice of vector because $\frac{P^D(0)}{P(0)} \gg 1$, and this is why we have the kind of observed delay in convergence of $\Lambda(t)$.
For the next and proceeding sections of this work, we use initial vectors of the form **2** whenever our computations involve deviation vectors in two spatial dimensions.

Efficiency of Symplectic integrators

For the 2D DKG model (2.22), we perform an analysis similar to the discussion of Section 3.4.1 for the 1D model (2.19). We numerically integrate the equations of motion (2.24) for different initial excitations and parameters. In this process, for a particular set of random disorder numbers $\epsilon_{\mathbf{r}}$, we compute the quantities $m_2(t)$ (2.34), $P(t)$ (2.35), the normalised site energies $\xi_{\mathbf{r}}(t)$ (2.33) and the absolute relative energy error $e_r(t)$ given by

$$e_r(t) = \frac{|H_{2K}(t) - H_{2K}(0)|}{H_{2K}(0)}, \tag{3.27}$$

similar to Equation 3.26. We compute all these quantities using the SIs we presented in Section 3.3.1. We also compute $\Lambda(t)$ as a way of checking that all SIs correctly estimate the same level of chaoticity in the system. For our computations we work with a Hamiltonian lattice of 40,000 degrees of freedom with dimensions $N = 200$ and $M = 200$. We excite a rectangular block of $n \cdot m$ sites (with dimensions $n \leq N$, $m \leq M$) which is positioned at the lattice centre for a disorder strength W and an energy $H_{2K}(0)$ (or energy per excited site $h = \frac{H_{2K}(0)}{nm}$). We consider the following different sets of initial conditions and parameters:

I: $n = m = 1$, $W = 10$ and $H_{2K}(0) = h = 0.3$,
II: $n = m = 1$, $W = 10$ and $H_{2K}(0) = h = 2$,
III: $n = m = 200$, $W = 10$, and $H_{2K}(0) = 10$, $(h = 2.5 \times 10^{-4})$.

Cases I and II have been reported to belong to the weak and selftrapping regimes of chaos respectively [Laptyeva et al. (2012)], while case III was included to investigate the general performance of SIs for situations where the energy of the system reaches the boundaries of the lattice. The lattice size was chosen such that for the two cases I and II, the energy of the system never reaches the boundary sites. In each of the cases we give the same momentum to each of the excited site(s) (with these sites bearing random signs) and we set the momentum to zero for all other sites. We also start with no displacements for all sites of the lattice. As a result of the discussion in the preceeding section, we set the initial deviation vector in such a way that it has non zero random numbers at the coordinates which correspond to the sites that have been initially excited. That is to say, the initial deviation vector in the form we referred to as **2**. In particular, we use an initial deviation vector whose non-zero coordinates just cover a square lattice of 16 sites with dimensions 4×4 when integrating the variational. We consider the normalized energy distributions $\{\xi_{\mathbf{r}}(t)\}_{\mathbf{r}}$ (2.33) for $\mathbf{r} \in \{1, \cdots, N\} \times \{1, \cdots, M\}$ and evaluate their second moment $m_2(t)$ (2.34) and participation number $P(t)$ (2.35). For each simulation we set the integration time step so that the relative energy error $e_r(t)$ is bounded from above by 10^{-5}. We then evaluate the efficiency of the schemes by checking their ability to produce the same dynamics of the energy propagation. This is done by considering the shape of the computed energy profiles and the time evolution of $e_r(t)$, $m_2(t)$, $P(t)$ and $\Lambda(t)$.

In Figure 3.9 we present results obtained for case I by implementing the five best performing SIs among the studied schemes, for $e_r(t) \approx 10^{-5}$ [Figure 3.9**(c)**]. These are the same five SIs which exhibited the best numerical performance in the 1D DKG model (Figure 3.4), namely, order four SIs $ABA864$, $ABAH864$ and order six SIs $SABA_2Y6$, $s9SABA_26$, $ABA864Y6$. All these SIs captured the same dynamics of the system as seen by the overlapping curves in panels **(a)**, **(b)**, **(c)**, **(d)** and **(e)** of Figure 3.9. We present in Figure 3.9**(a)** the energy profiles along the $x-$axis for sites where the $y-$value is fixed at $l_y = 100$ at the final integration time $t_f = 10^6$. Panel **(b)** shows the corresponding energy profile along the $y-$axis for sites where the $x-$value is fixed at $l_x = 100$ at the final integration time. In each of the two cross-sections the curves of the profiles from the different SIs overlap. Also, the implemented SIs produce the same time evolution of

m_2 and P [Figure 3.9**(d)**] and Λ [Figure 3.9**(e)**]. The results in Figure 3.9**(d)** show that eventually both the second moment and participation number behave as $m_2(t), P(t) \propto t^{0.2}$, indicating that the dynamics belong to the weak chaos regime, a confirmation of the findings of Laptyeva et al. (2012).

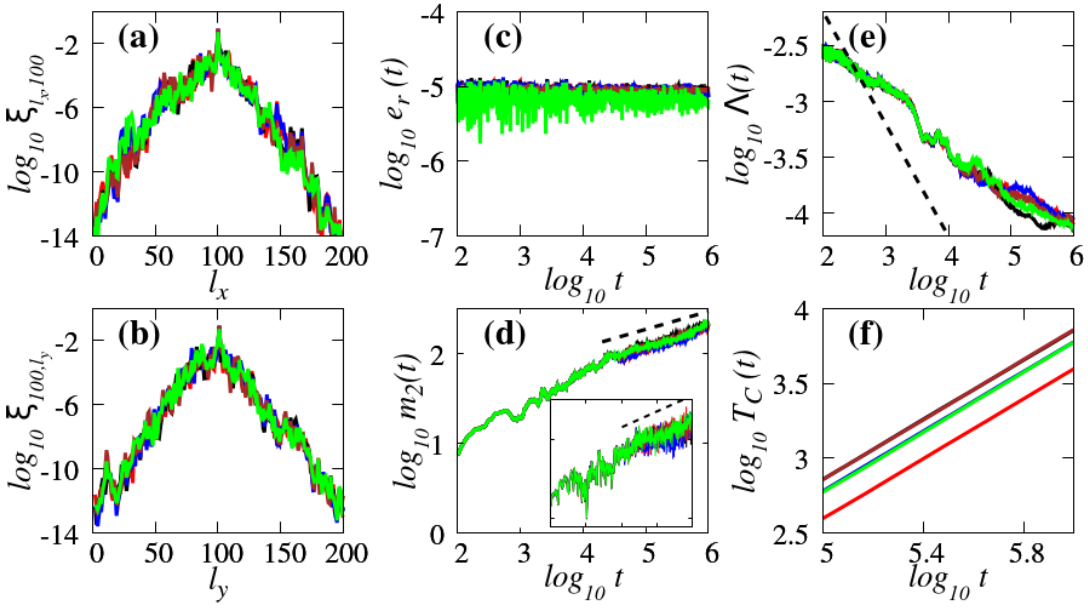

Figure 3.9: Results obtained for the numerical integration of case I of the 2D DKG model (2.22) by order four SIs $ABA864$ for time step $\tau = 0.56$, $ABAH864$ for $\tau = 0.40$ and order six schemes $ABA864Y6$ for $\tau = 0.68$, $s9SABA_26$ for $\tau = 0.60$, $SABA_2Y6$ for $\tau = 0.60$ [red, blue, black, brown and green curves]. **(a)** the normalized energy distributions $\xi_{l_x,100}$ and **(b)** ξ_{100,l_y} respectively at the final integration time $t_f = 10^6$ as functions of the lattice site indices l_x and l_y. The time evolution of **(c)** $e_r(t)$, **(d)** $m_2(t)$ and $P(t)$ [inset], **(e)** $\Lambda(t)$ and **(f)** $T_C(t)$. The dashed lines in **(d)** and it's inset plot guide the eye for slope 0.2 while for **(e)** a slope -1. The curves in panels **(a)**-**(e)** overlap while for **(f)** the curves for $ABAH864$, $SABA_2Y6$ and $s9SABA_26$, $ABA864Y6$ practically overlap each other. Panels **(a)**-**(b)** are in linear-log scale while **(c)**-**(f)** are in log-log scale.

In panel **(e)** we present the time evolution of $\Lambda(t)$, with the dashed line guiding the eye

	I		II		III	
SI	τ	T_C	τ	T_C	τ	T_C
$ABA864$	0.56	3950	0.35	6230	0.73	5550
$ABAH864$	0.40	5980	0.25	9270	0.51	8700
$SABA_2Y6$	0.60	5960	0.38	9230	0.71	9190
$s9SABA_26$	0.60	7230	0.37	10740	0.85	9300
$ABA864Y6$	0.68	7170	0.40	11510	0.84	10960
$SBAB_2Y6$	0.58	11400	0.36	17370	0.73	17130

Table 3.2: Similar to Table 3.1 but for the 2D DKG model (2.22). Information on the performance of the most efficient SIs used for the integration of the variational equations of the 2D DKG model at $e_r(t) \approx 10^{-5}$ up to final time $t_f = 10^6$ for the initial excitation of cases I-III (see text). The integration time step τ used for obtaining the respective absolute relative energy error levels $e_r(t)$ and the required CPU time $T_C(t_f)$ (seconds) needed for each integrator are reported.

for the slope observed in the case of regular dynamics (slope -1). $\Lambda(t)$ therefore shows a power law decay different from that of regular dynamics with no sign of the dynamics slowing down to exhibit regular behaviour.
In Table 3.2, we present results for the 2D DKG model, including computation of $\Lambda(t)$ for longer times, considering some typical representative cases and for various system parameters to give a global perspective of the system's dynamics. From Figure 3.9**(f)** we see that, for case I and at the accuracy of $e_r(t) \approx 10^{-5}$ [panel **(c)**], the most efficient SI is $ABA864$ followed by $ABAH864$, $SABA_2Y6$ and $s9SABA_26$, $ABA864Y6$. We present, in Table 3.2, findings for all the three considered cases I, II and III reporting the CPU times for the top six SIs at moderate accuracy $e_r \approx 10^{-5}$. The time steps that maintain the energy of the systems at the specified accuracy are also provided. We also present the required CPU times for solving the variational equations. From these results, it is clear that the computational performance of the SIs for the 2D DKG system at $e_r \approx 10^{-5}$ is similar to what was reported in Section 3.4.1 for the 1D DKG model.

3.5 Summary

In this chapter we presented some numerical techniques for investigating the dynamics of 1D and 2D disordered Hamiltonian systems. We discussed theoretical aspects of the dynamics of deviation vectors, their distribution and the variational equations. We also defined the LCEs which are the most widely used measures of chaoticity. In Section 3.3, we described some existing integrators and through composition techniques, we constructed some higher order SIs. We then showed the effect of the nature of a deviation vector on computation of dynamical quantities like the finite time mLCE $\Lambda(t)$ (3.11) and $P^D(t)$ (3.3). In particular, we saw that an initial deviation vector whose non-zero coordinates just cover the region of the initially excited sites gives the fastest convergence of $\Lambda(t)$ to it's asymptotic evolution. That is to say, an initial deviation vector where $\frac{P(0)}{P^D(0)} \lesssim 1$.
We have also analysed in detail the computational performance of a number of symmetric SIs of even orders ranging from two up to eight. For each of these SIs we integrated the equations of motion and the corresponding variational equations (3.9) of the 1D (2.19) and the 2D (2.22) DKG models. We performed extensive numerical simulations for 35 different SIs as we used all of them to reproduce the dynamics of the two models for several initial excitations. We monitored the evolution of the energy and it's distribution focussing our investigation on cases with the absolute relative energy error $e_r(t) \lesssim 10^{-5}$ for the two models and $e_r(t) \lesssim 10^{-8}$ for the 1D DKG system. We followed the evolution of two characteristics $m_2(t)$ and $P(t)$ of the energy distribution together with $\Lambda(t)$ computed by each one of these SIs. From our results, we see that the performance of the SIs that were considered is independent of the initial excitations as we consistently get the same ranking in terms of exhibited efficiency by the SIs for the different excitations. Secondly the performance is independent of the spatial dimensions of the model being investigated, as the rank in performance for both the 1D and 2D DKG models is the same. For both 1D and 2D DKG models, the order four SIs $ABA864$ and $ABAH864$, the order six SIs $SABA_2Y6$, $s9SABA_26$ and $ABA864Y6$, exhibited the best performance at an absolute relative energy error $e_r \approx 10^{-5}$ with $ABA864$ [Blanes et al. (2013)] requiring the least CPU time for both models. Therefore our numerical computations involving the 1D and 2D DKG systems in the next chapters are performed using the $ABA864$ SI over other integrators like the popular Runge-Kutta class of integrators or the $SABA$ family [Laskar and Robutel (2001)] which have been used to study similar Hamiltonian systems [Flach et al. (2009a); Skokos et al. (2009); Skokos and Flach (2010); Laptyeva et al. (2010); Bodyfelt et al. (2011b); Laptyeva et al. (2012)].

A number of order six and order eight SIs that we considered required a relatively large time step τ to realise the approximate relative energy error $e_r \approx 10^{-5}$ but, because of the size of τ, they could not keep the absolute relative energy error $e_r(t)$ constant at this level of accuracy. However, even at higher accuracy of say $e_r \approx 10^{-7}$ some of these SIs gave a better performance compared to a few others that were stable at $e_r \approx 10^{-5}$, but they did not feature amongst the top most SIs. These higher order SIs have been found to stabilise at smaller values of τ, and thus give higher accuracy of energy conservation in computations. For example, for $e_r \approx 10^{-8}$ the best performing schemes have been found to be the order six SIs $s11ABA82\_6$, $SABA_2Y6$ and $s9ABA82\_6$ and the order eight SIs $s15ABA82\_8$ and $s19ABA82\_8$, with $s11ABA82\_6$ requiring the least CPU times for the integrations of the 1D DKG model.

Chapter 4

Chaotic behaviour of the 1D DKG model

In this chapter we investigate the chaotic dynamics of the 1D DKG model (2.19), extending some previous investigations on this topic for example by Gkolias (2013) and Skokos et al. (2013). We present our work as follows: In Section 4.1 we highlight the numerical techniques used for our computations. In Section 4.2 we give a theoretical account of choaticity and spreading theories. We then present our findings for the different classifications of chaotic dynamical behaviours, namely the weak chaos spreading regime in Section 4.4, strong chaos case in Section 4.5 and selftrapping behaviour in Section 4.6. Lastly, in Section 4.7 we discuss and summarize our findings. Parts of the results presented in Sections 4.4 and 4.5 of this chapter have also been reported in Senyange et al. (2018).

4.1 Numerical techniques

As part of the numerical techniques, we pay close attention to the integration method we use for our simulations and data analysis, the specifications of the computational facility to use, the programming software including compilers, the lattice size and other statistical analysis techniques.

4.1.1 Integration method

Integrating the equations of motion (3.5) for the 1D DKG system (2.19) as well as the variational equations (3.9), involves implementing the ABA864 [Blanes et al. (2013)] integrator, which is a two-part split order four SI whose computational efficiency has been shown in Chapter 3 to be relatively high compared to other integrators. More specifically we apply the TM method [Section 3.3.2; Skokos and Gerlach (2010); Gerlach and Skokos (2011); Gerlach et al. (2012)] to integrate the variational equations, and thus utilise equations (3.25). In our simulations, the relative energy error

$$e_r(t) = \frac{|H_{1K}(t) - H_{1K}(0)|}{H_{1K}(0)} \tag{4.1}$$

of the integration is kept at $e_r(t) \approx 10^{-5}$ by using time steps $\tau \approx 0.2 - 0.5$. Furthermore, in our study we use initial deviation vectors of the form $\mathbf{2}$ [Section 3.4.1, Figure 3.1**(b)**] where only the position and momentum coordinates of $20 - 350$ central sites are non-zero.

4.1.2 Practical computational consideration

Like it was mentioned in Section 3.4, the numerical computations were done using a facility with specifications Intel Xeon E5−2623, 3.00 GHz working in FORTRAN 90 programming language with compilers Intel Fortran (ifort) and GCC gfortran at optimization level 2 (-O2). We also used the Open Multi-Processing (OPENMP) parallelization application programming interface allocating on average 4−6 threads (CPU-cores) for each simulation. This was made possible after eliminating data dependencies in the program sections where the parallelisation directives were implemented and thus the computational efficiency (i.e. CPU time) was improved by an approximate factor of 2.5.

4.1.3 Lattice size

Since in our investigation we want to study the asymptotic behaviour of initially localized energy excitations in theoretically infinite lattices we therefore perform simulations for very large but obviously finite chains. This setup however is computationally costly in terms of CPU time, storage space and computer processing memory. To counter these challenges, we use lattices whose length N increases with time (i.e. $N = N(t) \geq N(0)$) depending on the wave packet extent taking special care in avoiding boundary effects. To do so, we start with a relatively small lattice of size $N(0)$ and increase it whenever either the wave packet or the deviation vector distribution gets close to the boundary sites. We check that in the following way: for each site l located within the boundary strip of width N_W, we ensure that the site energy

$$h_l = \frac{p_l^2}{2} + \frac{\tilde{\epsilon}_l q_l^2}{2} + \frac{(q_{l-1} - q_l)^2 + (q_{l+1} - q_l)^2}{4W} + \frac{q_l^4}{4}, \tag{4.2}$$

and the square norm component $\delta q_l^2 + \delta p_l^2$ of the deviation vector at this site are always less than 10^{-8}. That is to say, for all $l \in [1, N_W] \cup [N - N_W + 1, N]$

$$\max_l\{h_l\} < 10^{-8} \qquad \text{and} \qquad \max_l\{\delta q_l^2 + \delta p_l^2\} < 10^{-8}. \tag{4.3}$$

We note that this restriction on the deviation vector ensures that its dynamics is not affected by finite lattice size effects thereby ensuring that any deductions made using the vector are reliable. In case criteria (4.3) are violated, the lattice size is then increased by a width dependant on the disorder strength W in order to increase the lattice size so that the wave packet will continue spreading without the boundary sites affecting the dynamics. We use N_W with values inversely proportional to W since the spatial extent (estimated for example by the localization volume) of the NMs increases with a decrease in W as noted in Chapter 2 and Krimer and Flach (2010).

4.1.4 Numerical estimation of slopes

In our study, we numerically compute quantities for many different disorder realizations over which we average the obtained results. For cases where we are interested in the power law description of the dependence of such a quantity (let us generally denote it by Q) usually on time t, we numerically estimate a slope of the average curve to find this law. This is done as follows: From the averaged data we compute a smooth curve using the robust locally weighted regression (LOESS) algorithm [Cleveland (1979); Cleveland and Devlin (1988); Laptyeva et al. (2010); Gkolias (2013)]. In this process, we smoothen points' trend using linear locally weighted regression, the weight function

$$W(x) = \begin{cases} (1 - |x|^3)^3 & \text{for} \quad |x| < 1 \\ 0 & \text{for} \quad |x| \geq 1, \end{cases}$$

a single iteration of the robust fitting procedure and smoothening proportion 0.1 [Cleveland (1979)]. We then use the central finite difference calculation described in Laptyeva et al. (2010), Bodyfelt et al. (2011b) and Gkolias (2013) to determine the local derivative $\alpha_Q(t) = dQ/dt$ of quantity Q with respect to (usually time) t. For cases where we compute the error in the power law exponent (using say error bars), we first compute the local derivative from each data realization and then average it over all realizations.

4.2 Chaoticity and energy spreading theories

We now give a theoretical description of a comparison between chaoticity and the wave packet extent. As mentioned before in Chapter 3, chaoticity can be quantified using the finite time mLCE $\Lambda(t)$ (3.11). Therefore, the chaoticity time scale $T_\Lambda(t)$ (usually referred to as Lyapunov time), defined as

$$T_\Lambda(t) \sim \frac{1}{\Lambda(t)} \tag{4.4}$$

[Skokos and Gerlach (2010)], estimates the time a system takes to become chaotic. Knowing that $\Lambda(t) \propto t^{\alpha_\Lambda}$, equation (4.4) becomes

$$T_\Lambda(t) \sim t^{-\alpha_\Lambda}. \tag{4.5}$$

Wave packet extent on the other hand can be estimated using the second moment m_2 [(2.30) for 1D and (2.34) for the 2D models] and participation number P [(2.31) for 1D and (2.35) for the 2D models]. We therefore define wave packet characteristic spreading time scales based on m_2 and P as follows: The diffusion coefficient D, which is related to the second moment as

$$m_2(t) \sim Dt, \tag{4.6}$$

defines a spreading time scale T_{m_2}

$$T_{m_2}(t) \sim \frac{1}{D}. \tag{4.7}$$

Equations (4.6) and (4.7) give

$$T_{m_2}(t) \sim t^{1-\alpha_{m_2}} \tag{4.8}$$

where $m_2(t) \propto t^{\alpha_{m_2}}$.
Secondly, the spreading time scale [we denote by T_P] can be interpreted as the time taken for a marginal change in the wave packet participation number P. Therefore,

$$T_P(t) \sim \frac{1}{\dot{P}}, \tag{4.9}$$

where $\dot{P}$ denotes the derivative of P. For the selftrapping regime where the number P of highly excited sites is practically constant, T_p is infinite. Since $P(t) \propto t^{\alpha_P}$, then

$$T_P(t) \sim t^{1-\alpha_P}. \tag{4.10}$$

Using equations (4.5), (4.8) and (4.10) we get the spreading to chaoticity time scale ratios

$$R_{m_2} := \frac{T_{m_2}}{T_\Lambda} \sim t^{1+\alpha_\Lambda-\alpha_{m_2}}, \qquad R_P := \frac{T_P}{T_\Lambda} \sim t^{1+\alpha_\Lambda-\alpha_P}. \tag{4.11}$$

From the ratios (4.11), we can compare the rates of wave packet's chaotization and extent of subdiffusive spreading.

4.3 Procedure for numerical simulations

In our numerical simulations, we give the system of N sites a total energy H_{1K} (2.19) by initially exciting a block of L central sites of the lattice with each site getting the same energy $h = h_l = H_{1K}(0)/L$ by setting $p_l = \pm\sqrt{2h}$, where the signs are assigned randomly and $p_l = 0$ for all other sites. The displacements q_l of the lattice are all set to 0. In all cases of the simulations, we imposed conditions $p_0 = p_{N+1} = q_0 = q_{N+1} = 0$.
We follow the evolution of several ICs for various disorder realizations of the system (2.19) where for each setup we obtain statistical results for the time evolution of a dynamical quantity, say Q, by averaging its values over 200 different disorder realizations to get $\langle Q \rangle$, where $\langle \cdot \rangle$ denotes the average. We then extract the rate of change of Q (derivative of Q) to get

$$\alpha_{_Q}(t) = \frac{d\langle Q \rangle}{dt} = \left\langle \frac{dQ}{dt} \right\rangle. \tag{4.12}$$

An almost constant value of $\alpha_{_Q}(t)$ indicates the existence of a linear dependence $Q(t) \propto \alpha_{_Q} t$ of Q on t. If the fitting is done for the logarithms of Q and t (as repeatedly happens in our studies) then implementing the procedure we just discussed we obtain a slope

$$\alpha'_{_Q} = \frac{d\langle \log Q \rangle}{d(\log t)}. \tag{4.13}$$

The practical constancy of $\alpha'_{_Q}$ indicates a power law dependence $Q(t) \propto t^{\alpha_Q}$ of Q on t.

4.4 The weak chaos regime

We generally perform numerical integration of the system (2.19) for time not exceeding $t_f \approx 10^9$ time units. The lattice size $N(t)$ was increased up to a maximum $N(t_f) \approx 700 - 1\,500$ thereby ensuring no energy at the boundary sites. The energy H_{1K} of the system was conserved at an absolute relative energy error (4.1) $e_r(t) \approx 10^{-5}$ for time steps $\tau \approx 0.4 - 0.6$. We investigate the chaotic behaviour of the system (2.19) by considering the following four parameter cases where each of L central lattice sites is excited with energy h (2.28) with disorder strength W.
Case $W1_1$**:** $W = 3$, $L = 37$, $h = 0.01$;
Case $W2_1$**:** $W = 4$, $L = 1$, $h = 0.4$;
Case $W3_1$**:** $W = 4$, $L = 21$, $h = 0.01$;
Case $W4_1$**:** $W = 5$, $L = 13$, $h = 0.02$.
These are representative cases of various W values and initial excitation lengths. The cases $W1_1$, $W2_1$ and $W3_1$ were also considered in Skokos et al. (2013) and Gkolias (2013) and respectively named cases III, I and II while case $W4_1$ is a new one. In that work, a total of 50 disorder realizations were analysed in each of the cases. In our study, we perform an analysis for 200 realizations in each of the four cases $W1_1$, $W2_1$, $W3_1$ and $W4_1$, thereby improving the statistical reliability of our findings. We also analyse the dynamics in more depth by studying observables for the deviation vector and it's distribution.
Figure 4.1 shows results for the time evolution of the second moment $m_2(t)$ (2.30) and the participation number $P(t)$ (2.31). Panels **(a)** and **(b)** respectively show the evolution of $m_2(t)$ and $P(t)$ for the cases $W1_1$ (red curves), $W2_1$ (blue curves), $W3_1$ (greens) and $W4_1$ (brown curves). In panels **(c)** and **(d)** we present slopes $\alpha_{m_2}(t)$ of $m_2(t)$ and $\alpha_P(t)$ of $P(t)$ respectively with the dashed lines indicating the values $\alpha_{m_2} = 0.34$ [panel **(c)**] and $\alpha_P = 0.17$ [panel **(d)**]. The error bars in **(c)** and **(d)** respectively denote the numerical error of one standard deviation in the computation of slopes $\alpha_{m_2}(t)$ and $\alpha_P(t)$.

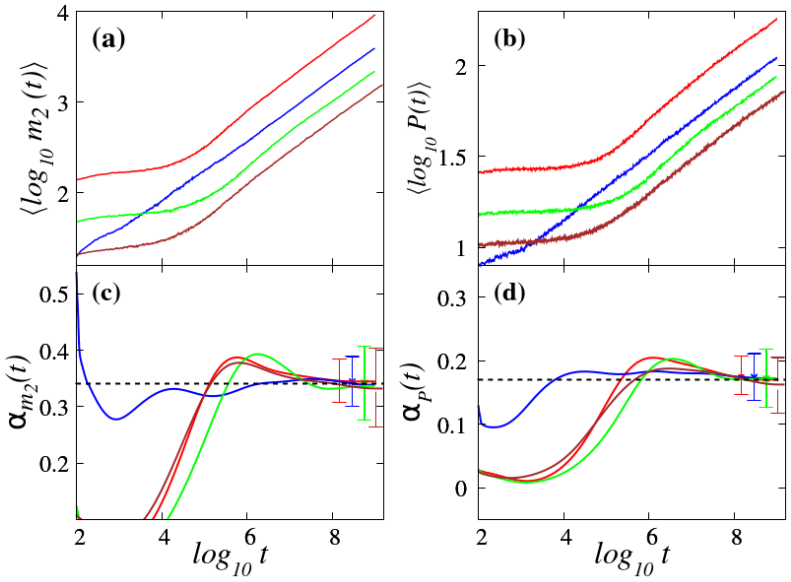

Figure 4.1: Results for the time evolution of **(a)** $m_2(t)$ (2.30), **(b)** $P(t)$ (2.31) and the corresponding slopes **(c)** $\alpha_{m_2}(t)$ for $m_2(t)$ **(d)** $\alpha_P(t)$ for $P(t)$ for the weak chaos cases $W1_1$ (red curves), $W2_1$ (blue curves), $W3_1$ (green curves) and $W4_1$ (brown curves) of Hamiltonian (2.19). The dashed lines in panels **(c)** and **(d)** respectively denote values $\alpha_{m_2} = 0.34$ and $\alpha_P = 0.17$. The error bars in **(c)** and **(d)** denote 1 standard deviation of the computed slopes. Plots **(a)** and **(b)** are in log-log scale while **(c)** and **(d)** are in log-linear scale.

These results verify that the cases considered show characteristics of the weak chaos spreading behaviour with $m_2(t)$ and $P(t)$ [panels **(a)** and **(b)** respectively] evolving as $m_2(t) \propto t^{0.34}$ [panel **(c)**], $P(t) \propto t^{0.17}$ [panel **(d)**] which is in accordance with theoretical estimates discussed in Section 2.3.3 and already established results of Flach et al. (2009b), Skokos et al. (2009), Laptyeva et al. (2010), Flach (2010) and Bodyfelt et al. (2011b) which emphasize that $m_2(t) \propto t^{1/3}$ and $P(t) \propto t^{1/6}$. More specifically, the theoretical predictions for the power law exponents lie within an interval, centred around our numerically computed values and of width of one standard deviation.

We now discuss findings for the chaoticity of the model. For each of the four weak chaos cases we investigated, we compute the time evolution of $\Lambda(t)$ (3.11) and present the results in Figure 4.2. The average of $\Lambda(t)$ over 200 disorder realizations is shown in Figure 4.2**(a)**. In the panels **(b)**-**(e)**, we plot the corresponding numerically computed slopes (4.13) of the curves in panel **(a)** together with an error (colour shading) defined by one standard deviation of the computed slopes α_Λ. The horizontal dashed lines in **(b)**-**(e)** denote the value $\alpha_\Lambda = -0.25$. The results of Figure 4.2 **(b)**-**(e)** indicate that for each weak chaos case considered, the time evolution of $\Lambda(t)$ converges towards the power law $\Lambda(t) \propto t^{-0.25}$. In this case, the lighter colour shade or clouds correspond to one standard deviation of the computed slopes. This result was also reported by Skokos et al. (2013) and Gkolias (2013) where the cases $W1_1$, $W2_1$ and $W3_1$ were studied and $\Lambda(t)$ evolved following the power law $\Lambda(t) \propto t^{-0.25}$. The additional case, $W4_1$, we have included in our analysis also complies with the power law decay of $\Lambda(t)$. Clearly α_Λ is different from the value -1 [Benettin et al. (1976); Skokos (2010)] of regular dynamical behaviour, thereby our findings reveal that the dynamics of the 1D DKG model in the weak chaos regime shows no tendencies of relaxing into regular behaviour. This result was also observed and discussed in Skokos et al. (2013).

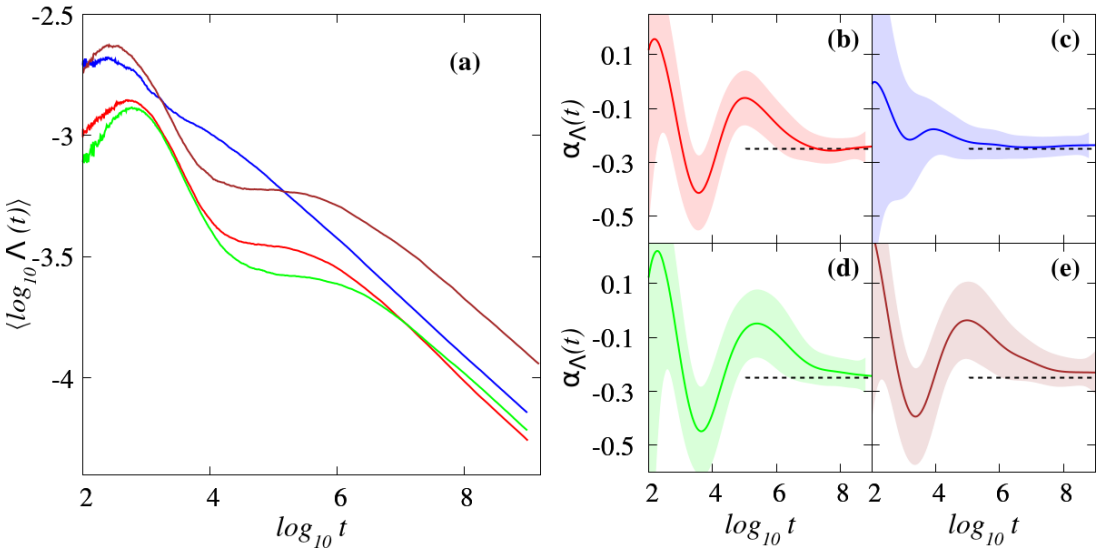

Figure 4.2: Results for **(a)** the time evolution of the finite time mLCE $\Lambda(t)$ (3.11) and **(b)**-**(d)** the corresponding numerically computed slopes for the four weak chaos cases of the 1D DKG system (2.19) described at the beginning of Section 4.4. Results are averaged over 200 disorder realizations. The curve colours correspond to the cases presented in Figure 4.1. The straight dashed lines in **(b)** - **(e)** indicate the value $\alpha_\Lambda = -0.25$. Panel **(a)** is in log-log scale while panels **(b)**-**(d)** are in log-linear scale.

Using our numerical findings, the spreading to chaoticity time scale ratios R_{m_2} and R_P of (4.11) give

$$R_{m_2} \sim t^{0.41}, \quad R_P \sim t^{0.58},$$

where $\alpha_{m_2} = 0.34$, $\alpha_P = 0.17$ and $\alpha_\Lambda = -0.25$. Thus the spreading time scales T_{m_2} and T_P remain always larger than the chaoticity time scale T_Λ, which implies that wave packet gets more chaotic at a rate faster than its spreading.

Deviation vector distributions

In order to further analyse the chaos behaviour of the 1D DKG (2.19) model, we investigate the time evolution of the deviation vectors (3.1) and their distributions (3.2). As a measure of the separation of trajectories, the deviation vector $\mathbf{w}(t)$ (3.1) (on which the finite time mLCE depends) eventually aligns to the most unstable direction in the system's phase space. Therefore large ξ_l^D (3.2) values of the DVD indicate at which lattice sites the sensitive dependence on initial conditions is higher. It is for this reason that such distributions were used in Skokos et al. (2013) to visualize the motion of chaotic seeds (degrees of freedom exhibiting more chaos) inside the spreading wave packet. Utilisations of the DVD in a similar manner were also reported in Ngapasare et al. (2019). In Figure 4.3 we present the evolution of the **(a)** energy density $\xi_l(t)$ (4.2) and **(b)** DVD $\xi^D(t)$ (3.2) for a representative realisation belonging to case $W1_1$. The centre of the lattice has been translated to 0. In Figure 4.3**(c)** and **(d)** we present snapshots of these distributions taken at the instances corresponding to the times indicated by the horizontal dashed lines of Figure 4.3**(a)**, **(b)** using matching colours.
From the results of Figure 4.3 we see that the energy density continuously extends to cover a wider region of the chain. This spreading is done more or less symmetrically around the position where the initial excitation takes place as the evolution of the distributions' centre [white curve in Figure 4.3**(a)**] is rather smooth and always remains close to the middle of the lattice. On the other hand, the DVD [panel **(b)**] always stays inside the excited part of the lattice as seen in panel **(a)** where the lattice section traversed by the

DVD lies within the portion covered by the energy distribution. The DVDs also retain a more localised, pointy shape as observed in panel **(d)**.

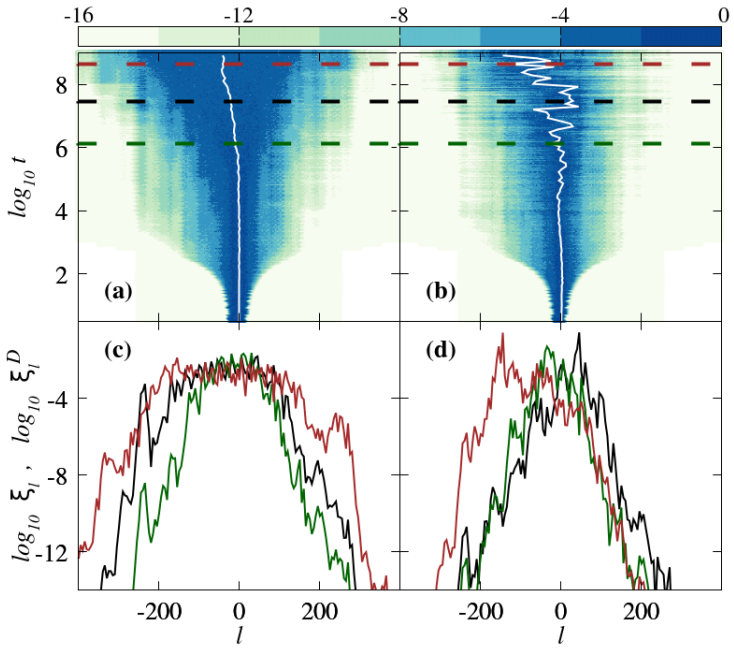

Figure 4.3: Results for the time evolution of **(a)** the normalized energy distribution $\xi_l(t)$ (4.2) and **(b)** the corresponding DVD $\xi_l^D(t)$ (3.2) of case $W1_1$. The colour scales at the top of the figure are used for colouring lattice sites according to their **(a)** $\log_{10}\xi_l(t)$ and **(b)** $\log_{10}\xi_l^D(t)$ values. In both panels a white curve traces the distributions' centre. **(c)** Normalized energy distributions $\xi_l(t)$ and **(d)** DVDs at times $\log_{10} t = 6.14$ [green curves], $\log_{10} t = 7.47$ [black curves], $\log_{10} t = 8.65$ [red curves]. These times are also denoted by similarly coloured horizontal dashed lines in **(a)** and **(b)**.

The DVDs are initially located in the region of the initial excitation and later start moving around widely after $\log_{10} t \approx 6$, as clearly depicted in the time evolution of each DVD's mean position $\bar{l}_w = \sum_l l\xi_l^D$ [white curve in Figure 4.3**(b)**], as $\bar{l}_w$ randomly fluctuates with increasing amplitude. The authors of Skokos et al. (2013) based on such observations and represented the random motion of deterministic chaos seeds inside the wave packet using DVDs. These random oscillations of the chaotic seeds are essential in homogenizing chaos inside the wave packet, leading in this way to the thermalization and subdiffusive spreading of the wave packet.

As the wave packet spreads [Figure 4.3 **(c)**], the (constant) total energy is shared among more degrees of freedom as additional lattice sites are excited. Therefore the energy density of the excited sites (i.e. the effective nonlinearity strength of the system) decreases. Also, the system's chaoticity reduces in time since the value of $\Lambda(t)$ [Figure 4.2 **(a)**] follows a power law decay.

We now generalise the findings of Figure 4.3 on DVDs beyond the single realisation reported, by computing some characteristics of the distribution. We compute the DVD second moment $m_2^D(t)$ and participation number $P^D(t)$. The obtained average results are presented in Figure 4.4. The DVDs' second moment $m_2^D(t)$ [Figure 4.4**(a)**] shows an asymptotic, slow growth, reaching values which are always smaller than the wave packets' $m_2(t)$ [Figure 4.1**(a)**] by at least one order of magnitude. This slow growth is characterised by the power law $m_2^D(t) \propto t^{0.1}$ indicated by the computed derivatives $\alpha_{m_2^D}(t)$ of $m_2^D(t)$ in Figure 4.4**(c)** where the horizontal dashed line corresponds to the value $\alpha_{m_2^D}(t) = 0.1$. The fact that the DVDs of Figure 4.3**(d)** remain practically localized with a narrow,

pointy shape is reflected in the small and almost constant P^D values [Figure 4.4**(b)** and **(d)**].

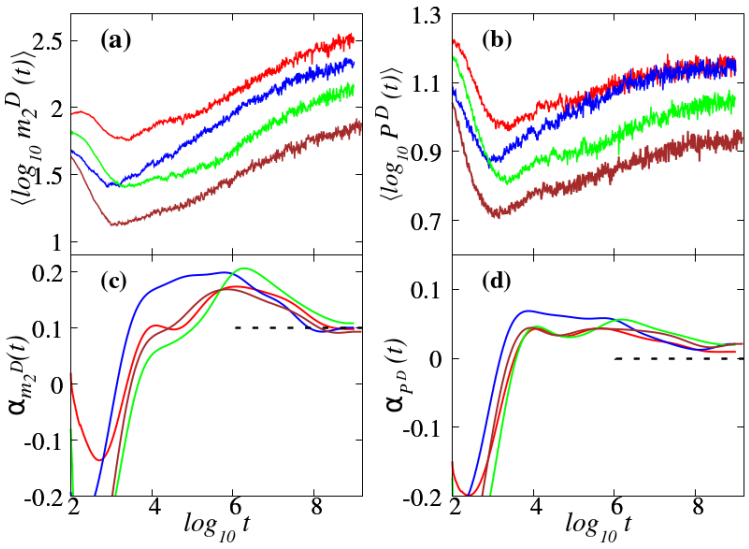

Figure 4.4: Results averaged over realizations for the time evolution of **(a)** $m_2^D(t)$ (2.30), **(b)** $P^D(t)$ (2.31), the corresponding slopes **(c)** $\alpha_{m_2^D}(t)$ for m_2^D and **(d)** $\alpha_{P^D}(t)$ for P^D for the cases $W1_1$ - $W4_1$. The dashed lines in panels **(c)** and **(d)** respectively indicate values $\alpha_{m_2^D}(t) = 0.1$ and $\alpha_{P^D}(t) = 0$. The curve colours correspond to the cases presented in Figure 4.1. Panels **(a)** and **(b)** are in log-log scale while **(c)**, and **(d)** are in log-linear scale.

Their participation number P^D attains small values, $P^D \gtrsim 8$ (the lowest value being $P^D \approx 8$ for case $W4_1$ [brown curves in Figure 4.4 **(b)**]), showing a tendency to asymptotically saturate to a constant number, since all curves of Figure 4.4**(b)** show signs of an eventual level off. This is confirmed by the computation of the slopes in Figure 4.4**(d)** of $P^D(t)$ which show a tendency to settle at values close to $\alpha_{P^D} = 0$ [horizontal dashed line in Figure 4.4 **(d)**].
We note that the localized DVD [Figure 4.3**(b)** and **(d)**] meanders over a significantly large region of the lattice compared to the energy distribution [Figure 4.3**(a)** and **(c)**] whose mean position is more or less fixed at a specific degree of freedom. In order to quantify the width of the lattice region effectively covered by the DVD, we follow the time evolution of the following three numerical quantities. Based on the mean position $\bar{l}_w(t)$ of the DVD (3.2) at time t we monitor the evolution of

$$M(t) = \max_{t \in \Delta} \left\{ ||l_\Delta - \bar{l}_w(t)|| \right\}, \tag{4.14}$$

where

$$l_\Delta = \frac{1}{|\Delta|} \sum_{t \in \Delta} \bar{l}_w(t)$$

with Δ being a time window of fixed width $|\Delta|$. $M(t)$ gives us an idea about the mean deviation of the DVD centre due to the dynamical evolution within a certain epoch in time. In other words, M gives the maximum of the absolute deviation of the elements of $\{\bar{l}_w(t)\}$ from their average in a time interval Δ.
A second measure we denote by $R(t)$ is defined as

$$R(t) = \max_{0 \le t_1 \le t_2 \le t} \left\{ ||\bar{l}_w(t_1) - \bar{l}_w(t_2)|| \right\}, \tag{4.15}$$

where ||.|| denotes the Euclidean norm. $R(t)$ gives the largest separation between any two mean positions of the distribution at or before time t. $R(t)$ in the case of the 1D lattice considered here is equivalent to

$$R(t) = \max_{0\leq t_1\leq t}\{\bar{l}_w(t_1)\} - \min_{0\leq t_2\leq t}\{\bar{l}_w(t_2)\}.$$

The quantity

$$\iota^D(t) = \sum_t ||\bar{l}_w(t) - \bar{l}_w(t-\tau)||, \tag{4.16}$$

estimates the magnitude of the total displacement of the DVD centre. $\bar{l}_w(t-\tau)$ is the mean position of the distribution, a time τ before the mean position $\bar{l}_w(t)$. From the evolution of the white curves showing the mean positions of the energy distribution [Figure 4.4 **(a)**] and DVD [Figure 4.4 **(b)**] we see that the DVD centre travels more distance compared to the energy centre and so the value of ι^D is expected to be larger for the DVD.
These three quantities inform us on the dynamics of the deviation vector in different ways. R estimates the extent (amplitude of fluctuations of the distribution centre) to which the DVD spreads in the lattice, ι^D the total distance covered by the distribution centre as it meanders in the lattice while M gives the same information as R but for short intervals of time during the evolution. We therefore expect that at any integration time t

$$M(t) \leq R(t) \leq \iota^D(t). \tag{4.17}$$

Figure 4.5 shows results obtained for the evolution of quantities $M(t)$ (4.14) [panel **(a)**], $R(t)$ (4.15) [panel **(b)**] and $\iota^D(t)$ (4.16) [panel**(c)**] where the dashed lines guide the eye for slopes 0.24 in **(a)**, 0.25 in **(b)** and 0.28 in **(c)**. Since the wave packet continuously spreads, the localized chaotic seeds, which are constantly meandering inside it, cover larger lattice regions as time increases.

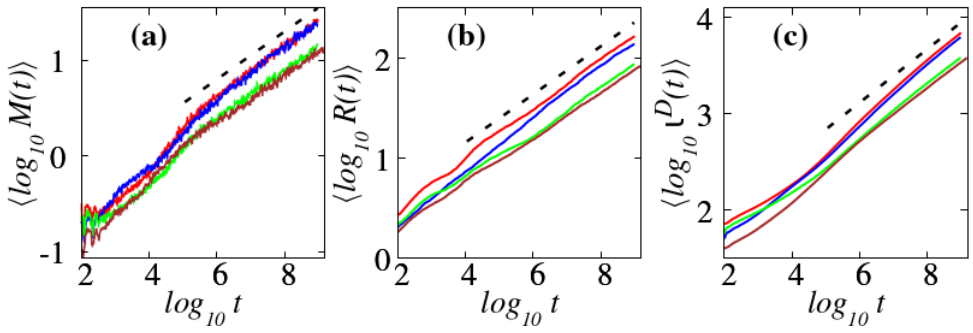

Figure 4.5: Results for the time evolution of **(a)** $M(t)$ (4.14), **(b)** $R(t)$ (4.15) and **(c)** $\iota^D(t)$ (4.16) of the DVD for cases $W1_1$ - $W4_1$ of Hamiltonian (2.19). The curve colours correspond to the cases presented in Figure 4.1. The straight dashed lines show slopes **(a)** 0.24, **(b)** 0.25 and **(c)** 0.28. Panels **(a)**, **(b)** and **(c)** are in log-log scale.

This is evident by the continuously increasing values of $M(t)$ [Figure 4.5**(a)**], $R(t)$ [Figure 4.5**(b)**] and $\iota^D(t)$ [Figure 4.5**(c)**]. This increase is very well described, for all three measures, by the power laws $R(t) \propto t^{0.24}$ [Figure 4.5**(a)**], $\iota^D(t) \propto t^{0.25}$ [Figure 4.5**(b)**] and $M(t) \propto t^{0.28}$ [Figure 4.5**(c)**].

4.5 The strong chaos regime

We now turn our attention to the chaotic behaviour of energy spreading in the strong chaos regime that was predicted in Section 2.3.3; a study which was not considered in

Skokos et al. (2013). As was explained in Laptyeva et al. (2010), Flach (2010) and Bodyfelt et al. (2011b), the strong chaos subdiffusive regime is only possible when more than one site is initially excited. The wave packet spreading in the initial phase for this regime is faster than in the weak chaos regime with the wave packet spreading as $m_2(t) \propto t^{1/2}$ and $P(t) \propto t^{1/4}$ compared to the $m_2(t) \propto t^{1/3}$ and $P(t) \propto t^{1/6}$ behaviour observed for the weak chaos. This initial phase is followed by a subsequent slowing down of energy propagation, which asymptotically tends to the weak chaos behaviour.
In our study we consider the following four cases that belong to the strong chaos regime:
Case $S1_1$**:** $W = 1$, $L = 330$, $h = 0.1$;
Case $S2_1$**:** $W = 2$, $L = 83$, $h = 0.1$;
Case $S3_1$**:** $W = 3$, $L = 37$, $h = 0.1$;
Case $S4_1$**:** $W = 3$, $L = 83$, $h = 0.1$,
The cases $S1_1$, $S3_1$ and $S4_1$ were also considered in Gkolias (2013) where they were named respectively as cases III, II and I while case $S2_1$ is a new one. For all these cases, we perform investigations based on numerical integrations up to a final time $t_f \approx 10^{8.2}$ (i.e. $t_f \approx$ 150,000,000) time units. The lattice size $N(t)$ is gradually increased to prevent the boundary sites from interfering with the dynamics of the system. In particular, in our strong chaos simulations we use lattices whose size increases up to a maximum $N(t_f) \approx 2\,500 - 23\,000$. The time steps $\tau \approx 0.25 - 0.35$ used conserved the energy H_{1K} of the system at absolute relative energy error $e_r(t)$ (4.1) at the level of 10^{-5}.
In Figure 4.6 we present the time evolution of the measures of wave packet extent, namely the second moment $m_2(t)$ (2.30) and participation number $P(t)$ (2.31). We see clear power law growths $m_2(t) \propto t^{\alpha_{m_2}}$ and $P(t) \propto t^{\alpha_P}$ of these two quantities.

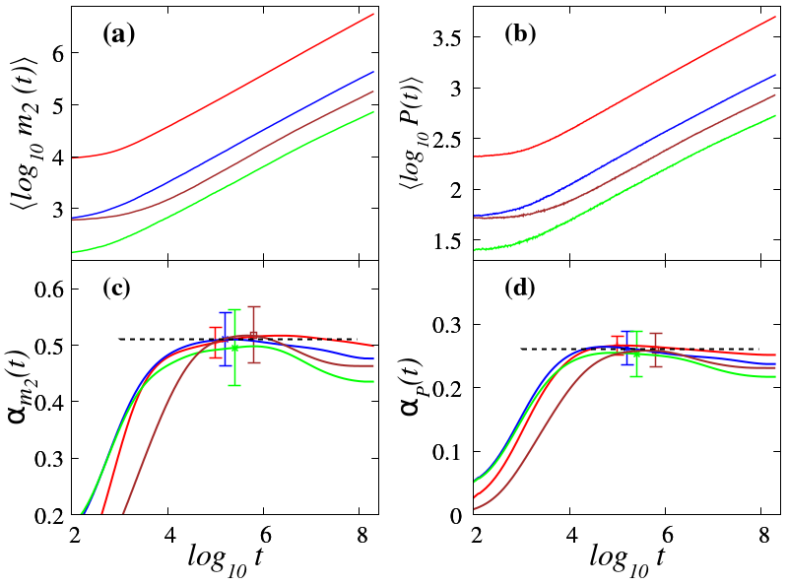

Figure 4.6: Similar to Figure 4.2 but for the strong chaos spreading regime of Hamiltonian (2.19). Results for the time evolution of **(a)** $m_2(t)$ (2.30), **(b)** $P(t)$ (2.31), the corresponding slopes **(c)** $\alpha_{m_2}(t)$ for m_2 and **(d)** $\alpha_P(t)$ for $P(t)$ for the cases $S1_1$ (red curves), $S2_1$ (blue curves), $S3_1$ (green curves) and $S4_1$ (brown curves). The dashed lines in panels **(c)** and **(d)** respectively indicate values $\alpha_{m_2} = 0.5$ and $\alpha_P = 0.26$. The error bars in **(c)** and **(d)** denote the numerical error of one standard deviation in the computed slopes [**(c)** and **(d)**]. Plots **(a)** and **(b)** are in log-log scale while **(c)** and **(d)** are in log-linear scale.

The computed values of α_{m_2} and α_P are respectively shown by straight dashed lines shown in Figure 4.6**(c)** and **(d)** are $\alpha_{m_2} = 0.5$ and $\alpha_P = 0.26$ and persist for about 2

decades of integration time. This epoch is generally followed by a mild slowing down of the spreading process for $\log_{10} t \gtrsim 6$ in accordance with results shown in Laptyeva et al. (2010) and Bodyfelt et al. (2011a). The error bars in **(c)** and **(d)** denote a standard deviation of m_2 and P slopes. The findings show that all these cases belong to the strong chaos regime since the theoretical estimates $\alpha_{m_2} = 0.5$, is equal to the numerically computed result, and $\alpha_P = 0.25$ is within a standard deviation of the numerically computed slope ($\alpha_P = 0.26$) [panels**(c)** and **(d)**] where the computed values $\alpha_{m_2} = 0.5$ and $\alpha_P = 0.26$ for about 2 decades of integration time. We note that for the weak chaos cases the wave packet effectively covers approximately 800 sites by $t_f = 10^9$ compared to approximately 1 800 sites by $t_f = 10^{8.2}$ in the strong chaos case as estimated using P.
We now elaborate on the chaoticity in the strong chaos regime: Figure 4.7 shows results for the evolution of the finite time mLCE $\Lambda(t)$ (3.11). We observe a power law decay $\Lambda(t) \propto t^{\alpha_\Lambda}$, with no tendency of slowing down to the regular dynamics law $\Lambda(t) \propto t^{-1}$, similar to the chaotic tendency seen in the weak chaos cases. The difference is that for strong chaos $\alpha_\Lambda \approx -0.32$ while for weak chaos $\alpha_\Lambda \approx -0.25$. The difference in the values of α_Λ for the strong and weak chaos regimes is an additional indication of the differences in the dynamical behaviour for these two regimes. As the strong chaos regime is a transient one, the evolution of $m_2(t)$ and $P(t)$ show signs of the crossover to the weak chaos dynamics, as their increase becomes slower for $\log_{10} t \gtrsim 6$ (Figure 4.6). This happens because the values of $m_2(t)$ and $P(t)$ are determined by the current dynamical state of the wave packet. On the other hand, such changes are not well pronounced in the evolution of $\Lambda(t)$ (Figure 4.7). As the dynamics crosses over from the strong chaos behaviour characterized by $\alpha_\Lambda = -0.32$ to the asymptotic weak chaos behaviour associated with $\alpha_\Lambda = -0.25$, one would expect to see some change in the values of α_Λ (panels **(b)**-**(d)** of Figure 4.7) indicating this transition.

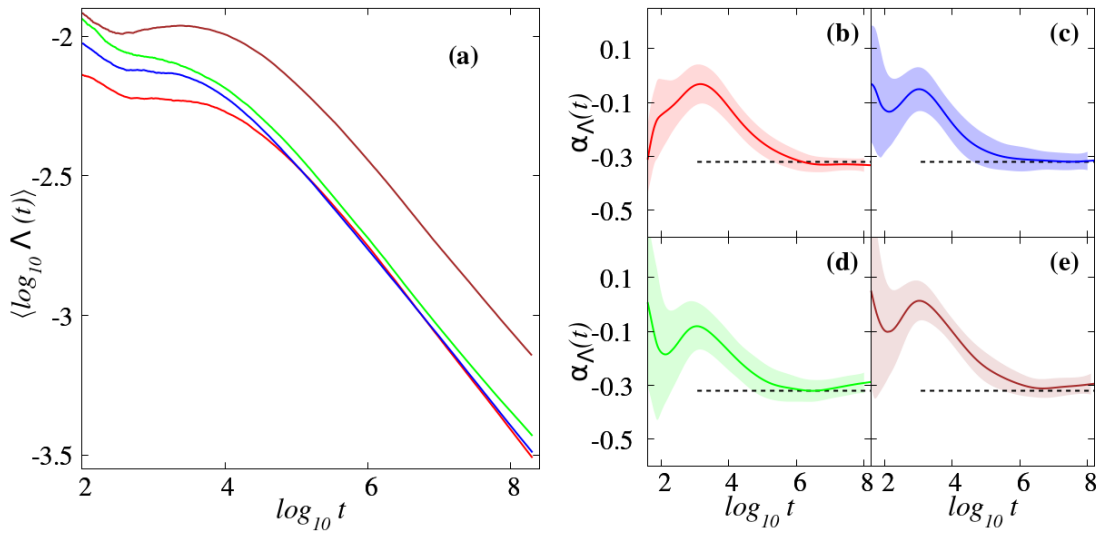

Figure 4.7: Similar to Figure 4.2 but for the strong chaos spreading regime of Hamiltonian (2.19). Results for the time evolution of **(a)** the finite time mLCE $\Lambda(t)$ (3.11) and **(b)**-**(e)** the corresponding derivatives for the strong chaos cases. The curve colours correspond to the cases presented in Figure 4.6. The straight dashed lines indicate slopes $\alpha_\Lambda = -0.32$. Panel **(a)** is in log-log scale while panels **(b)**-**(e)** are in log-linear scale.

Such changes are not observed because the value of Λ (3.11) is influenced by the whole evolution of the deviation vector [i.e. the ratio $||\boldsymbol{w}(t)||/||\boldsymbol{w}(0)||$ in (3.11)] and consequently, the whole history of the dynamics (which is predominately influenced by the strong chaos behaviour) and not by the current state of the systems. Thus, Λ is not sensitive to subtle

dynamical changes.
Using our numerical findings as shown in Figure 4.6 and Figure 4.7, the spreading to chaoticity time scale ratios R_{m_2} and R_P of (4.11) give

$$R_{m_2} \sim t^{0.18}, \quad R_P \sim t^{0.42},$$

since $\alpha_{m_2} = 0.5$, $\alpha_P = 0.26$ and $\alpha_\Lambda = -0.32$. The chaoticity time scale T_Λ therefore always remains smaller than the spreading time scales T_{m_2} and T_P. This means that, just like we observed for the weak chaos case, a wave packet gets more chaotic at a rate faster than its spreading.
We now investigate the DVD evolution for subtle changes that may not have been captured by m_2, P or Λ.

Deviation vector distributions

We use the deviation vectors to study the behaviour of chaotic seeds in this regime of strong chaos. In Figure 4.8**(a)** and **(b)** we respectively plot the time evolution of the energy density (4.2) and the corresponding DVD (3.2) for an individual set up of case $S3_1$, while snapshots of these distributions at some specific times are shown in Figure 4.8**(c)** and **(d)**. The centre of the lattice has been translated to 0.

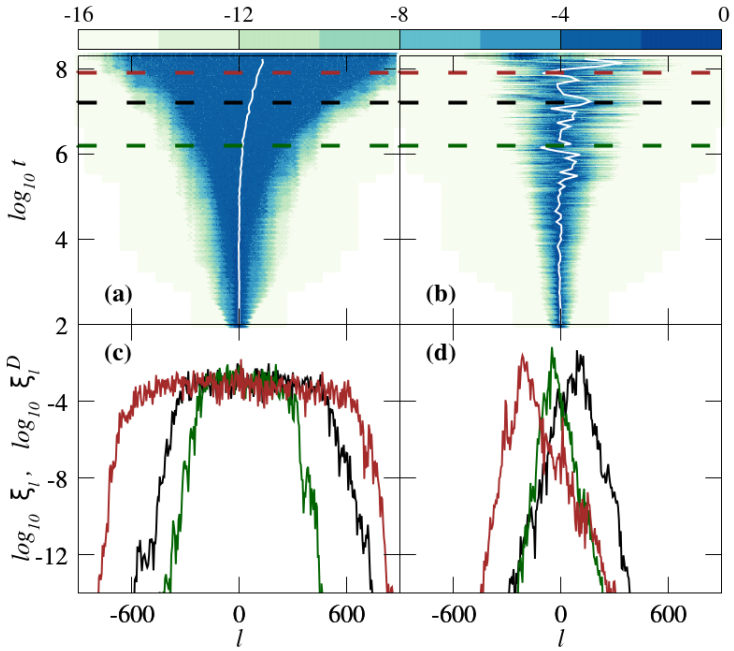

Figure 4.8: Similar to Figure 4.3 but for the strong chaos spreading regime case $S3_1$ of Hamiltonian (2.19). Results for the time evolution of **(a)** the normalized energy distribution $\xi_l(t)$ (4.2) and **(b)** the corresponding DVD $\xi_l^D(t)$ (3.2). The colour scales at the top of the figure are used for colouring lattice sites according to their **(a)** $\log_{10}\xi_l(t)$ and **(b)** $\log_{10}\xi_l^D(t)$ values. In each of the panels **(a)** and **(b)** the white curve traces the distributions' centre. **(c)** Normalized energy distributions $\xi_l(t)$ and **(d)** DVDs at times $\log_{10} t = 6.2$ [green curve], $\log_{10} t = 7.2$ [black curve], $\log_{10} t = 7.9$ [red curve]. These times are also denoted by similar coloured horizontal dashed lines in **(a)** and **(b)**.

As in the weak chaos cases presented in Figure 4.3, the energy density spreads smoothly and rather symmetrically around the lattice's centre [Figure 4.8**(a)**, **(c)**], reaching more distant sites from the centre compared to the weak chaos cases [Figure 4.3**(a)**, **(c)**].

This is because the strong chaos regime is characterized by a faster subdiffusive spreading compared to the weak chaos regime, which is reflected in the larger exponents in the power law increases of m_2 and P as presented in Figure 4.1 and Figure 4.6. On the other hand, the DVDs again remain localized, exhibiting fluctuations in their position, which appear earlier in time and have larger amplitudes [Figure 4.8**(b)**, **(d)**] with respect to the weak chaos case [Figure 4.3**(b)**, **(d)**].
The DVD second moment m_2^D (3.4) [shown in Figure 4.9**(a)**] for the strong chaos cases $S1_1$ - $S4_1$ increases in time attaining larger values compared to the weak chaos regime [presented in Figure 4.4**(a)**], although this increase does not show signs of a constant power law growth rate as observed in the weak chaos case where eventually $m_2^D(t) \propto t^{0.1}$. In addition, a slowing down of the growth rate is observed at higher times. The DVDs remain localized as depicted in Figure 4.9**(b)**, with a clear tendency of their participation number P^D (3.3) to slowly decrease.

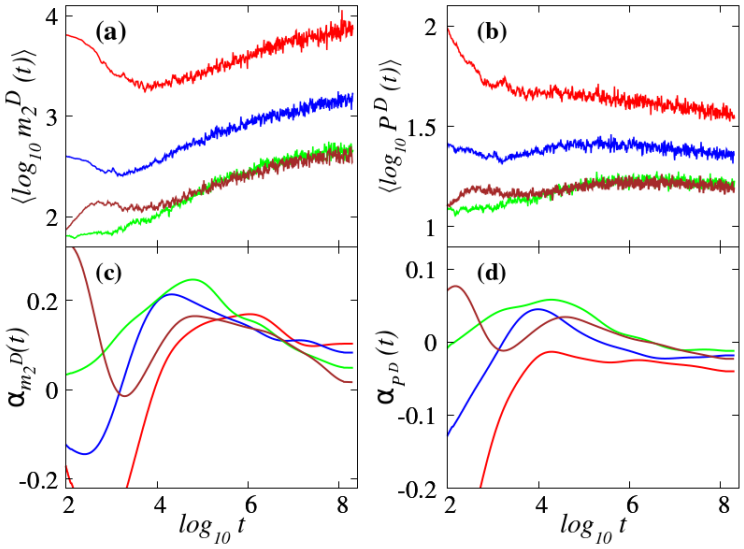

Figure 4.9: Similar to Figure 4.4 but for the strong chaos spreading regime cases $S1_1$ - $S4_1$ of Hamiltonian (2.19). Results averaged over 200 disorder realizations for the time evolution of **(a)** $m_2^D(t)$ (2.30), **(b)** $P^D(t)$ (2.31), the corresponding slopes **(c)** $\alpha_{m_2^D}(t)$ for m_2^D and **(d)** $\alpha_{P^D}(t)$ for P^D for the cases $S1_1$ - $S4_1$. The curve colours correspond to the cases presented in Figure 4.6. Panels **(a)** and **(b)** are in log-log scale while **(c)**, and **(d)** are in log-linear scale.

The final values of P^D in the cases of strong chaos are such that $13 \lesssim P^D \lesssim 100$, thus a bit higher (with signs of a tendency to saturate after t_f) compared to those observed in the weak chaos case where $0 \lesssim P^D \lesssim 13$.
Since the wave packet spreads faster for the strong chaos regime than the weak chaos case, while the DVD remains localized, one expects faster and wider movements of the chaotic seeds in order to achieve chaotization of the wave packet. Evolution of the DVD mean position $\bar{l}_w$ [white curve in Figure 4.8**(b)**], $M(t)$ (4.15) [Figure 4.10**(a)**], $R(t)$ (4.14) [Figure 4.10**(b)**] and $\iota^D(t)$ (4.16) [Figure 4.10**(c)**] confirm the chaotic seed dynamics. Each of these quantities grows reaching values larger by about one order of magnitude in comparison with the weak chaos regime [Figure 4.5 **(a)**, **(b)**, **(c)**]. The straight dashed lines in panels **(a)**, **(b)** and **(c)** of Figure 4.10 respectively show the slopes 0.24, 0.25 and 0.28 which were observed for the weak chaos cases [Figure 4.5 **(a)**, **(b)**, **(c)**]. In each of these panels [**(a)**, **(b)** and **(c)**],the quantities $M(t)$, $R(t)$ and $\iota^D(t)$ grow faster for strong chaos cases compared to weak chaos behaviour represented by the dashed lines.

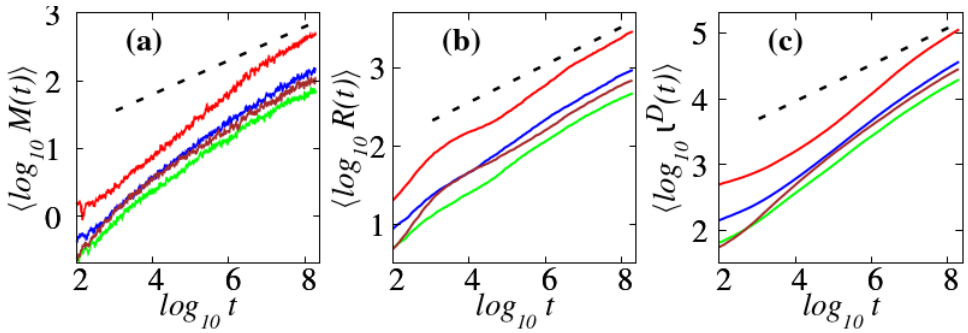

Figure 4.10: Similar to Figure 4.5 but for the strong chaos spreading regime cases $S1_1$ - $S4_1$ of Hamiltonian (2.19). Results for the time evolution of **(a)** $M(t)$ (4.14), **(b)** $R(t)$ (4.15) and **(c)** $\iota^D(t)$ (4.16). The curve colours correspond to the cases presented in Figure 4.6. The straight dashed lines guide the eye for slopes **(a)** 0.24, **(c)** 0.25 and **(c)** 0.28 which correspond to the growth of the quantities as observed and reported in the weak chaos regime [Section 4.4]. Panels **(a)**, **(b)** and **(c)** are in log-log scale.

This analysis also shows that the deviation vector meanders at higher speeds in the strong chaos regime compared to the weak chaos case.

4.6 The selftrapping chaos regime

We consider here the dynamics in the selftrapping regime of the 1D DKG model (2.19) for which the largest portion of the wave packet stays practically localized at the region of the initial excitation while some small tails propagate towards the lattice edges [Kopidakis et al. (2008); Skokos et al. (2009)]. For single site excitations leading to selftrapping behaviour, it has been shown that the wave packet second moment $m_2(t)$ grows as $m_2(t) \propto t^{1/3}$ while the participation number $P(t)$ remains practically constant [Skokos et al. (2009)].
In our study we initially excite a single site with energy $H_{1K} = h$ and integrate the system up to a final time $t_f \approx 10^{8.9}$ time units. We consider the following two parameter set ups which lead to selftrapping behaviour:
Case $ST1_1$**:** $W = 4$, $L = 1$, $h = 1.5$;
Case $ST2_1$**:** $W = 5$, $L = 1$, $h = 1$.
The lattice size $N(t)$ is increased up to a maximum value $N(t_f) \approx 1\,000$ for $ST1_1$ and $N(t_f) \approx 800$ for $ST2_1$ in order to avoid energy spreading to the boundary sites. The energy H_{1K} of the system is conserved at an absolute relative energy error (4.1) $e_r(t) \approx 10^{-5}$ using time steps $\tau \approx 0.2$ ($ST1_1$) and $\tau \approx 0.25$ ($ST2_1$) for the $ABA864$ SI. Case $ST1_1$ was studied in [Gkolias (2013)] while case $ST2_1$ is new and will contribute to the generalization of results for the selftrapping regime in the 1D DKG model. By computing the participation number $P(t)$ (2.31), we verify that the considered cases belong to the selftrapping regime. In Figure 4.11 we present the averaged results for the time evolution of the second moment $m_2(t)$ (2.30) and the participation number $P(t)$ (2.31). Panels **(a)** and **(b)** respectively show the time evolution of $m_2(t)$ and $P(t)$ for the cases $ST1_1$ (red curves) and $ST2_1$ (blue curves). In panels **(c)** and **(d)** we present the slopes $\alpha_{m_2}(t)$ of $m_2(t)$ and $\alpha_P(t)$ of $P(t)$ respectively with the dashed lines indicating the values $\alpha_{m_2} = 0.37$ [panel **(c)**] and $\alpha_P = 0$ [panel **(d)**]. The error bars in **(c)** and **(d)** respectively denote one standard deviation in the computation of slopes $\alpha_{m_2}(t)$ and $\alpha_P(t)$. These results verify that the cases considered belong to the selftrapping chaos regime since $P(t)$ [panel **(b)**] gives a practically constant value, in accordance with established results of Kopidakis et al. (2008) and Skokos et al. (2009) which emphasize that the wave packet remains localized (i.e. $P(t) \approx constant$).

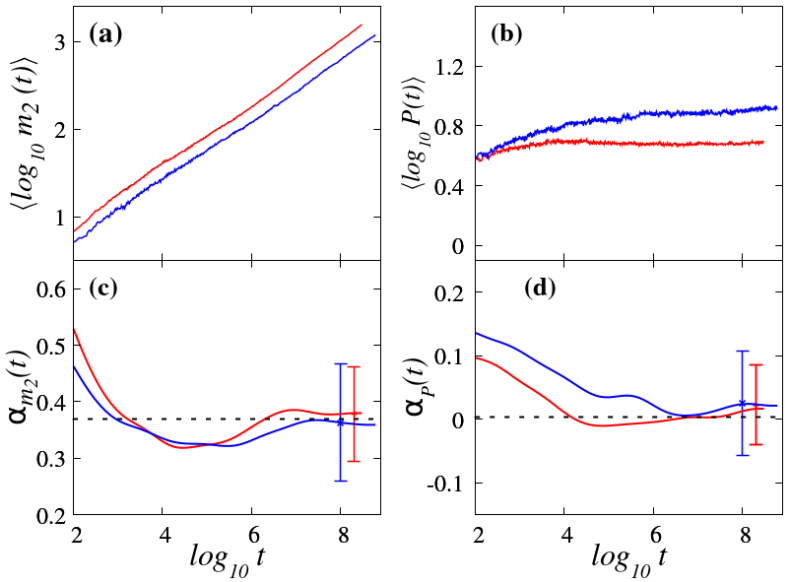

Figure 4.11: Similar to Figure 4.1. Results for the time evolution of **(a)** $m_2(t)$ (2.30), **(b)** $P(t)$ (2.31), and the corresponding slopes **(c)** $\alpha_{m_2}(t)$ for m_2 and **(d)** $\alpha_P(t)$ for P for the cases $ST1_1$ (red curves) and $ST2_1$ (blue curves). The dashed lines in panels **(c)** and **(d)** respectively guide the eye for values $\alpha_{m_2}(t) = 0.37$ and $\alpha_P(t) = 0$. The error bars in **(c)** and **(d)** denote one standard deviation in the computed slopes. Plots **(a)** and **(b)** are in log-log scale while **(c)**, and **(d)** are in log-linear scale.

The theoretical predictions and previously published work [Skokos et al. (2009)] for the power law exponents of respectively $P(t)$ and $m_2(t)$ lie within the interval centred around our numerically computed values and of width equal to one standard deviation.
We now investigate the chaoticity of the model. For each of the two selftrapping chaos cases we investigated, we compute the time evolution of $\Lambda(t)$ (3.11) and present the results in Figure 4.12.

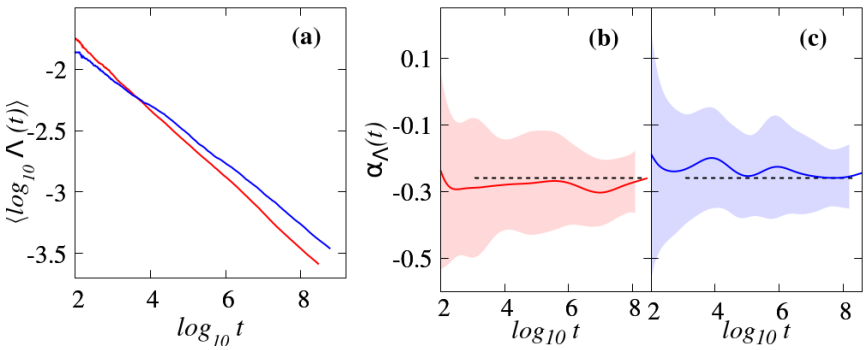

Figure 4.12: Similar to Figure 4.2. Results for the time evolution of **(a)** the finite time mLCE $\Lambda(t)$ (3.11) and **(b)**-**(c)** the corresponding numerically computed slopes for the two selftrapping chaos cases of the 1D DKG system (2.19) considered in Figure 4.11. Results are averaged over 200 disorder realizations. The curve colours correspond to the cases presented in Figure 4.11. The straight dashed lines in **(b)** - **(c)** indicate the value $\alpha_\Lambda = -0.26$. Panel **(a)** is in log-log scale while panels **(b)**-**(c)** are in log-linear scale.

In panel **(a)** of Figure 4.12, the time evolution of the finite time mLCE $\Lambda(t)$ (3.11) averaged over 200 disorder realisations for the selftrapping cases $ST1_1$ and $ST2_1$ is reported. The corresponding evolution of derivatives α_Λ is shown in panels **(b)** and **(c)**. These results show that the chaoticity of system (2.19) is characterised by the power law $\Lambda(t) \propto t^{-0.26}$,

a law similar to what we observed for the weak chaos regime, and does not show any tendencies to crossover to regular dynamics for the entire duration of our integration. From the numerical computations of m_2 and Λ, the ratio R_{m_2} (4.11) gives the value

$$R_{m_2} \sim t^{0.37},$$

since $\alpha_{m_2} = 0.37$ and $\alpha_\Lambda = -0.26$. The wave packet therefore gets more chaotic much faster compared to it's spreading since the chaoticity time scale T_Λ is always smaller than the spreading time scale T_{m_2}.

Deviation vector distributions

We now investigate the deviation vector dynamics in this regime of chaos. Like for the weak and strong chaos cases presented before, we first present a representative realisation, after which we give averaged results for 200 disorder realisations.
In Figure 4.13 we present the evolution of the **(a)** energy density $\xi_l(t)$ (4.2) and **(b)** DVD $\xi^D(t)$ (3.2) for a representative realisation belonging to case $ST1_1$.

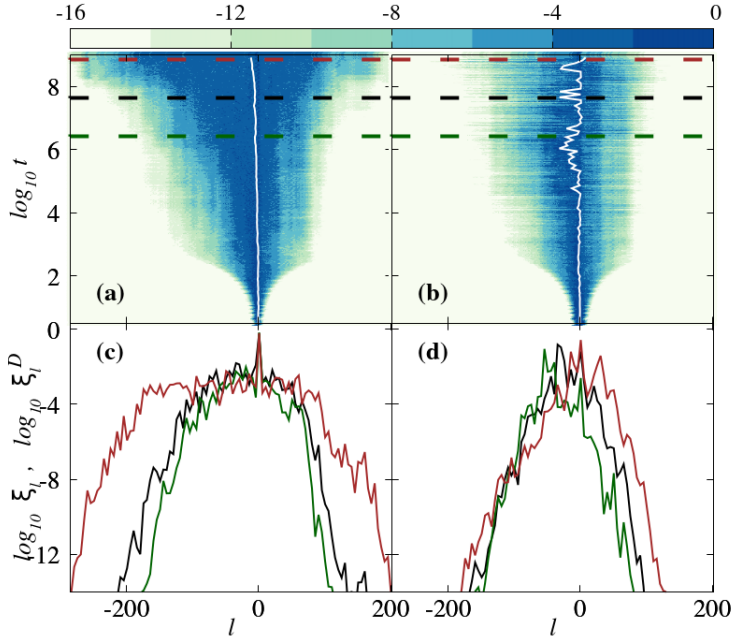

Figure 4.13: Similar to Figure 4.3. Results for the time evolution of **(a)** the normalized energy distribution $\xi_l(t)$ (4.2) and **(b)** the corresponding DVD $\xi_l^D(t)$ (3.2). The colour scales at the top of the figure are used for colouring lattice sites according to their **(a)** $\log_{10}\xi_l(t)$ and **(b)** $\log_{10}\xi_l^D(t)$ values. In each of the panels **(a)** and **(b)** the white curve traces the distributions' centre. **(c)** Normalized energy distributions and **(d)** DVDs at times $\log_{10} t = 6.4$ [green curve], $\log_{10} t = 7.6$ [black curve], $\log_{10} t = 8.8$ [red curve]. These times are also denoted by similarly coloured horizontal dashed lines in **(a)** and **(b)**.

In panels **(a)** and **(b)** the position of the distributions' mean value is traced by a thick white curve while in panels **(c)** and **(d)** we show three snapshots of the distributions correspondingly taken at times indicated by the horizontal lines of panels **(a)** and **(b)** with matching colours. The centre of the lattice has been translated to 0. We note that the energy distribution has high values in the lattice centre, which corresponds to the trapped part of the wave packet. This is visible in panel **(c)** where the snapshots have very sharp pointy peaks at the centre of the energy profiles. The snapshots of Figure 4.13**(d)** and the mean position [traced by white curve in **(b)**] show that the DVD distribution centre

fluctuates with increasing amplitudes as the energy spreads to more sites of the lattice. The DVD behaviour shown by the single realisation in Figure 4.13 is characteristic of the behaviour for the considered cases as revealed by the computations of $m_2^D(t)$ (2.30) and $P^D(t)$ (2.31) performed for more disorder realisations.
Figure 4.14 shows results for **(a)** $m_2^D(t)$ (2.30), **(b)** $P^D(t)$ (2.31) and the corresponding slopes **(c)** $\alpha_{m_2^D}$ of $m_2(t)$ and **(d)** α_{P^D} of $P(t)$.

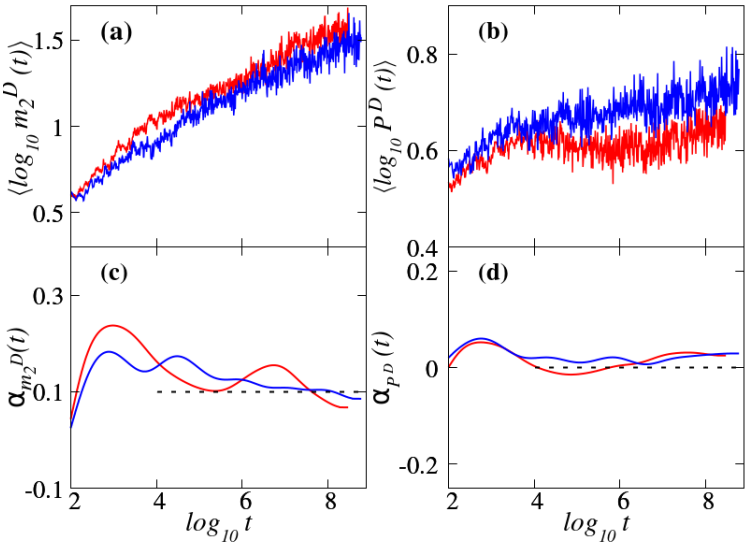

Figure 4.14: Similar to Figure 4.4. Results averaged over realizations for the time evolution of **(a)** $m_2^D(t)$ (2.30), **(b)** $P^D(t)$ (2.31), the corresponding slopes **(c)** $\alpha_{m_2^D}(t)$ for m_2^D and **(d)** $\alpha_{P^D}(t)$ for P^D for the cases $ST1_1$ and $ST2_1$. The dashed lines in panels **(c)** and **(d)** respectively indicate values $\alpha_{m_2^D}(t) = 0.1$ and $\alpha_{P^D}(t) = 0$. The curve colours correspond to the cases presented in Figure 4.11. Panels **(a)** and **(b)** are in log-log scale while **(c)**, and **(d)** are in log-linear scale.

The straight dashed lines are slope values $\alpha_{m_2^D}(t) = 0.1$ and $\alpha_{P^D}(t) = 0$. We see that, just like for the weak chaos case, the second moment has a low growth rate, close to 0.1, while the participation number of the DVD is also practically constant.
In Figure 4.15 we present results obtained for the quantities $M(t)$ (4.14) [panel **(a)**], $R(t)$ (4.15) [panel **(b)**] and $\iota^D(t)$ (4.16) [panel**(c)**] with the dashed lines guiding the eye for the

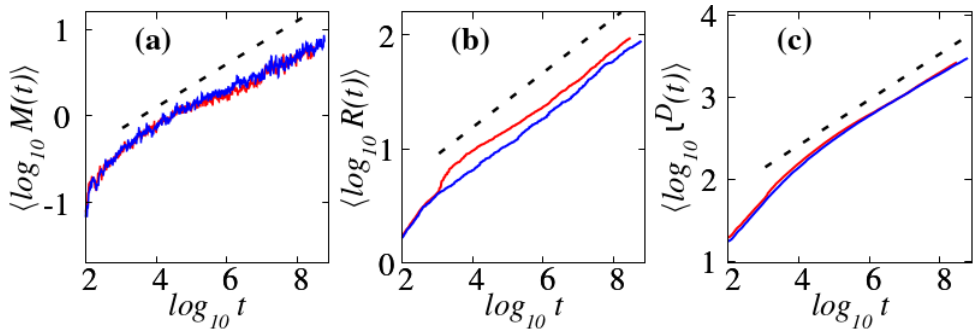

Figure 4.15: Similar to Figure 4.5 but for the selftrapping chaos spreading regime cases $ST1_1$ and $ST2_1$ of Hamiltonian (2.19). Results for the time evolution of **(a)** $M(t)$ (4.14), **(b)** $R(t)$ (4.15) and **(c)** $\iota^D(t)$ (4.16). The curve colours correspond to the cases presented in Figure 4.11. The straight dashed lines guide the eye for slopes **(a)** 0.24, **(c)** 0.25 and **(c)** 0.28 which correspond to the growth observed in the weak chaos regime. Panels **(a)**, **(b)** and **(c)** are in log-log scale.

slopes 0.24 in **(a)**, 0.25 in **(b)** and 0.28 in **(c)** which were obtained for the weak chaos case [Figure 4.5]. The values of $M(t)$ [Figure 4.15**(a)**], $R(t)$ [Figure 4.15**(b)**] and $\iota^D(t)$ [Figure 4.15**(c)**] continuously increase the entire time of the integration. This is because the meandering localized chaotic seeds have to cover wider regions of the lattice as time increases. The quantities $M(t)$, $R(t)$ and $\iota^D(t)$ have growth rates which are approximately equal to those of the weak chaos case (indicated by the straight lines).

4.7 Summary

We investigated the chaotic behaviour of the 1D DKG model (2.19) in the weak, strong and selftrapping chaos regimes. We performed extensive simulations for chaotic spreading of initially localized excitations, for several parameter cases and obtained statistical results on ensembles of approximately 200 disorder realizations in each case. For all three regimes we compute the finite time mLCE $\Lambda(t)$ (3.11), a widely used chaos indicator, and show evidence that although the wave packet chaoticity strength decreases in time the dynamics shows no tendency to cross to regular behaviour. $\Lambda(t)$ decreases following a power law $\Lambda(t) \propto t^{\alpha_\Lambda}$, which is characterized by α_Λ values different from $\alpha_\Lambda = -1$ observed for regular motion. In particular, we found that $\alpha_\Lambda \approx -0.25$ for the weak chaos regime [in agreement with the findings of Skokos et al. (2013) and Gkolias (2013)], $\alpha_\Lambda \approx -0.32$ for the strong chaos regime and $\alpha_\Lambda \approx -0.26$ for the selftrapping chaos regime. From the theoretical explanation of the relation between the chaotic regime and the dynamical characteristics we see that for all considered regimes of chaos, the chaoticity time scale $T_\Lambda(t)$ (4.4) always remains smaller than the spreading time scales $T_{m_2}(t)$ (4.7) and or $T_P(t)$ (4.9). This implies that wave packet gets more chaotic at a rate faster than its spreading.

The computation of the corresponding DVDs created by the deviation vector used to compute $\Lambda(t)$ and of quantities related to their dynamics (m_2^D, P^D, R, M, ι^D), allowed us to better capture the instantaneous and long term features of the underlying chaotic behaviour and to quantify the meandering tendencies of chaotic seeds inside the wave packet. In all studied cases the DVD retained a localized, pointy shape with its participation number $P^D(t)$ remaining asymptotically constant at small values. As time increased the DVD exhibited oscillations of larger amplitudes in order to visit all regions inside the spreading wave packet. As a results, the quantities M (4.14), R (4.15) and ι^D (4.16) which estimate the range of the lattice region visited by the DVD, increased in time. This increase was characterized by power law growths, $R(t) \propto t^{0.24}$, $M(t) \propto t^{0.25}$ and $\iota^D(t) \propto t^{0.28}$ in the weak chaos regime. On the other hand, in the strong chaos case R, M and ι^D grow with higher, but non constant, rates since the wave packet spreads faster than in the weak chaos case and the DVD visits a wider region. It is worth noting that this rate decreases in time, tending to the values observed in weak chaos regime. This is a direct consequence of the transient nature of the strong chaos regime, as this regime eventually crosses over toward the weak chaos dynamics. For the selftrapping case, quantity $R(t)$ grows at the same rate as observed in the weak chaos regime while $M(t)$ and $\iota^D(t)$ have a slightly slower growth.

In conclusion, we numerically verified for the weak and strong chaos spreading regimes of the 1D DKG model (2.19) that (a) the deterministic chaoticity of wave packet dynamics persists in time, although its strength decreases; (b) chaotic seeds meander inside the wave packet fast enough to ensure its chaotization; and (c) the characteristics of chaos evolution (like for example the power law $\Lambda(t) \propto t^{\alpha_\Lambda}$) in the weak and strong

chaos regimes are distinct for each case (e.g. $\alpha_\Lambda \approx -0.25$ for weak chaos and $\alpha_\Lambda \approx -0.32$ for strong chaos).
In Chapter 5 we present the investigation of the chaotic behaviour for disordered lattices in two spatial dimensions as we try to understand the behaviour in higher spatial dimensions.

Chapter 5

Chaotic behaviour of the 2D DKG model

In this chapter we investigate the chaotic nature of dynamics for the 2D DKG model (2.22), extending the studies of Chapter 4 to two spatial dimensions. We present our findings as follows: In Section 5.1 we highlight the numerical techniques used for the computation of our results. We then present our findings for the different classifications of chaotic dynamical behaviours namely, the weak chaos spreading regime in Section 5.3, the strong chaos case in Section 5.4 and the selftrapping behaviour in Section 5.5. Lastly, we discuss and summarize our discussion on dynamics of the 2D model in Section 5.6. Parts of the results presented in Sections 5.3 and 5.4 of this chapter have also been reported in Many Manda et al. (2020).

5.1 Numerical techniques

The numerical techniques used for the 2D DKG model (2.22) are similar to the ones used for the 1D DKG model (2.19) whose dynamics has been presented in Chapter 4. In particular, we once again implement the two-part split order four SI ABA864 [Chapter 3, Blanes et al. (2013)] to solve the variational equations by applying equations (3.25) whose explicit form is given in Appendix (A.2). In our simulations, the absolute relative energy error

$$e_r(t) = \frac{|H_{2K}(t) - H_{2K}(0)|}{H_{2K}(0)}, \tag{5.1}$$

of the integration is kept at $e_r(t) \approx 10^{-5}$ by using time steps $\tau \approx 0.2 - 0.9$. Furthermore, in our study we use initial deviation vectors of the form **2** [Section 3.4.2; Figure 3.6**(b)**] where only the position and momentum coordinates of square sub-lattices of sizes from 3×3 to 25×25 at the centre of the lattice are non-zero.

The numerical simulations were performed using the FORTRAN 90 programming language with OPENMP parallelization allocation of an average of $4 - 8$ threads (CPU-cores) for each simulation.

We use lattices whose size, $N \times M$, increases with time [i.e. $N(t)$ and $M(t)$ are smallest at $t = 0$] depending on the wave packet extent while avoiding any boundary effects to the dynamics of the system. We start with a relatively small lattice of extent coverage $N(0) \times M(0)$ and increase it whenever either the wave packet or the deviation vector distribution gets close to the boundary sites. We ensure this by checking that for each site (l, m) in an exterior strip of width N_W at the lattice boundary, the site energy

$$h_{l,m} = \frac{p_{l,m}^2}{2} + \frac{\epsilon_{l,m}}{2} q_{l,m}^2 + \frac{q_{l,m}^4}{4} + \frac{1}{4W}\left[q_{l,m+1} - q_{l,m})^2 + ((q_{l+1,m} - q_{l,m})^2\right] \tag{5.2}$$

and the corresponding square norm component $\delta q_{l,m}^2 + \delta p_{l,m}^2$ of the deviation vector at this site are always less than 10^{-8}. That is to say, for each site (l, m) in an exterior strip of width N_W we ensure

$$\max_{l,m}\{h_{l,m}\} < 10^{-8} \qquad \text{and} \qquad \max_{l}\{\delta q_{l,m}^2 + \delta p_{l,m}^2\} < 10^{-8}. \tag{5.3}$$

The lattice size is uniformly increased by a width dependant on the particular W in case criteria (5.3) is not fulfilled. For smaller disorder strength W we increase the lattice by more sites compared to a larger W. For simplicity, we use a square lattice where $N(t) = M(t)$ for our study.
We compute the slopes of data-curves using the LOESS procedure and the central finite differences described in Section 4.1.4.

5.2 Procedure for numerical simulations

In all our numerical simulations, we give the system a total energy H_{2K} (2.22) by initially exciting a block of $L \times J$ central sites of the $N(0) \times M(0)$ lattice. We give each of the sites in the central block energy $h = h_{l,m} = H_{2K}(0)/(L \cdot J)$ by setting $p_{l,m} = \pm\sqrt{2h}$ with random signs and $p_{l,m} = q_{l,m} = 0$ for all other sites. We use the fixed boundary conditions $q_{0,m} = q_{N+1,m} = q_{l,M+1} = q_{l,0} = 0$ and $p_{0,m} = p_{N+1,m} = p_{l,M+1} = p_{l,0} = 0$ for all $0 < l < N + 1$ and $0 < m < M + 1$. Once again we follow the time evolution of different dynamical quantities for several ICs and various disorder realizations of the system (2.22) where we obtain statistical results by averaging the values over 50 different disorder realizations.

5.3 The weak chaos regime

The participation number $P(t)$ (2.35) and second moment $m_2(t)$ (2.34), in the 2D DKG model, are known to characterize the energy spreading extent as $P(t) \propto t^{1/5}$ and $m_2(t) \propto t^{1/5}$ [Laptyeva et al. (2012)] respectively in the weak chaos regime. The system is known to behave chaotically and not cross to regular dynamical behaviour, characterised by $\Lambda(t) \propto t^{-1}$ [Benettin et al. (1976); Skokos (2010)].
Our numerical integrations are up to a maximum final time $t_f \approx 10^8$ time units with the lattice $N \times M$ increased up to size with dimension lengths in range $N(t_f) = M(t_f) \approx 300 - 500$. The energy H_{2K} of the system was conserved at an absolute relative energy error (5.1) $e_r(t) \approx 10^{-5}$ for time steps of size range $\tau \approx 0.4 - 0.9$. For the following four weak chaos parameter cases, we investigate chaos in the system (2.22) where a total of $L \cdot J$ central sites (which make up sub-lattice $L \times J$) of the lattice are excited with energy density h and disorder strength W. For simplicity, we take $L = J$ and $N(t) = M(t)$.
Case $W1_2$**:** $W = 10$, $L = 1$, $h = 0.05$;
Case $W2_2$**:** $W = 10$, $L = 1$, $h = 0.3$;
Case $W3_2$**:** $W = 10$, $L = 3$, $h = 0.0085$;
Case $W4_2$**:** $W = 11$, $L = 2$, $h = 0.0175$.
For each of these cases, we average the computations over 50 disorder realizations. We first verify that the selected cases $W1_2$, $W2_2$, $W3_2$ and $W4_2$ belong to the weak chaos regime. Case $W2_2$ was studied in Laptyeva et al. (2012) as belonging to weak chaos with some of its dynamical quantities based on the wave packet computed and findings reported. In our work, we recalculate these quantities and also include some qualitative and statistical results about the evolution of the deviation vector for each of the four cases. In some sense, case $W2_2$ also acts as a benchmark for our investigation.

In Figure 5.1 we present the averaged results for the evolution of $m_2(t)$ (2.34) [panel **(a)**] and $P(t)$ (2.35) [panel **(b)**] for the cases $W1_2$ (red curves), $W2_2$ (brown curves), $W3_2$ (blue curves), and $W4_2$ (green curves).

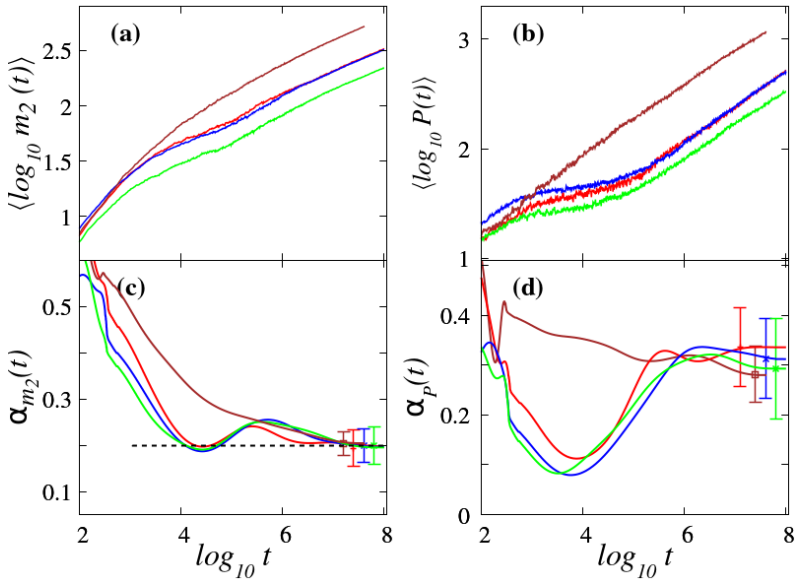

Figure 5.1: Results for the time evolution of **(a)** $m_2(t)$ (2.34), **(b)** $P(t)$ (2.35), the corresponding slopes **(c)** $\alpha_{m_2}(t)$ for $m_2(t)$ and **(d)** $\alpha_P(t)$ for $P(t)$ for the weak chaos cases $W1_2$ (red curves), $W2_2$ (brown curves), $W3_2$ (blue curves) and $W4_2$ (green curves) of Hamiltonian (2.22). The dashed line in **(c)** denotes the value $\alpha_{m_2} = 0.2$. Each error bar denotes a standard deviation in the corresponding computed slope. Plots **(a)** and **(b)** are in log-log scale while **(c)** and **(d)** are in log-linear scale.

The corresponding slopes $\alpha_{m_2}(t)$ of $m_2(t)$ and $\alpha_P(t)$ of $P(t)$ respectively are shown in panels **(c)** and **(d)** with the dashed line indicating the average value $\alpha_{m_2} = 0.2$ [panel **(c)**] which is computed for the saturated slopes at the end of the integration. These results verify that the cases considered show weak chaos behaviour since the evolution of $m_2(t)$ [panel **(a)**] follows the power laws $m_2 \propto t^{0.2}$ [panel **(c)**], in accordance with established results of Laptyeva et al. (2012) which emphasize the same power law growth reported here for $m_2(t)$. α_P on the other hand is observed to be approximately 0.31 by the final time of integration. The theoretical value of $\alpha_P = 0.2$ could be possible to attain after longer times $log_{10}t > 10^8$ that we could not reach due to computational challenges. The error bars shown in panels **(c)** and **(d)** are computations of a standard deviation of the quantities $\alpha_{m_2}(t)$ and $\alpha_P(t)$ respectively.

We investigate the chaoticity of the system using the finite time mLCE $\Lambda(t)$ (3.11). For each of the cases we numerically compute $\Lambda(t)$ (3.11) and present the results, averaged over 50 disorder realizations, in Figure 5.2**(a)**. The corresponding numerically computed slopes (4.12) of the curves in panel **(a)** together with an error (color shading) defined as one standard deviation of the distribution of computed slopes α_Λ are plotted in panels **(b)**-**(e)**. The horizontal dashed lines in **(b)**-**(d)** denote the value $\alpha_\Lambda = -0.37$. The results of Figure 5.2 **(b)**-**(d)** indicate that the time evolution of $\Lambda(t)$ in the weak chaos regime eventually follows the power law $\Lambda(t) \propto t^{-0.37}$. The light color shade correspond to an error of one standard deviation in the numerically computed slopes.

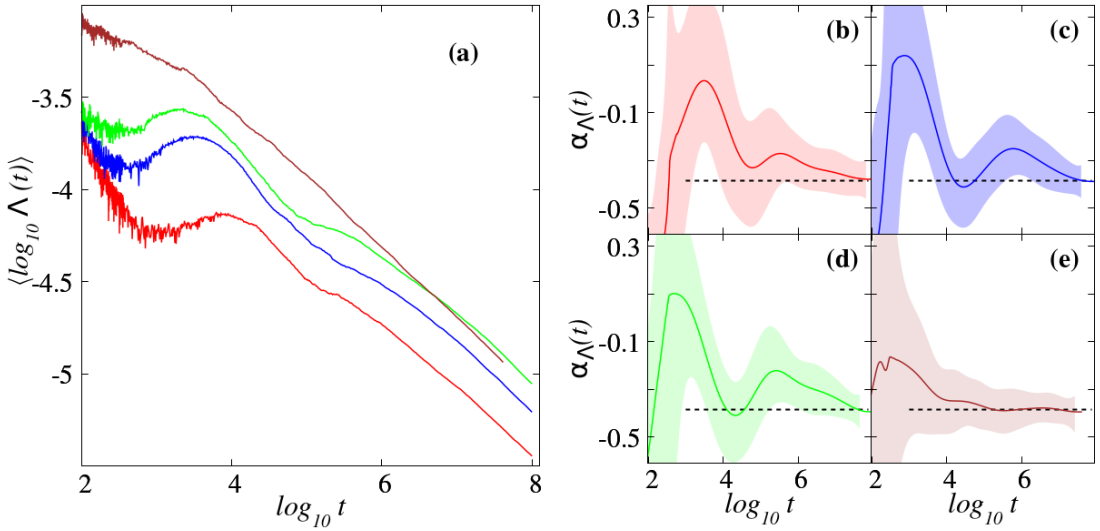

Figure 5.2: Results for **(a)** the time evolution of the finite time mLCE $\Lambda(t)$ (3.11) and **(b)**-**(d)** the corresponding numerically computed slopes for the four weak chaos cases of the 2D DKG system (2.22) considered in Figure 5.1. Results are averaged over 50 disorder realizations. The straight dashed lines in **(b)** - **(e)** indicate the value $\alpha_\Lambda = -0.37$. The curve colors correspond to the cases presented in Figure 5.1. Panel **(a)** is in log-log scale while panels **(b)**-**(e)** are in log-linear scale.

As we can see from the results in Figure 5.2, the dynamics of the system (2.22) shows no tendency to cross to regular behaviour as the computed exponent α_Λ [panels **(b)**-**(d)** of Figure 5.2] of the finite time mLCE (3.11) saturates around $\alpha_\Lambda \approx -0.37 \neq -1$ for all the considered cases. The ratios R_{m_2} and R_P of (4.11) become

$$R_{m_2} \sim t^{0.43} \text{ and } R_P \sim t^{0.32},$$

since $\alpha_{m_2} = 0.2$, $\alpha_P = 0.31$ and $\alpha_\Lambda = -0.37$. The chaoticity time scale $T_\Lambda(t)$ is therefore smaller than the spreading time scales $T_{m_2}(t)$ and $T_P(t)$. The growth therefore of chaoticity is higher than that of spreading in the weak chaos regime of the 2D DKG model (2.22).

Deviation vector distributions

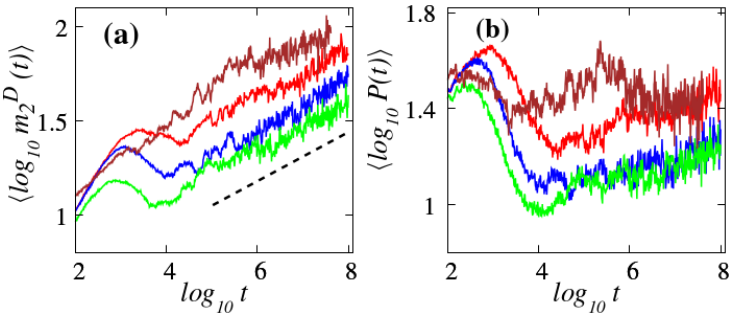

Figure 5.3: Results averaged over 50 realizations for the time evolution of **(a)** $m_2^D(t)$ (2.34) and **(b)** $P^D(t)$ (2.35) for the cases $W1_2$ - $W4_2$. The dashed straight line in panel **(a)** indicates the slope 0.13. The curve colors correspond to the cases presented in Figure 5.1. Panels **(a)** and **(b)** are in log-log scale.

We now make an investigation of the DVD and some of it's characteristics in relation to the dynamics of the system (2.22). We compute the evolution of $m_2^D(t)$ (3.4) and

participation number $P^D(t)$ (3.3) and present their average results in Figure 5.3. The DVDs' second moment $m_2^D(t)$ [Figure 5.3**(a)**] shows a slow growth following the power law $m_2^D(t) \propto t^{0.13}$ and it reaches values always smaller than those computed for wave packets' $m_2(t)$ [Figure 5.1**(a)**]. The participation number $P^D(t)$ of the DVD attains relatively smaller values, $P^D \lesssim 40$ (the lowest value being $P^D \approx 13$ for case $W4_2$ [green curves in Figure 5.3 **(b)**]). This shows that, compared to the energy distributions, the DVDs are more localized and they keep a narrow and pointy shape with a relatively slow growth in the regime of weak chaos.

We now present findings for the fluctuations of the DVD and it's centre by following the time evolution of $M(t)$ (4.14), $R(t)$ (4.15) and $\iota^D(t)$ (4.16) which were defined in Section 4.4. In Figure 5.4 we present results for the $M(t)$ [panel **(a)**], $R(t)$ [panel **(b)**] and $\iota^D(t)$ [panel**(c)**] where the dashed lines guide the eye for slopes 0.29 in **(a)**, 0.25 in **(b)** and 0.28 in **(c)**.

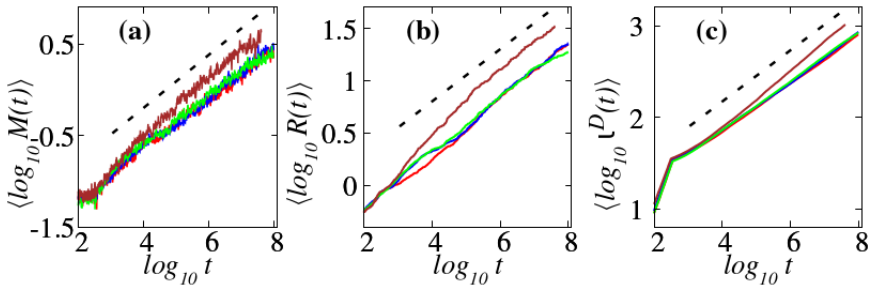

Figure 5.4: Results for the time evolution of **(a)** $M(t)$ (4.14), **(b)** $R(t)$ (4.15) and **(c)** $\iota^D(t)$ (4.16) of the DVD for cases $W1_2$ - $W4_2$ of Hamiltonian (2.22). The curve colours correspond to the cases presented in Figure 5.1. The straight dashed lines guide the eye for slopes **(a)** 0.29, **(b)** 0.25 and **(c)** 0.28. The plots are in log-log scale.

The results from the evolution of M, R and ι^D show a strict increase in these quantities thereby indicating that chaotic seeds constantly meander in the lattice.

5.4 The strong chaos regime

The time evolution of the second moment $m_2(t)$ (2.34) and participation number $P(t)$ (2.35) of the 2D DKG model wave packet is known to follow as $m_2(t) \propto t^{1/3}$ and $P(t) \propto t^{1/3}$ [Laptyeva et al. (2012)] in the strong regime of chaos. We investigate the behaviour of energy propagation in this regime. We numerically integrate the system (2.22) up to a final time $t_f \approx 10^{7.7}$ (i.e. $t_f \approx 50{,}000{,}000$) time units with the lattice $N \times M$ increased up to a size with dimension lengths in range $N(t_f) = M(t_f) \approx 300 - 500$. The energy H_{2K} of the system was conserved at an absolute relative energy error (5.1) $e_r(t) \approx 10^{-5}$ for time steps of size range $\tau \approx 0.4 - 0.9$. A total of $L \cdot J$ central sites (which make up sub-lattice $L \times J$) of the lattice are excited with energy density h and disorder strength W. Taking $L = J$ and $N(t) = M(t)$, we consider the following four parameter cases:

Case $S1_2$**:** $W = 9$, $L = 35$, $h = 0.006$;
Case $S2_2$**:** $W = 10$, $L = 21$, $h = 0.0135$;
Case $S3_2$**:** $W = 12$, $L = 21$, $h = 0.01$;
Case $S4_2$**:** $W = 12.5$, $L = 15$, $h = 0.035$.

The results of Figure 5.5 show that each of the cases $S1_2$-$S4_2$ exhibits the characteristics of strong chaos, where $m_2(t)$ (2.34) and $P(t)$ (2.35) respectively follow the power laws

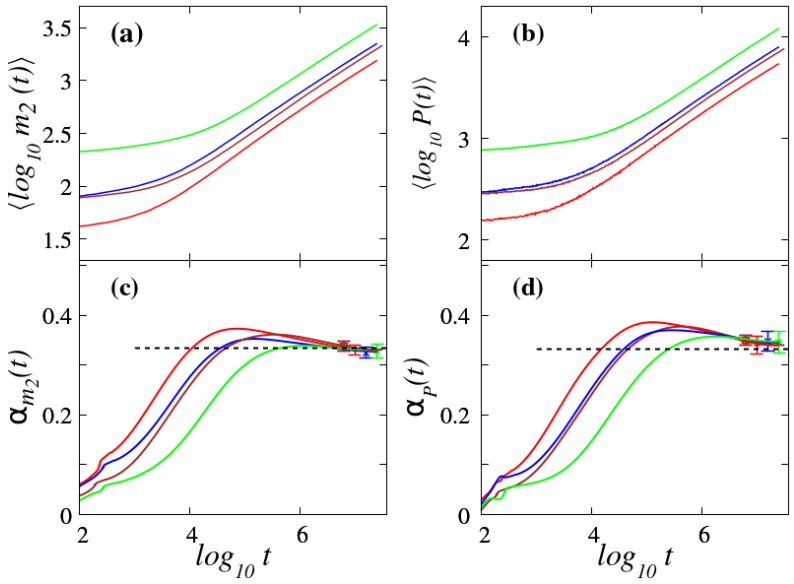

Figure 5.5: Similar to Figure 5.1 but for the strong chaos spreading regime of Hamiltonian (2.22). Results for the time evolution of **(a)** $m_2(t)$ (2.34), **(b)** $P(t)$ (2.35), the corresponding slopes **(c)** $\alpha_{m_2}(t)$ for $m_2(t)$ and **(d)** $\alpha_P(t)$ for $P(t)$ for the cases $S1_2$ (green curves), $S2_2$ (blue curves), $S3_2$ (brown curves) and $S4_2$ (red curves). The dashed lines in panels **(c)** and **(d)** indicate values $\alpha_{m_2} = 0.33$ and $\alpha_P = 0.33$ respectively. The error bars in **(c)** and **(d)** are a standard deviation of the computed slopes. Plots **(a)** and **(b)** are in log-log scale while **(c)**, **(d)** is in log-linear scale.

$m_2(t) \propto t^{\alpha_{m_2}}$ [panels **(a)** and **(c)**] and $P(t) \propto t^{\alpha_P}$ [panels **(b)** and **(d)**], for values $\alpha_P = \alpha_{m_2} = 0.33$ [shown by dashed lines in **(c)** and **(d)**] and in agreement with the theoretical estimates [Laptyeva et al. (2012)]. The error bars in **(c)** and **(d)** are each one standard deviation of the slopes α_{m_2} and α_P respectively.
In Figure 5.6, we present results for the evolution of $\Lambda(t)$ (3.11) where we observe an

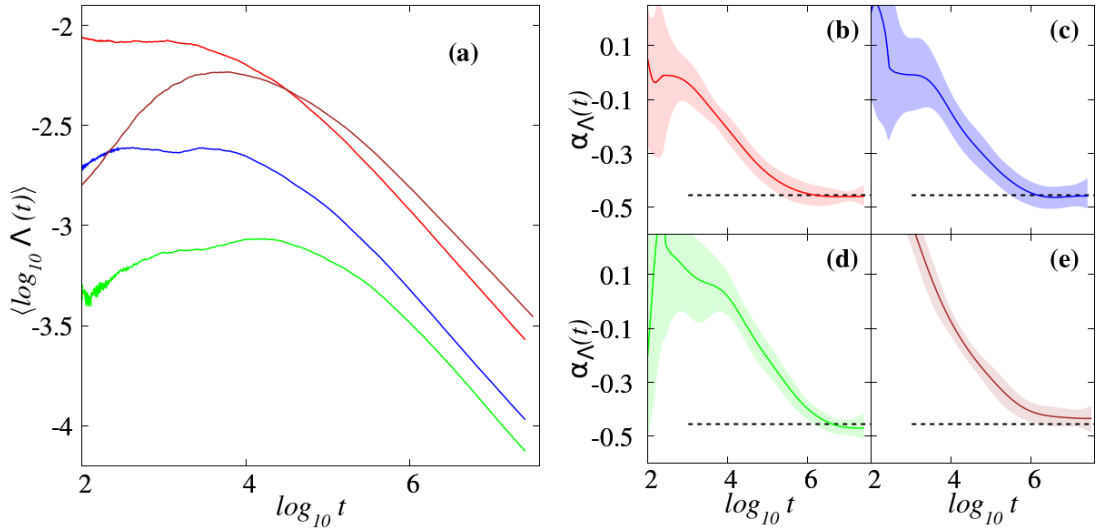

Figure 5.6: Similar to Figure 5.2 but for the strong chaos spreading regime of Hamiltonian (2.22). Results for the time evolution of **(a)** the finite time mLCE $\Lambda(t)$ (3.11) and **(b)**-**(e)** the corresponding derivatives for the cases $S1_2$ (green curves), $S2_2$ (blue curves), $S3_2$ (brown curves) and $S4_2$ (red curves). The straight dashed lines indicate slopes $\alpha_\Lambda = -0.46$. Panel **(a)** is in log-log scale while panels **(b)**-**(e)** are in log-linear scale.

eventual power law decay $\Lambda(t) \propto t^{\alpha_\Lambda}$ with no tendency to cross to the regular dynamics law $\Lambda(t) \propto t^{-1}$. The exponent $\alpha_\Lambda \approx -0.46$ is different from the one of the weak chaos case where $\alpha_\Lambda \approx -0.37$. This shows the difference in the chaoticity of the system (2.22) for the two regimes.
The spreading to chaoticity time scale ratios R_{m_2} and R_P of (4.11) are therefore

$$R_{m_2},\ R_P \sim t^{0.21},$$

since $\alpha_{m_2} = \alpha_P = 0.33$ and $\alpha_\Lambda = -0.46$. $T_\Lambda(t)$ is therefore smaller than either of $T_{m_2}(t)$ or $T_P(t)$.

Deviation vector distributions

In Figure 5.7 we present averaged results for the DVDs' second moment $m_2^D(t)$ [Figure 5.7**(a)**] and the participation number $P^D(t)$ [Figure 5.7**(b)**] for the strong chaos cases $S1_2$ - $S4_2$.

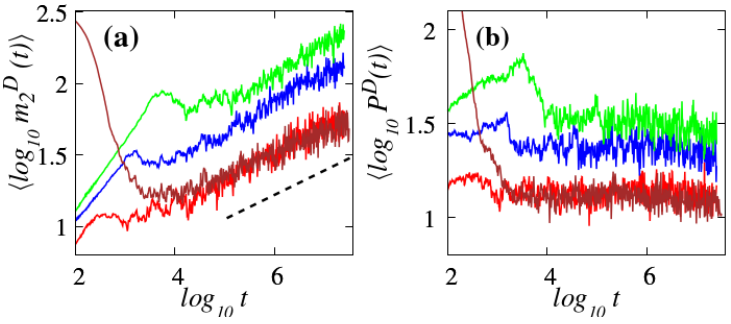

Figure 5.7: Similar to Figure 5.3 but for the strong chaos spreading regime cases $S1_2$ - $S4_2$ of Hamiltonian (2.22). Results averaged over 50 disorder realizations for the time evolution of **(a)** $m_2^D(t)$ (2.34) and **(b)** $P^D(t)$ (2.35). The curve colors correspond to the cases presented in Figure 5.5. The straight dashed line in **(a)** guides the eye for slope 0.17. Panels **(a)** and **(b)** are in log-log scale while **(c)**, and **(d)** are in log-linear scale.

The $m_2^D(t)$ follows a power law $m_2^D(t) \propto t^{0.17}$ which shows a faster growth in the spatial extent of the DVD compared to revelations from the weak chaos cases whose power law was $m_2^D(t) \propto t^{0.13}$. The DVD participation number $P^D(t)$ on the other hand is practically constant as seen in Figure 5.7**(b)**. These findings show that in the strong chaos regime, the DVD keeps spreading just like in the weak chaos case, but gets a more pointy shape.

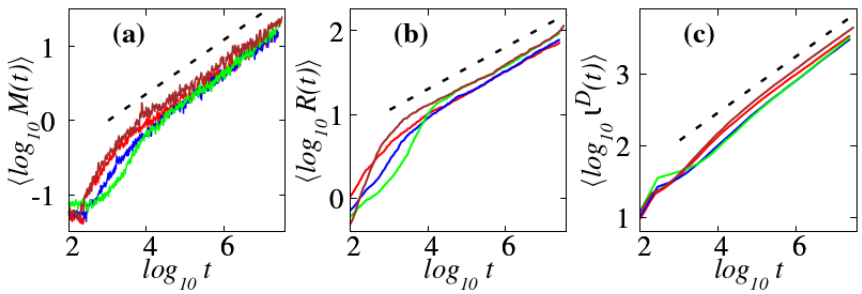

Figure 5.8: Similar to Figure 5.4 but for the strong chaos spreading regime cases $S1_2$ - $S4_2$ of Hamiltonian (2.22). Results for the time evolution of **(a)** $M(t)$ (4.14), **(b)** $R(t)$ (4.15) and **(c)** $\iota^D(t)$ (4.16). The curve colours correspond to the cases presented in Figure 5.5. The straight dashed lines guide the eye for slopes **(a)** 0.37, **(b)** 0.25 and **(c)** 0.39. The panels are in log-log scale.

In Figure 5.8 we show the results for the evolution of DVD quantities $M(t)$ (4.14), $R(t)$ (4.15) and $\iota^D(t)$ (4.16). The straight dashed lines show that these quantities grow following power laws $M(t) \propto t^{0.37}$ [Figure 5.8**(a)**], $R(t) \propto t^{0.25}$ [Figure 5.8**(b)**] and $\iota^D(t) \propto t^{0.39}$ [Figure 5.8**(c)**]. This shows that the quantities $R(t)$, $M(t)$ and $\iota^D(t)$ in the strong chaos regime grow with the same or higher power law exponents compared to the weak chaos case where results showed that $M(t) \propto t^{0.29}$ [Figure 5.4**(a)**], $R(t) \propto t^{0.25}$ [Figure 5.4**(b)**] and $\iota^D(t) \propto t^{0.28}$ [Figure 5.4**(c)**]. Since $M(t) \leq R(t)$ (4.17) and our results show $M(t)$ is growing faster than $R(t)$, it means that at some point $M(t)$ will have to slow down so as to satisfy the bound relation (4.17).

5.5 The selftrapping chaos regime

In the selftrapping chaos regime, the participation number $P(t)$ (2.35) of the wave packet remains practically constant as the system evolves. For our investigation in this regime, we numerically integrate the system (2.22) up to a final time $t_f \approx 10^{7.7}$ (i.e. $t_f \approx 50{,}000{,}000$) time units with the lattice $N \times M$ increased up to size with dimension lengths in range $N(t_f) = M(t_f) \approx 350$. The energy H_{2K} of the system was conserved at an absolute energy relative error (5.1) $e_r(t) \approx 10^{-5}$ for time step $\tau \approx 0.7$. A single site located at the centre of the lattice is excited with energy density $h = 2.0$ and disorder strength $W = 10$ is used. We refer to this configuration as case ST_2. ST_2 was studied in Laptyeva et al. (2012) and classified as leading to chaotic behaviour in the selftrapping regime. In our work we investigate this parameter set and we compare the resultant dynamics with that of the weak and strong chaos regimes.
In Figure 5.9 we present the time evolution of $m_2(t)$ (2.34) and $P(t)$ (2.35) [panel **(a)**] and $\Lambda(t)$ (3.11) [panel **(b)**].

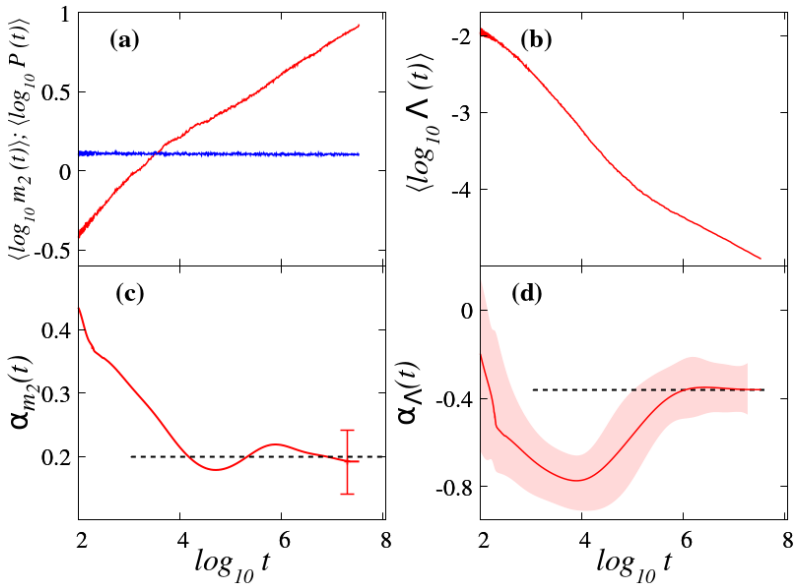

Figure 5.9: Results for the time evolution of **(a)** $m_2(t)$ (2.34) [red curve] and $P(t)$ (2.35) [blue curve], **(b)** the finite time mLCE $\Lambda(t)$ (3.11), the corresponding slopes **(c)** $\alpha_{m_2}(t)$ for m_2 and **(d)** $\alpha_\Lambda(t)$ for $\Lambda(t)$ for the selftrapping regime case ST_2 of Hamiltonian (2.22). Results averaged over 50 disorder realizations. The dashed lines in panels **(c)** and **(d)** indicate values $\alpha_{m_2} = 0.2$ and $\alpha_\Lambda = -0.36$ respectively. The error bar in **(c)** and the light color shade in **(d)** denote the numerical error of one standard deviation in the computed slopes $\alpha_{m_2}(t)$ and $\alpha_\Lambda(t)$ respectively. Plots **(a)** and **(b)** are in log-log scale while **(c)** and **(d)** are in log-linear scale.

ST_2 exhibits characteristics of selftrapping chaos with the $m_2(t)$ evolving following a power law $m_2(t) \propto t^{\alpha_{m_2}}$ where $\alpha_{m_2} \approx 0.2$ [Figure 5.9**(c)**], a finding consistent with what was reported in Laptyeva et al. (2012) and similar to the behaviour of the $m_2(t)$ for the weak chaos regime. Also $P(t)$, as expected, remains constant at very small values.
For the finite time mLCE $\Lambda(t)$ (3.11), which was not computed in Laptyeva et al. (2012), we observe an eventual power law decay $\Lambda(t) \propto t^{\alpha_\Lambda}$ which is different from $\Lambda(t) \propto t^{-1}$ of regular dynamics. The computed exponent $\alpha_\Lambda \approx -0.36$ is close to the average $\alpha_\Lambda \approx -0.37$ observed in the weak chaos case. This shows that the chaoticity for the selftrapping case is similar to that of the weak chaos case but different from the one of strong chaos case (where $\alpha_\Lambda \approx -0.46$). The spreading to chaoticity time scale ratio R_{m_2} of (4.11) is therefore

$$R_{m_2} \sim t^{0.44},$$

since $\alpha_{m_2} = 0.2$ and $\alpha_\Lambda = -0.36$, indicating that $T_\Lambda(t) < T_{m_2}(t)$.

Deviation vector distributions

We present our findings for a representative realisation of case ST_2 in this regime, after which we give results similar to the outcomes of the DVD discussion given in the cases of weak and strong chaos.
In Figure 5.10 we show the time evolution of the normalised energy density (2.33) and DVDs (3.2). For this analysis we use the marginal energy densities

$$\xi_{l_x} = \sum_m \xi_{l,m} \qquad \text{and} \qquad \xi_{l_y} = \sum_l \xi_{l,m} \tag{5.4}$$

and

$$\xi^D_{l_x} = \sum_m \xi^D_{l,m} \qquad \text{and} \qquad \xi^D_{l_y} = \sum_l \xi^D_{l,m}. \tag{5.5}$$

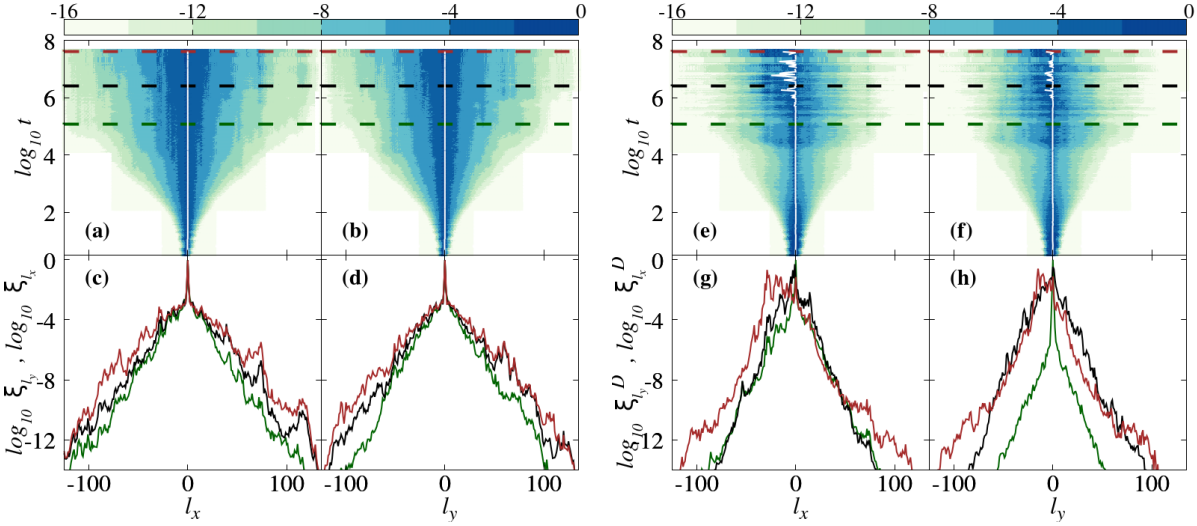

Figure 5.10: Results for the time evolution of the normalized energy distribution **(a)** $\xi_{l_x}(t)$ and **(b)** $\xi_{l_y}(t)$ (5.4) and the DVD **(e)** $\xi^D_{l_x}(t)$ and **(f)** $\xi^D_{l_y}(t)$ (5.4) for a single realisation of case ST_2. The colour scales at the top of the figure are used for colouring lattice sites according to their **(a)** $\log_{10}\xi_{l_x}(t)$, **(b)** $\log_{10}\xi_{l_y}(t)$, **(e)** $\log_{10}\xi^D_{l_x}(t)$ and **(f)** $\log_{10}\xi^D_{l_y}(t)$ values. In each of the panels **(a)**, **(b)**, **(c)** and **(d)** the white curve traces the distributions' centre. **(c)** Normalized energy distributions $\xi_{l_x}(t)$, **(d)** Normalized energy distributions $\xi_{l_y}(t)$, **(g)** DVD $\xi^D_{l_x}(t)$ and **(h)** DVD $\xi^D_{l_y}(t)$ at times $\log_{10} t = 5$ [green curve], $\log_{10} t = 6.4$ [black curve], $\log_{10} t = 7.7$ [red curve]. These times are also denoted by similarly coloured horizontal dashed lines in **(a)**, **(b)**, **(e)** and **(f)**.

The centre of the lattice has been translated to 0 in each of the two dimensions. In Figure 5.10**(a)** and **(b)** we respectively plot the time evolution of $\xi_{l_x}(t)$ (5.4) and $\xi_{l_y}(t)$ (5.4), while in **(e)** and **(f)** we show the evolution of $\xi^D_{l_x}(t)$ (5.5) and $\xi^D_{l_y}(t)$ (5.5). Once again the energy density exhibits a symmetric spreading behaviour around the mean position of the wave packet [Figure 5.10**(a)**, **(b)**, **(c)** and **(d)**] while the DVD centre fluctuates as shown in Figure 5.10**(e)**, **(f)**, **(g)** and **(h)**, within the region covered by the wave packet. Snapshots of the energy distributions at specific integration times $\log_{10} t = 5$, $\log_{10} t = 6.4$ and $\log_{10} t = 7.7$ are shown in **(c)** and **(d)** and those for the DVDs are presented in **(g)** and **(h)**. As expected of the selftrapping behaviour, there are some sites which are highly excited and this manifests in form of sharp peaks of the snapshots in panels **(c)** and **(d)**. In Figure 5.11 we present averaged results for the second moment $m_2^D(t)$ (3.4) and the participation number $P^D(t)$ (3.3) of the DVD (3.2) for the selftrapping case ST_2.
The $m_2^D(t)$ [Figure 5.11**(a)**] and $P^D(t)$ [Figure 5.11**(b)**] show a tendency to eventually become constant at very small values, indicating that the DVD eventually stops spreading and gets a pointy shape.

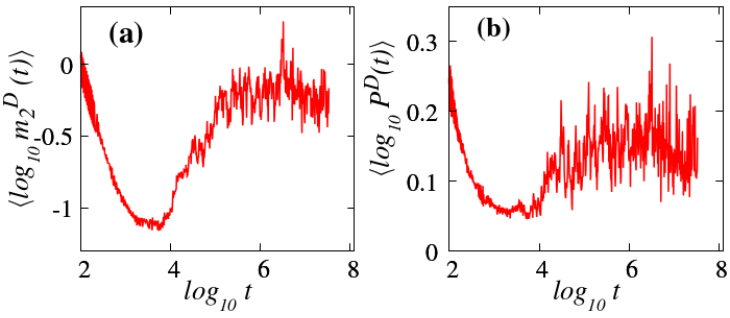

Figure 5.11: Similar to Figure 5.3 but for the selftrapping chaos spreading regime case ST_2 of Hamiltonian (2.22). Results averaged over 50 disorder realizations for the time evolution of **(a)** $m_2^D(t)$ (2.34) and **(b)** $P^D(t)$ (2.35). The plots are in log-log scale.

Figure 5.12 shows the results for the quantities **(a)** $M(t)$ (4.14), **(b)** $R(t)$ (4.15) and **(c)** $\iota^D(t)$ (4.16) computed for the DVD (red curves) and energy distribution (blue curves).

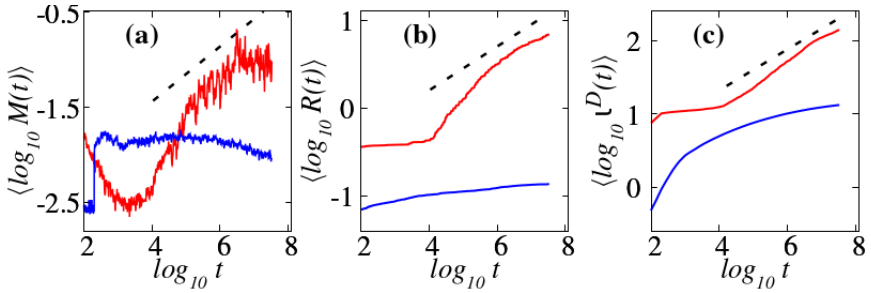

Figure 5.12: Similar to Figure 5.4 but for the selftrapping chaos regime case ST_2 of Hamiltonian (2.22). Results for the time evolution of **(a)** $M(t)$ (4.14), **(b)** $R(t)$ (4.15) and **(c)** $\iota^D(t)$ (4.16) for the DVD (red curves) and energy distribution (blue curves). The straight dashed lines guide the eye for slopes **(a)** 0.29, **(b)** 0.25 and **(c)** 0.28. The panels are in log-log scale.

The results show that mean position fluctuations for the energy distribution are of smaller magnitude compared to those of the DVD mean position. This result for the comparison of DVD and energy distribution mean position fluctuations, which is not different from the behaviour in both the weak and strong chaos cases, confirms the behaviour we see from the representative distribution plots in Figure 5.10 about meandering of mean positions.

The straight dashed lines correspond to slopes 0.29 [Figure 5.12**(a)**], 0.25 [Figure 5.12**(b)**] and 0.28 [Figure 5.12**(c)**] observed in the case of weak chaos in Section 5.3. The DVD quantities $R(t)$, $M(t)$ and $\iota^D(t)$ in this case continue to increase although they eventually grow away from and smaller than what was observed for the weak chaos regime, showing that the DVD mean position fluctuations in the selftrapping regime eventually grow slower than those in the weak chaos case.

5.6 Summary

We studied the dynamical behaviour of the 2D DKG model (2.22) in the weak, strong and selftrapping chaotic regimes. For a number of chaotic parameter cases, we obtained statistical results from approximately 50 disorder realizations in each case. Like for the case of the 1D DKG model (2.19) studied in Chapter 4, we computed the finite time mLCE $\Lambda(t)$ (3.11) and verified that the level of chaoticity of the propagating wave packets decreases in time with the system maintaining its chaotic nature without any tendency of the dynamics to crossover to regular behaviour. $\Lambda(t)$ follows a power law $\Lambda(t) \propto t^{\alpha_\Lambda}$ characterized by $\alpha_\Lambda \neq -1$. We found that in the weak, strong and selftrapping chaos regimes $\alpha_\Lambda \approx -0.37$, $\alpha_\Lambda \approx -0.46$ and $\alpha_\Lambda \approx -0.36$ respectively. The wave packet gets more chaotic at a rate higher than its spreading since for all considered regimes of chaos, the chaoticity time scale $T_\Lambda(t)$ (4.4) always remains smaller than the spreading time scales $T_{m_2}(t)$ (4.7) and or $T_P(t)$ (4.9).

The DVD (3.2) kept a localized, pointy shape with small values of the participation number $P^D(t)$ (3.3) compared to $P(t)$ (2.35) of the normalised energy distribution (2.33). However, the DVD centre fluctuations amplitude for all weak, strong and selftrapping chaos cases increased with time as it (DVD centre) moved to regions inside the spreading wave packet. Therefore the quantities $R(t)$ (4.15), $M(t)$ (4.14) and $\iota^D(t)$ (4.16) which estimate the DVD centre fluctuations increased with time following power laws $R(t) \propto t^{0.25}$, $M(t) \propto t^{0.29}$ and $\iota^D(t) \propto t^{0.28}$ in the weak chaos regime. For the strong chaos case on the other hand, $M(t)$ and $\iota^D(t)$ grow with higher non constant exponents as $M(t) \propto t^{0.37}$ and $\iota^D(t) \propto t^{0.39}$ showing that the chaotic seeds spread faster with the DVD covering wider areas compared to the weak chaos case. Just like in the weak chaos case, $R(t) \propto t^{0.25}$ for the strong chaos regime, showing that the growth rate of the fluctuation amplitude of the DVD centre is similar for both regimes but with higher amplitudes observed for the strong chaos case.

In summary, we showed numerically for the 2D DKG model (2.22) that (a) the strength of chaotic dynamics of a wave packet decreases in time but it does not crossover to regular dynamics, (b) chaotization is due to the chaotic seeds meandering in the wave packet and (c) the characteristics of chaos evolution show a clear distinction between weak and strong chaos behaviour.

Chapter 6

Summary and Conclusions

In this thesis, the study of energy propagation in disordered nonlinear Hamiltonian systems of many degrees of freedom was discussed. Firstly, normal mode (NM) properties for a 1D modified Klein-Gordon model (2.36) with parameters D, which allows the system to be ordered for $D = 0$ and increase disorder in the system up to when $D = 1/2$, and $\mathcal{W}$ which regulates the contribution of nearest neighbour interactions, were studied. For a fixed $\mathcal{W} = 4$, the NMs become less spatially extended [with spatial extent measured using the localization volume V (2.7) and participation number P (2.8)] in the lattice as values of D increase towards $1/2$ following the laws $P \propto D^{-2}$ and $V \propto D^{-2}$ and a participation number fluctuation correction scaling given by $V \approx 2.6P$. Therefore, the NMs of linear systems with strong enough disorder only extend to a finite number of sites and so, an initially localized wave packet will not spread to infinitely many sites. Nonlinearity, however, introduces chaos to the system and destroys AL as the NMs interact with each other. Spreading energy distribution characteristics for different dynamical behaviours in nonlinear disordered lattices including the weak, strong and selftrapping regimes of chaos for $D = 1/2$ were theoretically explained using the DDNLS system (2.15).

In chapter 3, numerical techniques for investigating the dynamical behaviour of one- and two-dimensional Hamiltonian chains were discussed. These included aspects of deviation vector dynamics, the corresponding DVDs, Lyapunov characteristic exponents, the variational equations and integration methods. For both the $1D$ and $2D$ DKG models, an initial deviation vector where all coordinates of both the positions and momenta components are zero except for the coordinates which just cover the degrees of freedom where the initial excitation takes place, gives the fastest convergence of the DVD behaviour [monitored using finite time mLCE $\Lambda(t)$ and DVD participation number $P^D(t)$] to it's asymptotic state compared to other forms of initial deviation vector. A number of existing integrators were described and higher order symplectic schemes constructed through composition techniques. The computational efficiency of these schemes in integrating the equations of motion [(2.21) and (2.24)] and the corresponding variational equations (3.9) of the one (2.19) and two (2.22) spatial dimension DKG systems was analysed. The performance of the integrators was found to be independent of the spatial dimensions of the model being investigated, as the rank in performance over both the 1D and 2D DKG models was the same. The order four SIs $ABA864$ and $ABAH864$, the order six SIs $s9SABA_26$, $SABA_2Y6$ and $ABA864Y6$, gave the best performance at an absolute relative energy error $e_r \approx 10^{-5}$ with $ABA864$ [Blanes et al. (2013)] requiring the least CPU time in both models. At a high accuracy level $e_r \approx 10^{-8}$, the order six SIs $s11ABA82\_6$, $SABA_2Y6$ and $s9ABA82\_6$ and the order eight SIs $s15ABA82\_8$ and $s19ABA82\_8$ were found to be the most computationally efficient schemes.

In chapters 4 and 5, systematic numerical calculations of finite time maximum Lyapunov characteristic exponents $\Lambda(t)$ (3.11) were presented for respectively the 1D and 2D disordered nonlinear Hamiltonian lattices with the DKG models (2.19) and (2.22) as prototype representative systems. The dynamical behaviour in the spreading wave packet was found to remain chaotic for the entire duration of the simulation. In one spatial dimension, $\Lambda(t)$ evolved following the laws $\Lambda(t) \propto t^{-0.25}$, $\Lambda(t) \propto t^{-0.32}$ and $\Lambda(t) \propto t^{-0.26}$ for respectively the weak, strong and selftrapping regimes of chaos. There was however a slowing down in the chaotic behaviour for the two spatial dimensions system with $\Lambda(t)$ evolving as $\Lambda(t) \propto t^{-0.37}$, $\Lambda(t) \propto t^{-0.46}$ and $\Lambda(t) \propto t^{-0.36}$ for respectively the weak, strong and selftrapping regimes of chaos. For all initial system configurations presented in the $1D$ and $2D$ models, there was no signs of a tendency by the dynamics to slow down and cross to ordered motion which is characterised by $\Lambda(t) \propto t^{-1}$. The chaoticity timescale $T_\Lambda(t)$ (4.4) was found to be shorter than the spreading timescales $T_{m_2}(t)$ (4.7) and/or $T_P(t)$ (4.9) with the corresponding chaoticity-spreading timescale ratios $R_{m_2}(t)$ and/or $R_P(t)$ (4.11) diverging as a power law. Thus a confirmation of the subdiffusive spreading theories assumption necessitating chaos to be persistent and fast enough in disordered nonlinear lattices. Additionally, computations of the $m_2(t)$, (2.30) and (2.34), showed that the wave packet continues spreading for the different chaos regimes in the one and two spatial dimensions models, contrary to the reports of Johansson et al. (2010) and Aubry (2011).

For all initial conditions considered in the $1D$ and $2D$ models, the energy density was observed to spread evenly with time about the distribution centre while the DVD remained localized with it's peak position meandering to cover distances approximately equal to the energy distribution width. As estimators for fluctuation amplitudes of the DVD mean position, quantities $M(t)$ (4.14) [estimates the mean deviation of the DVD centre in a fixed epoch progressively in time], $R(t)$ (4.15) [estimates the maximum fluctuation amplitudes of the DVD mean position] and $\iota^D(t)$ (4.16) [estimates the magnitude of the total displacement of the DVD centre], were introduced. The amplitude of the fluctuations increased in time for all regimes of chaos with characteristic power law growths $R(t) \propto t^{0.24}$, $M(t) \propto t^{0.25}$ and $\iota^D(t) \propto t^{0.28}$ in the weak and selftrapping chaos regimes of the 1D DKG model. The strong chaos regime however, exhibited faster growth of these quantities with an eventual tendency to settle at the same power laws as the weak chaos regime, a good indication of the transient nature of the strong to weak chaos behaviour. In the regime of weak chaos for the 2D DKG model, $R(t)$ and $\iota^D(t)$ grow at rates similar to those observed in the same chaotic regime for the 1D DKG system. $M(t)$ on the other hand grows faster for the 2D DKG model (2.22) following the laws $M(t) \propto t^{0.29}$ for the weak chaos case and $M(t) \propto t^{0.37}$ for the strong chaos case, an indication that fluctuations of the DVD mean position in small time intervals of the dynamics are stronger in two dimensions compared to one dimension. The total distance covered by the fluctuations of the DVD mean position, which is estimated using $\iota^D(t)$, was found to have a faster growth in the strong chaos case of two dimensions compared to one dimension. For both models, the quantities $M(t)$, $R(t)$, and $\iota^D(t)$ keep growing up to the largest simulation times, showing no sign of becoming constant as would be for regular motion. This verifies another subdiffusive spreading theories assumption which requires the seeds of chaos to meander fast enough through the wave packet of a disordered Hamiltonian lattice thereby ensuring its chaotization.

6.1 Outlook

In this work, the chaotic behaviour of disordered nonlinear lattices has been discussed using a typical example of the DKG models with quartic nonlinearity. Our results agree with the findings for the quartic discrete nonlinear Schrödinger equations (which have two conserved quantities) presented in Senyange et al. (2018) and Many Manda et al. (2020), thereby enabling a generalization of this behaviour to nonlinear disordered lattices. However, there are some open questions that have emerged as a follow up of this work. We mention here some of them. Our first example is the question on a thorough analytical and numerical investigation of linear NM properties in models of 2D spatial dimensions starting with the purely ordered case and gradually increasing the systems' heterogeneity to get a fully disordered model. Further more, how the dynamical behaviour of the models (1D and 2D) is affected by the width of the interval containing on-site potentials. That is to say, how the dynamics of nonlinear disordered models changes for DKG model disorder selected from an interval $[1-D, 1+D]$ where D takes on different values, i.e. $D \in (0, 1/2]$. The second open question is how the findings of this work are affected when the 1D and 2D models have a generalised (including fractional) nonlinearity. A good starting point is the investigation of Skokos and Flach (2010) and Laptyeva et al. (2012) where a theoretical and numerical dynamical study of respectively the generalised 1D and 2D Klein-Gordon models is reported. In both papers, it was shown that the wave packet continues to grow with the second moment following a power law. However there is need for further inquiry on the time evolution of chaos for these models compared to the presentation of Chapters 4 and 5.

Appendix A

Symplectic integration of the DKG models

We present here the explicit form of the variational equations (3.9), operators $e^{\tau L_{T_\mathcal{V}}}$ and $e^{\tau L_{V_\mathcal{V}}}$ used for the time propagation of a deviation vector with initial conditions $(\mathbf{q}, \mathbf{p}, \delta\mathbf{q}, \delta\mathbf{p})$ at time t to their final values $(\mathbf{q}', \mathbf{p}', \delta\mathbf{q}', \delta\mathbf{p}')$ at time $t+\tau$ for Hamiltonians (2.19) and (2.22) TDH (3.10).

A.1 The 1D DKG model

The variational equations (3.3.2) of the 1D DKG model (2.19) are

$$\begin{aligned}
\frac{dq_i}{dt} &= p_i, \quad \text{for } 1 \le i \le N \\
\frac{dp_1}{dt} &= -\left[\epsilon_1 q_1 + q_1^3 + \frac{1}{W}(2q_1 - q_2)\right] \\
\frac{dp_i}{dt} &= -\left[\epsilon_i q_i + q_i^3 + \frac{1}{W}(2q_i - q_{i-1} - q_{i+1})\right], \quad \text{for } 2 \le i \le N-1 \\
\frac{dp_N}{dt} &= -\left[\epsilon_N q_N + q_N^3 + \frac{1}{W}(2q_N - q_{N-1})\right] \\
\frac{d\delta q_i}{dt} &= \delta p_i, \quad \text{for } 1 \le i \le N \\
\frac{d\delta p_1}{dt} &= -\left[\delta q_1\left(\epsilon_1 + 3q_1^2\right) + \frac{1}{W}(2\delta q_1 - \delta q_2)\right] \\
\frac{d\delta p_i}{dt} &= -\left[\delta q_i\left(\epsilon_i + 3q_i^2\right) + \frac{1}{W}(2\delta q_i - \delta q_{i-1} - \delta q_{i+1})\right], \quad \text{for } 2 \le i \le N-1 \\
\frac{d\delta p_N}{dt} &= -\left[\delta q_N\left(\epsilon_N + 3q_N^2\right) + \frac{1}{W}(2\delta q_N - \delta q_{N-1})\right].
\end{aligned} \tag{A.1}$$

In order to implement the SIs discussed in Section 3.3 for the integration of equations (A.1) we split Hamiltonian (2.19) in two integrable parts

$$T(\mathbf{p}) = \sum_{i=1}^{N} \frac{p_i^2}{2}, \quad V(\mathbf{q}) = \sum_{i=1}^{N}\left[\frac{\epsilon_i}{2}q_i^2 + \frac{q_i^4}{4} + \frac{1}{2W}(q_{i+1} - q_i)^2\right], \tag{A.2}$$

i.e. respectively the kinetic and potential energies respectively of the system. The solution of the variational equations for integrable Hamiltonians T and V are obtained through the action of the operators

$$e^{\tau L_{V_\mathcal{V}}} : \begin{cases} q_i' &= q_i + \tau p_i \\ p_i' &= p_i \\ \delta q_i' &= \delta q_i + \tau \delta p_i \\ \delta p_i' &= \delta p_i \end{cases}, \text{ for } 1 \leq i \leq N, \tag{A.3}$$

and

$$e^{\tau L_{T_\mathcal{V}}} : \begin{cases} q_i' &= q_i, \text{ for } 1 \leq i \leq N \\ p_1' &= p_1 - \tau \left[\epsilon_1 q_1 + q_1^3 + \frac{1}{W}(2q_1 - q_2) \right] \\ p_i' &= p_i - \tau \left[\epsilon_i q_i + q_i^3 + \frac{1}{W}(2q_i - q_{i-1} - q_{i+1}) \right], \text{ for } 2 \leq i \leq N-1 \\ p_N' &= p_N - \tau \left[\epsilon_N q_N + q_N^3 + \frac{1}{W}(2q_N - q_{N-1}) \right] \\ \delta q_i' &= \delta q_i, \text{ for } 1 \leq i \leq N \\ \delta p_1' &= \delta p_1 - \tau \left[\delta q_1 \left(\epsilon_1 + 3q_1^2 \right) + \frac{1}{W}(2\delta q_1 - \delta q_2) \right] \\ \delta p_i' &= \delta p_i - \tau \left[\delta q_i \left(\epsilon_i + 3q_i^2 \right) + \frac{1}{W}(2\delta q_i - \delta q_{i-1} - \delta q_{i+1}) \right], \text{ for } 2 \leq i \leq N-1 \\ \delta p_N' &= \delta p_N - \tau \left[\delta q_N \left(\epsilon_N + 3q_N^2 \right) + \frac{1}{W}(2\delta q_N - \delta q_{N-1}) \right]. \end{cases} \tag{A.4}$$

A.2 The 2D DKG model

The 2D DKG Hamiltonian (2.22) can also be written as the sum of the kinetic energy $T(\mathbf{p})$ and the potential energy $V(\mathbf{q})$. The propagation operators for the solution of the variational equations are given by the expressions

$$e^{\tau L_{V_\mathcal{V}}} : \begin{cases} q_{i,j}' &= q_{i,j} + \tau p_{i,j} \\ p_{i,j}' &= p_{i,j} \\ \delta q_{i,j}' &= \delta q_{i,j} + \tau \delta p_{i,j} \\ \delta p_{i,j}' &= \delta p_{i,j} \end{cases}, \text{ for } 1 \leq i \leq N,\ 1 \leq j \leq M, \tag{A.5}$$

and

$$
e^{\tau L_{T_{\mathcal{V}}}}:\begin{cases}
q'_{i,j} &= q_{i,j}, \ \text{for } 1\le i\le N,\ 1\le j\le M\\
p'_{1,1} &= p_{1,1}-\tau\left[\epsilon_{1,1}q_{1,1}+q_{1,1}^3+\frac{1}{W}\left(4q_{1,1}-q_{2,1}-q_{1,2}\right)\right]\\
p'_{1,M} &= p_{1,M}-\tau\left[\epsilon_{1,M}q_{1,M}+q_{1,M}^3+\frac{1}{W}\left(4q_{1,M}-q_{1,M-1}-q_{2,M}\right)\right]\\
p'_{N,1} &= p_{N,1}-\tau\left[\epsilon_{N,1}q_{N,1}+q_{N,1}^3+\frac{1}{W}\left(4q_{N,1}-q_{N-1,1}-q_{N,2}\right)\right]\\
p'_{N,M} &= p_{N,M}-\tau\left[\epsilon_{N,M}q_{N,M}+q_{N,M}^3+\frac{1}{W}\left(4q_{N,M}-q_{N-1,M}-q_{N,M-1}\right)\right]\\
p'_{i,j} &= p_{i,j}-\tau\left[\epsilon_{i,j}q_{i,j}+q_{i,j}^3+\frac{1}{W}\left(4q_{i,j}-q_{i-1,j}-q_{i,j-1}\ -q_{i+1,j}-q_{i,j+1}\right)\right],\\
&\quad \text{for } 2\le i\le N-1,\ 2\le j\le M-1\\
p'_{i,1} &= p_{i,1}-\tau\left[\epsilon_{i,1}q_{i,1}+q_{i,1}^3+\frac{1}{W}\left(4q_{i,1}-q_{i-1,1}-q_{i+1,1}\ -q_{i,2}\right)\right],\\
&\quad \text{for } 2\le i\le N-1\\
p'_{i,M} &= p_{i,M}-\tau\left[\epsilon_{i,M}q_{i,M}+q_{i,M}^3+\frac{1}{W}\left(4q_{i,M}-q_{i-1,M}-q_{i,M-1}\ -q_{i+1,M}\right)\right],\\
&\quad \text{for } 2\le i\le N-1\\
p'_{1,j} &= p_{1,j}-\tau\left[\epsilon_{1,j}q_{1,j}+q_{1,j}^3+\frac{1}{W}\left(4q_{1,j}-q_{1,j-1}-q_{2,j}\ -q_{1,j+1}\right)\right],\\
&\quad \text{for } 2\le j\le M-1\\
p'_{N,j} &= p_{N,j}-\tau\left[\epsilon_{N,j}q_{N,j}+q_{N,j}^3+\frac{1}{W}\left(4q_{N,j}-q_{N-1,j}-q_{N,j-1}\ -q_{N,j+1}\right)\right],\\
&\quad \text{for } 2\le j\le M-1\\
\delta q'_{i,j} &= \delta q_{i,j}, \ \text{for } 1\le i\le N,\ 1\le j\le M\\
\delta p'_{1,1} &= \delta p_{1,1}-\tau\left[\delta q_{1,1}\left(\epsilon_{1,1}+3q_{1,1}^2\right)+\frac{1}{W}\left(4\delta q_{1,1}-\delta q_{2,1}-\delta q_{1,2}\right)\right]\\
\delta p'_{1,M} &= \delta p_{1,M}-\tau\left[\delta q_{1,M}\left(\epsilon_{1,M}+3q_{1,M}^2\right)+\frac{1}{W}\left(4\delta q_{1,M}-\delta q_{1,M-1}-\delta q_{2,M}\right)\right]\\
\delta p'_{N,1} &= \delta p_{N,1}-\tau\left[\delta q_{N,1}\left(\epsilon_{N,1}+3q_{N,1}^2\right)+\frac{1}{W}\left(4\delta q_{N,1}-\delta q_{N-1,1}-\delta q_{N,2}\right)\right]\\
\delta p'_{N,M} &= \delta p_{N,M}-\tau\left[\delta q_{N,M}\left(\epsilon_{N,M}+3q_{N,M}^2\right)+\frac{1}{W}\left(4\delta q_{N,M}-\delta q_{N-1,M}-\delta q_{N,M-1}\right)\right]\\
\delta p'_{i,j} &= \delta p_{i,j}-\tau\left[\delta q_{i,j}\left(\epsilon_{i,j}+3q_{i,j}^2\right)+\frac{1}{W}\left(4\delta q_{i,j}-\delta q_{i-1,j}-\delta q_{i,j-1}\ -\delta q_{i+1,j}-\delta q_{i,j+1}\right)\right],\\
&\quad \text{for } 2\le i\le N-1,\ 2\le j\le M-1\\
\delta p'_{i,1} &= \delta p_{i,1}-\tau\left[\delta q_{i,1}\left(\epsilon_{i,1}+3q_{i,1}^2\right)+\frac{1}{W}\left(4\delta q_{i,1}-\delta q_{i-1,1}-\delta q_{i+1,1}\ -\delta q_{i,2}\right)\right],\\
&\quad \text{for } 2\le i\le N-1\\
\delta p'_{i,M} &= \delta p_{i,M}-\tau\left[\delta q_{i,M}\left(\epsilon_{i,M}+3q_{i,M}^2\right)+\frac{1}{W}\left(4\delta q_{i,M}-\delta q_{i-1,M}-\delta q_{i,M-1}\ -\delta q_{i+1,M}\right)\right],\\
&\quad \text{for } 2\le i\le N-1\\
\delta p'_{1,j} &= \delta p_{1,j}-\tau\left[\delta q_{1,j}\left(\epsilon_{1,j}+3q_{1,j}^2\right)+\frac{1}{W}\left(4\delta q_{1,j}-\delta q_{1,j-1}-\delta q_{2,j}\ -\delta q_{1,j+1}\right)\right],\\
&\quad \text{for } 2\le j\le M-1\\
\delta p'_{N,j} &= \delta p_{N,j}-\tau\left[\delta q_{N,j}\left(\epsilon_{N,j}+3q_{N,j}^2\right)+\frac{1}{W}\left(4\delta q_{N,j}-\delta q_{N-1,j}-\delta q_{N,j-1}\ -\delta q_{N,j+1}\right)\right],\\
&\quad \text{for } 2\le j\le M-1.
\end{cases}
\tag{A.6}
$$

Bibliography

M. J. Ablowitz and P. Clarkson. Solitons, nonlinear evolution equations and inverse scattering. *Physica D: Nonlinear Phenomena*, 18(1-3):223–241, 1991.

M. J. Ablowitz and J. F. Ladik. Nonlinear differential–difference equations and Fourier analysis. *Journal of Mathematical Physics*, 17(6):1011–1018, 1976.

V. Achilleos, G. Theocharis, and C. Skokos. Energy transport in one-dimensional disordered granular solids. *Physical Review E*, 93(2):1–9, 2016.

V. Achilleos, G. Theocharis, and C. Skokos. Chaos and Anderson-like localization in polydisperse granular chains. *Physical Review E*, 97(4):1–8, 2018.

E. Akkermans and G. Montambaux. *Mesoscopic Physics of Electrons and Photons*. Number 1. Cambridge University Press, New York, 2007.

G. Amati and T. Schilling. Structural localization in the classical and quantum Fermi-Pasta-Ulam model. *Chaos*, 30(3), 2020.

W. Anderson, P. Absence of Diffusion in Certain Random Lattices. *Physical Review*, 109 (5):1492–1506, 1958.

C. G. Antonopoulos, T. Bountis, C. Skokos, and L. Drossos. Complex statistics and diffusion in nonlinear disordered particle chains. *Chaos*, 24(2), 2014.

C. G. Antonopoulos, C. Skokos, T. Bountis, and S. Flach. Analyzing chaos in higher order disordered quartic-sextic Klein-Gordon lattices using q-statistics. *Chaos, Solitons and Fractals*, 104:129–134, 2017.

S. Aubry. KAM tori and absence of diffusion of a wave-packet in the 1D random dnls model. *International Journal of Bifurcation and Chaos*, 21(8):2125–2145, 2011.

S. Aubry and G. Andre. Analyticity breaking and Anderson localization in incommensurate lattices. *Annals of the Israel Physical Society*, 3, 1980.

D. M. Basko. Weak chaos in the disordered nonlinear Schrödinger chain: Destruction of Anderson localization by Arnold diffusion. *Annals of Physics*, 326(7):1577–1655, 2011.

D. M. Basko. Local nature and scaling of chaos in weakly nonlinear disordered chains. *Physical Review E*, 86(3):1–10, 2012.

D. M. Basko. Kinetic theory of nonlinear diffusion in a weakly disordered nonlinear Schrödinger chain in the regime of homogeneous chaos. *Physical Review E*, 89(2):1–22, 2014.

G. Benettin, L. Galgani, and J.-M. Strelcyn. Kolmogorov entropy and numerical experiments. *Physical Review A*, 14(6), 1976.

G. Benettin, L. Galgani, A. Giorgilli, and J.-M. Strelcyn. All Lyapunov Characteristic Numbers are Effectively Computable. *Comptes Rendus Hebdomadaires des Séances de l'Académie Des Sciences, Série A*, 286(9):431–433, 1978.

G. Benettin, L. Galgani, A. Giorgilli, and J.-M. M. Strelcyn. Lyapunov Characteristic Exponents for smooth dynamical systems and for hamiltonian systems; A method for computing all of them. Part 2: Numerical application. *Meccanica*, 15(1):21–30, 1980a.

G. Benettin, L. Galgani, A. Giorgilli, and J.-M. M. Strelcyn. Lyapunov Characteristic Exponents for smooth dynamical systems and for hamiltonian systems; A method for computing all of them. Part 2: Numerical application. *Meccanica*, 15(1):21–30, 1980b.

J. Billy, V. Josse, Z. Zuo, A. Bernard, B. Hambrecht, P. Lugan, D. Clément, L. Sanchez-palencia, P. Bouyer, J. Billy, V. Josse, Z. Zuo, A. Bernard, and B. Hambrecht. Direct observation of Anderson localization of matter-waves in a controlled disorder. *Nature*, 453(7197):891–4, 2008.

S. Blanes, F. Casas, A. Farrés, J. Laskar, J. Makazaga, and A. Murua. New families of symplectic splitting methods for numerical integration in dynamical astronomy. *Applied Numerical Mathematics*, 68:58–72, 2013.

J. D. Bodyfelt, T. V. Laptyeva, G. Gligoric, D. O. Krimer, C. Skokos, and S. Flach. Wave interactions in localizing media-a coin with many faces. *International Journal Of Bifurcation And Chaos*, 21(08):2107, 2011a.

J. D. Bodyfelt, T. V. Laptyeva, C. Skokos, D. O. Krimer, and S. Flach. Nonlinear waves in disordered chains: Probing the limits of chaos and spreading. *Physical Review E - Statistical, Nonlinear, and Soft Matter Physics*, 84(1):1–10, 2011b.

J. Borowska and L. Łacińska. Eigenvalues of 2-tridiagonal Toeplitz matrix. *Journal of Applied Mathematics and Computational Mechanics*, 14(4):11–17, 2015.

O. Braun and Y. Kivshar, S. Dynamical phase diagram of the dc-driven underdamped Frenkel-Kontorova chain. *Physics Reports*, 306:1 – 108, 1998.

O. M. Braun and Y. S. Kivshar. *The Frenkel-Kontorova Model: Concepts, Methods, and Applications*. Springer-Verlag Berlin Heidelberg, New York, 2004.

P. Butera, L. Galgani, A. Giorgilli, A. Tagliani, and H. Sabata. Stochasticity thresholds in a lattice field theory. *Il Nuovo Cimento B Series 11*, 59(1):81–86, 1980.

D. K. Campbell, P. Rosenau, and G. M. Zaslavsky. Introduction : The Fermi – Pasta – Ulam problem — The first fifty years. 015101(2005), 2012.

A. A. Chabanov, M. Stoytchev, and A. Z. Genack. Signatures of photon localization. *Nature*, 404:850–852, 2000.

N. Cherroret. A self-consistent theory of localization in nonlinear random media. *Journal of Physics: Condensed Matter*, 29(024002), 2017.

C. Chin, R. Grimm, P. Julienne, and E. Tiesinga. Feshbach resonances in ultracold gases. *Reviews of Modern Physics*, 82(2):1225–1286, 2010.

D. Clément, A. F. Varón, M. Hugbart, J. A. Retter, P. Bouyer, L. Sanchez-Palencia, D. M. Gangardt, G. V. Shlyapnikov, and A. Aspect. Suppression of transport of an interacting elongated Bose-Einstein condensate in a random potential. *Physical Review Letters*, 95(17):1–4, 2005.

W. S. Cleveland. Robust locally weighted regression and smoothing scatterplots. *Journal of the American Statistical Association*, 74(368):829–836, 1979.

W. S. Cleveland and S. J. Devlin. Locally weighted regression: An approach to regression analysis by local fitting. *Journal of the American Statistical Association*, 83(403): 596–610, 1988.

L. A. Cobus, S. E. Skipetrov, A. Aubry, B. A. Van Tiggelen, A. Derode, and J. H. Page. Anderson Mobility Gap Probed by Dynamic Coherent Backscattering. *Physical Review Letters*, 116(19):1–5, 2016.

A. Crisanti, G. Paladin, and A. Vulpiani. *Products of Random Matrices in statistical physics*. Springer-Verlag Berlin Heidelberg, Barcelona, 1 edition, 1993.

L. Cruzeiro-Hansson, P. L. Christiansen, and J. N. Elgin. Comment on Self-trapping on a dimer: Time-dependent solutions of a discrete nonlinear Schrödinger equation. *Physical Review B*, 37(13):7896–7897, 1986.

C. M. Da Fonseca and V. Kowalenko. Eigenpairs of a family of tridiagonal matrices: three decades later. *Acta Mathematica Hungarica*, 2019.

F. Dalfovo, S. Giorgini, L. P. Pitaevskii, and S. Stringari. Theory of Bose-Einstein condensation in trapped gases. *Reviews of Modern Physics*, 71(3):463–512, 1999.

R. Dalichaouch, J. P. Armstrong, S. Schultz, P. M. Platzman, and S. L. McCall. Microwave localization by two-dimensional random scattering. *Nature*, 354:56–58, 1991.

C. Danieli, T. Mithun, Y. Kati, D. K. Campbell, and S. Flach. Dynamical glass in weakly nonintegrable Klein-Gordon chains. *Physical Review E*, 100(3):1–13, 2019.

T. Dauxois, M. Peyrard, and A. R. Bishop. Dynamics and thermodynamics. *Physical Review E*, 47(1), 1993.

U. Dehlinger. Zur Theorie der Rekristallisation reiner Metalle. *Ann. Phys. (Leipzig)*, 2 (749):749, 1929.

B. Deissler, M. Zaccanti, G. Roati, C. D'Errico, M. Fattori, M. Modugno, G. Modugno, and M. Inguscio. Delocalization of a disordered bosonic system by repulsive interactions. *Nature Physics*, 6(5):354–358, 2010.

A. Dhar and K. Saito. Heat conduction in the disordered Fermi-Pasta-Ulam chain. *Physical Review E - Statistical, Nonlinear, and Soft Matter Physics*, 78(6):1–4, dec 2008.

E. E. Edwards, M. Beeler, T. Hong, and S. L. Rolston. Adiabaticity and localization in one-dimensional incommensurate lattices. *Physical Review Letters*, 101(26):1–4, 2008.

J. C. Eilbeck and M. Johansson. The discrete nonlinear SchrÖdinger equation - 20 years on. *Journal of Chemical Information and Modeling*, 53(9):1689–1699, 2003.

J. C. Eilbeck, P. S. Lomdahl, and A. C. Scott. The discrete self-trapping equation. *Physica D: Nonlinear Phenomena*, 16(3):318–338, 1985.

L. Ermann and D. L. Shepelyansky. Destruction of Anderson localization by nonlinearity in kicked rotator at different effective dimensions. *Journal of Physics A: Mathematical and Theoretical*, 47:335101 (9pp), 2014.

F. Evers and A. D. Mirlin. Anderson transitions. *Reviews of Modern Physics*, 80(4): 1355–1417, 2008.

A. Farrés, J. Laskar, S. Blanes, F. Casas, J. Makazaga, A. Murua, and S. Blanes. High precision symplectic integrators for the Solar System. *Celestial Mechanics and Dynamical Astronomy*, 116(2):141–174, 2013.

E. Fermi, J. Pasta, S. Ulam, and M. Tsingou. Studies of non linear problems, Technical Report. (May), 1955.

A. T. Filippov. *The Versatile Soliton*, volume 85. Birkhauser Boston, New York, 2000.

S. Flach. Spreading of waves in nonlinear disordered media. *Chemical Physics*, 375(2-3): 548–556, oct 2010.

S. Flach and A. V. Gorbach. Discrete breathers - Advances in theory and applications. *Physics Reports*, 467(1-3):1–116, 2008.

S. Flach and C. R. Willis. Discrete breathers. *Physica D: Nonlinear Phenomena*, 127 (1-2):61–72, 1999.

S. Flach, D. O. Krimer, and C. Skokos. Erratum: Universal spreading of wave packets in disordered nonlinear systems [Phys. Rev. Lett. 102, 024101 (2009)]. *Physical Review Letters*, 102(20):209903, 2009a.

S. Flach, D. O. Krimer, and C. Skokos. Universal spreading of wave packets in disordered nonlinear systems. *Physical Review Letters*, 102(2):1–4, 2009b.

S. Flach, X. Antoine, R. Duboseq, S. De Bievre, F. Genould, S. Rota Nodari, and F. Marcia. *Nonlinear Optical and Atomic Systems: An interface of Physics and Mathematics*. Springer International Publishing, 2015.

J. Ford. The Fermi-Pasta-Ulam problem: Paradox turns discovery. *Physics Reports*, 213 (5):271–310, 1992.

E. Forest and R. D. Ruth. Fourth-order symplectic integration*. *Physica D*, 43:105–117, 1990.

C. Fort, V. Guarrera, M. Modugno, L. Fallani, J. E. Lye, D. S. Wiersma, and M. Inguscio. Effect of Optical Disorder and Single Defects on the Expansion of a Bose-Einstein Condensate in a One-Dimensional Waveguide. *Physical Review Letters*, 95(17):1–4, 2005.

I. Freund. Joseph W. Goodman: Speckle Phenomena in Optics: Theory and Applications. *Journal of Statistical Physics*, 130(2):413–414, 2007.

F. Fucito, F. Marchesoni, E. Marinari, G. Parisi, L. Peliti, S. Ruffo, and A. Vulpiani. Approach to equilibrium in a chain of nonlinear oscillators. *Journal de physique Paris*, 43(5):707–713, 1982.

I. García-Mata and D. L. Shepelyansky. Delocalization induced by nonlinearity in systems with disorder. *Physical Review E*, 79(2):1–9, 2009.

E. Gerlach and C. Skokos. Comparing the efficiency of numerical techniques for the integration of variational equations. *Discrete and Continuous Dynamical Systems-Series A*, (SUPPL.):475–484, 2011.

E. Gerlach, S. Eggl, and C. Skokos. Efficient integration of the variational equations of multidimensional Hamiltonian systems: Application to the Fermi–Pasta–Ulam lattice. *International Journal of Bifurcation and Chaos*, 22(09):1250216, 2012.

V. S. Gerschgorin. On the demarcation of the eigenvalues of a matrix. *Bulletin de l Acad emiedes Sciences de l URSS*, 1(6):749–754, 1931.

A. Giorgilli, S. Paleari, and T. Penati. An extensive adiabatic invariant for the Klein–Gordon model in the thermodynamic limit. *Annales Henri Poincare*, 16(4): 897–959, 2015.

I. Gkolias. Chaos in 1-Dimensional Nonlinear Disordered Lattices. *Masters Thesis*, (September), 2013.

J. W. Goossens, H. Hafermann, and Y. Jaouën. Experimental realization of Fermi-Pasta-Ulam-Tsingou recurrence in a long-haul optical fiber transmission system. *Scientific Reports*, 9(1):1–11, 2019.

L. Guidoni, C. Triché, P. Verkerk, and G. Grynberg. Quasiperiodic optical lattices. *Physical Review Letters*, 79(18):3363–3366, 1997.

E. Hairer, C. Lubich, and G. Wanner. *Geometric Numerical Integration*. Springer-Verlag Berlin Heidelberg, New York, 2001.

P. G. Harper. Single band motion of conduction electrons in a uniform magnetic field. *Proceedings of the Physical Society. Section A*, 68(10):874–878, 1955.

M. Hillebrand, G. Kalosakas, A. Schwellnus, and C. Skokos. Heterogeneity and chaos in the Peyrard-Bishop-Dauxois DNA model. *Physical Review E*, 99(2):1–8, 2019.

H. Hu, A. Strybulevych, J. H. Page, S. E. Skipetrov, and B. A. Van Tiggelen. Localization of ultrasound in a three-dimensional elastic network. *Nature Physics*, 4(12):945–948, 2008.

A. Iomin. Subdiffusion in classical and quantum nonlinear Schrödinger equations with disorder. *Computers and Mathematics with Applications*, pages 1–17, 2017.

K. Ishii. Localization of eigenstates and transport phenomena in the one-dimensional disordered system. *Supplement of the progress of Theoretical Physics*, (53), 1973.

M. V. Ivanchenko, T. V. Laptyeva, and S. Flach. Anderson Localization or Nonlinear Waves : A Matter of Probability. *Physical Review Letters*, 107:240602, 2011.

M. V. Ivanchenko, T. V. Laptyeva, and S. Flach. Quantum chaotic subdiffusion in random potentials. *Physical Review B - Condensed Matter and Materials Physics*, 89(6):4–7, 2014.

F. Jendrzejewski, A. Bernard, K. Müller, P. Cheinet, V. Josse, M. Piraud, L. Pezzé, L. Sanchez-Palencia, A. Aspect, and P. Bouyer. Three-dimensional localization of ultracold atoms in an optical disordered potential. *Nature Physics*, 8(5):398–403, 2012.

M. Johansson. Discrete nonlinear Schrödinger approximation of a mixed Klein-Gordon/Fermi-Pasta-Ulam chain: Modulational instability and a statistical condition for creation of thermodynamic breathers. *Physica D*, 216:62–70, 2006.

M. Johansson and K. Rasmussen. Statistical mechanics of general discrete nonlinear Schrödinger models: Localization transition and its relevance for Klein-Gordon lattices. *Physical Review E*, 70(6):15, 2004.

M. Johansson, G. Kopidakis, and S. Aubry. KAM tori in 1D random discrete nonlinear Schrödinger model? *Epl*, 91(5):1–6, 2010.

S. John. Strong localization of photons in certain disordered dielectric superlattices. *Physical Review Letters*, 58(23):2486–2489, 1987.

S. John, H. Sompolinsky, and M. J. Stephen. Localization in a disordered elastic medium near two dimensions. *Physical Review B*, 27(9):5592–5603, 1983.

K. L. Johnson. *Contact Mechanics*. Cambridge University Press, New York, 1985.

W. Kahan and R.-c. Li. Composition constants for raising the orders of unconventional schemes for ordinary differential equations. *Mathematics of Computation*, 66(219): 1089–1099, 1997.

P. G. Kevrekidis, K. Rasmussen, and A. R. Bishop. The discrete nonlinear Schrödinger equation: A survey of recent results. *International Journal of Modern Physics B*, 15 (21):2833–2900, 2001.

Y. S. Kivshar. Creation of nonlinear localized modes in discrete lattices. *Physical Review E*, 48(5):4132–4135, 1993.

Y. S. Kivshar and G. P. Agrawal. *Optical solitons: From fibers to photonic crystals*. Elsevier Science, 2003.

Y. S. Kivshar and M. Peyrard. Modulational instabilities in discrete lattices. *Physical Review A*, 46(6):3198–3205, 1992.

S. S. Kondov, W. R. McGehee, J. J. Zirbel, and B. DeMarco. Three-dimensional Anderson localization of ultracold matter. *Science*, 334(6052):66–68, 2011.

T. Kontorova and J. Frenkel. On the theory of plastic deformation and twinning. *Zh. Ekap. Teor. Fiz.*, 8:1340–1348, 1938.

G. Kopidakis, S. Komineas, S. Flach, and S. Aubry. Absence of wave packet diffusion in disordered nonlinear systems. *Physical Review Letters*, 100(8):1–4, 2008.

P. Koseleff. Exhaustive search of symplectic integrators using computer algebra. *Integration Algorithms and Classical Mechanics*, 10:103–119, 1996.

P. V. Koseleff. Relations among lie formal series and construction of symplectic integrators. *Lecture Notes in Computer Science*, 673:213–230, 1993.

B. Kramer, A. MacKinnon, H. Search, C. Journals, A. Contact, and M. Iopscience. Localization: theory and experiment. *Rep Prog Phys*, 56(56):1469–1564, 1993.

D. O. Krimer and S. Flach. Statistics of wave interactions in nonlinear disordered systems. *Physical Review E*, 82(4):1–7, 2010.

Y. Lahini, A. Avidan, F. Pozzi, M. Sorel, R. Morandotti, D. N. Christodoulides, and Y. Silberberg. Anderson localization and nonlinearity in one-dimensional disordered photonic lattices. *Physical Review Letters*, 100(1):1–4, 2008.

Y. Lahini, R. Pugatch, F. Pozzi, M. Sorel, R. Morandotti, N. Davidson, and Y. Silberberg. Observation of a localization transition in quasiperiodic photonic lattices. *Physical Review Letters*, 103(1):1–4, 2009.

T. V. Laptyeva, J. D. Bodyfelt, D. O. Krimer, C. Skokos, and S. Flach. The crossover from strong to weak chaos for nonlinear waves in disordered systems. *EPL*, 91(3):1–6, 2010.

T. V. Laptyeva, J. D. Bodyfelt, and S. Flach. Subdiffusion of nonlinear waves in two-dimensional disordered lattices. *EPL*, 98(6), 2012.

T. V. Laptyeva, J. D. Bodyfelt, and S. Flach. Do nonlinear waves in random media follow nonlinear diffusion equations? *Physica D*, 256-257:1–6, 2013.

T. V. Laptyeva, M. V. Ivanchenko, and S. Flach. Nonlinear lattice waves in heterogeneous media. *Journal of Physics A: Mathematical and Theoretical*, 47(49), 2014.

J. Laskar and P. Robutel. High order symplectic integrators for perturbed Hamiltonian systems. *North-Holland Mathematics Studies*, 158(C):263–299, 2001.

B. Li, H. Zhao, and B. Hu. Can disorder induce a finite thermal conductivity in 1D lattices? *Physical Review Letters*, 86(1), 2001.

L. Losonczi. Eigenvalues and eigenvectors of some tridiagonal matrices. 60(251):309–322, 1992.

E. Lucioni, B. Deissler, L. Tanzi, G. Roati, M. Zaccanti, M. Modugno, M. Larcher, F. Dalfovo, M. Inguscio, and G. Modugno. Observation of subdiffusion in a disordered interacting system. *Physical Review Letters*, 106(23):1–4, 2011.

E. Lucioni, L. Tanzi, C. D'Errico, M. Moratti, M. Inguscio, and G. Modugno. Modeling the transport of interacting matter waves in a disordered system by a nonlinear diffusion equation. *Physical Review E*, 87(4):1–6, 2013.

A. M. Lyapunov. The General Problem of the Stability of Motion. *International Journal of Control*, 55(3):531–773, 1992.

M. Manghi and N. Destainville. Physics of base-pairing dynamics in DNA. *Physics Reports*, 631:1–41, 2016.

B. Many Manda, B. Senyange, and C. Skokos. Chaotic wave-packet spreading in two-dimensional disordered nonlinear lattices. *Physical Review E*, 101(3):3–8, 2020.

A. J. Martínez, P. G. Kevrekidis, and M. A. Porter. Superdiffusive transport and energy localization in disordered granular crystals. *Physical Review E*, 93(2):1–21, 2016.

R. I. McLachlan. Composition methods in the presence of small parameters. *BIT Numerical Mathematics*, 35(2):258–268, 1995.

E. Michaely and S. Fishman. Effective noise theory for the nonlinear Schrödinger equation with disorder. *Physical Review E*, 85(4):1–8, 2012.

A. V. Milovanov and A. Iomin. Localization-delocalization transition on a separatrix system of nonlinear Schrödinger equation with disorder. *Epl*, 100(1), 2012.

H. T. Moges, T. Manos, and C. Skokos. On the behavior of the generalized alignment index (Gali) method for regular motion in multidimensional hamiltonian systems. *Nonlinear Phenomena in Complex Systems*, 23(2):153–164, 2020.

M. I. Molina, N. Lazarides, and G. P. Tsironis. Optical surface modes in the presence of nonlinearity and disorder. *Physical Review E*, 85(1):4–7, 2012.

A. Morbidelli. Modern Integrations of Solar System Dynamics. *Annual Review of Earth and Planetary Sciences*, 30(1):89–112, 2002.

O. Morsch and M. Oberthaler. Dynamics of Bose-Einstein condensates in optical lattices. *Reviews of Modern Physics*, 78(1):179–215, 2006.

M. Mulansky and A. Pikovsky. Spreading in disordered lattices with different nonlinearities. *EPL*, 90(1):10015, 2010.

M. Mulansky and A. Pikovsky. Scaling properties of energy spreading in nonlinear Hamiltonian two-dimensional lattices. *Physical Review E*, 86(5):1–7, 2012.

M. Mulansky and A. Pikovsky. Energy spreading in strongly nonlinear disordered lattices. *New Journal of Physics*, 15, 2013.

M. Mulansky, K. Ahnert, A. Pikovsky, and D. L. Shepelyansky. Dynamical thermalization of disordered nonlinear lattices. *Physical Review E*, 80(5):1–5, 2009.

A. Ngapasare, G. Theocharis, O. Richoux, C. Skokos, and V. Achilleos. Chaos and Anderson localization in disordered classical chains: Hertzian versus Fermi-Pasta-Ulam-Tsingou models. *Physical Review E*, 99(3):1–10, 2019.

V. I. Oseledec. A multiplicative ergodic theorem. Lyapunov characteristic numbers for dynamical systems. *Trans. Mosc. Soc*, 19(197), 1968.

A. A. Ovchinnikov, N. S. Erikhman, and K. A. Pronin. *Vibrational-rotational excitations in nonlinear molecular systems*. Springer Science+Business Media, New York, 1 edition, 2001.

S. Paleari and T. Penati. *An extensive resonant normal form for an arbitrary large Klein–Gordon model*, volume 195. 2016.

T. Pertsch, U. Peschel, J. Kobelke, K. Schuster, H. Bartelt, S. Nolte, A. Tünnermann, and F. Lederer. Nonlinearity and disorder in fiber arrays. *Physical Review Letters*, 93 (5):1–4, 2004.

Y. B. Pesin. Characteristic Lyapunov exponents and smooth ergodic theory. *Russian Mathematical Surveys*, 32(4):55–114, 1977.

M. Peyrard. Nonlinear dynamics and statistical physics of DNA. *Nonlinearity*, 17(2), 2004.

A. S. Pikovsky and D. L. Shepelyansky. Destruction of Anderson localization by a weak nonlinearity. *Physical Review Letters*, 100(9):1–4, 2008.

L. Pistone, M. Onorato, and S. Chibbaro. Thermalization in the discrete nonlinear Klein-Gordon chain in the wave-turbulence framework. *EPL*, 121(4), 2018.

L. Prandtl. Ein Gedankenmodell zur kinetischen Theorie der festen Körper. *Z. angew. Math. Mech.*, 8(2):85–106, 1928.

T. Prat, D. Delande, and N. Cherroret. Quantum boomeranglike effect of wave packets in random media. *Physical Review A*, 99(023629):1–5, 2019.

K. Rayanov, G. Radons, and S. Flach. Decohering localized waves. *Physical Review E*, 88(1):1–6, 2013.

G. Roati, C. D'Errico, L. Fallani, M. Fattori, C. Fort, M. Zaccanti, G. Modugno, M. Modugno, and M. Inguscio. Anderson localization of a non-interacting Bose–Einstein condensate. *Nature*, 453(7197):895–898, 2008.

C. D. T. Runge. Über die numerische Auflösung von Differentialgleichungen. *Mathematische Annalen*, 46:167–178, 1895.

R. D. Ruth and C. A. Berkeley. A canonical integration technique. *IEEE Transactions on Nuclear Science*, NS-30(4):2669–2671, 1983.

L. Sanchez-Palencia and M. Lewenstein. Disordered quantum gases under control. *Nature Physics*, 6(2):87–95, 2010.

F. Scheffold, R. Lenke, R. Tweer, and G. Maret. Localization or classical diffusion of light? *Nature*, 398(6724):181, 1999.

T. Schwartz, G. Bartal, S. Fishman, and M. Segev. Transport and Anderson localization in disordered two-dimensional photonic lattices. *Nature*, 446(7131):52–55, 2007.

B. Senyange and C. Skokos. Computational efficiency of symplectic integration schemes: application to multidimensional disordered Klein–Gordon lattices. *European Physical Journal: Special Topics*, 227(5-6):625–643, 2018.

B. Senyange, B. M. Manda, and C. Skokos. Characteristics of chaos evolution in one-dimensional disordered nonlinear lattices. *Physical Review E*, 98(5):1–10, 2018.

B. Senyange, J. J. du Plessis, B. Many Manda, and C. Skokos. Properties of normal modes in a modified disordered Klein–Gordon lattice: From disorder to order. *Nonlinear Phenomena in Complex Systems*, 23(2):165–171, 2020.

L. Sirovich, P. Holmes, D. Barkley, M. Dellnitz, and P. Newton. *Solitons: An introduction*, volume M. 2005.

C. Skokos. The Lyapunov Characteristic Exponents and Their Computation. In *Lect. Notes Phys.*, volume 790, pages 63–135. Springer-Verlag Berlin Heidelberg, 2010.

C. Skokos and S. Flach. Spreading of wave packets in disordered systems with tunable nonlinearity. *Physical Review E*, 82(1):1–9, 2010.

C. Skokos and E. Gerlach. Numerical integration of variational equations. *Physical Review E*, 82(3), 2010.

C. Skokos, D. O. Krimer, S. Komineas, and S. Flach. Delocalization of wave packets in disordered nonlinear chains. *Physical Review E*, 79(5):1–12, 2009.

C. Skokos, I. Gkolias, and S. Flach. Nonequilibrium chaos of disordered nonlinear waves. *Physical Review Letters*, 111(6):1–5, 2013.

C. Skokos, G. A. Gottwald, and J. Laskar, editors. *Chaos Detection and Predictability*, volume 915. Springer-Verlag Berlin Heidelberg, nov 2016.

M. Sofroniou and G. Spaletta. Derivation of symmetric composition constants for symmetric integrators. *Optimization Methods and Software*, 20(4-5):597–613, 2005.

J. B. Sokoloff. Band structure and localization in incommensurate lattice potentials. *Journal of Chemical Information and Modeling*, 53(9):1689–1699, 1981.

M. Störzer, P. Gross, C. M. Aegerter, and G. Maret. Observation of the critical regime near anderson localization of light. *Physical Review Letters*, 96(6):1–4, 2006.

O. Tieleman, C. Skokos, and A. Lazarides. Chaoticity without thermalisation in disordered lattices. *EPL*, 105(2), 2014.

E. Timmermans, P. Tommasini, M. Hussein, and A. Kerman. Feshbach resonances in atomic Bose-Einstein condensates. *Physics Report*, 315(1-4):199–230, 1999.

H. Veksler, Y. Krivolapov, and S. Fishman. Spreading for the generalized nonlinear Schrödinger equation with disorder. *Physical Review E*, 80(3):15–17, 2009.

B. Vermersch and J. C. Garreau. Interacting ultracold bosons in disordered lattices: Sensitivity of the dynamics to the initial state. *Physical Review E*, 85(4):1–9, 2012.

B. Vermersch and J. C. Garreau. Spectral description of the dynamics of ultracold interacting bosons in disordered lattices. *New Journal of Physics*, 15, 2013.

R. L. Weaver. Anderson localization of ultrasound. *Wave Motion*, 12(2):129–142, 1990.

R. Weiner and K. Strehmel. *Linear-implizite Runge-Kutta- Methoden und ihre Anwendung*. Vieweg+Teubner Verlag, Wiesbaden, 1992.

D. S. Wiersma, P. Bartolini, A. Lagendijk, and R. Righini. Localization of light in a disordered medium. *Nature*, 390:671–673, 1997.

J. Wisdom and M. Holman. Symplectic maps for the N-body problem. *Journal of Chemical Information and Modeling*, 53(9):1689–1699, 1991.

H. Wolkowicz and G. P. Styan. Bounds for eigenvalues using traces. *Linear Algebra and Its Applications*, 29:471–506, 1980.

D. Yan, P. G. Kevrekidis, and D. J. Frantzeskakis. Dark solitons in a Gross-Pitaevskii equation with a power-law nonlinearity: Application to ultracold Fermi gases near the Bose-Einstein condensation regime. *Journal of Physics A: Mathematical and Theoretical*, 44(41), 2011.

H. Yoshida. Construction of higher order symplectic integrators. *Physics Letters A*, 150 (5-7):262–268, 1990.

W. C. Yueh. Eigenvalues of several tridiagonal matrices. *Applied Mathematics E - Notes*, 5:66–74, 2005.